

This work was written as part of one of the author's official duties as an Employee of the United States Government and is therefore a work of the United States Government. In accordance with 17 U.S.C. 105, no copyright protection is available for such works under U.S. Law.

Public Domain Mark 1.0











<https://creativecommons.org/publicdomain/mark/1.0/>

Access to this work was provided by the University of Maryland, Baltimore County (UMBC) ScholarWorks@UMBC digital repository on the Maryland Shared Open Access (MD-SOAR) platform.

**Please provide feedback**

Please support the ScholarWorks@UMBC repository by emailing [scholarworks-group@umbc.edu](mailto:scholarworks-group@umbc.edu) and telling us what having access to this work means to you and why it's important to you. Thank you.

# Modeling the High-Energy Ionizing Output from Simple Stellar and X-ray Binary Populations

KRISTEN GAROFALI <sup>1</sup>, ANTARA R. BASU-ZYCH <sup>1,2,3</sup>, BENJAMIN D. JOHNSON,<sup>4</sup> PANAYIOTIS TZANAVARIS,<sup>2,3,5</sup>  
ANNE JASKOT <sup>6</sup>, CHRIS RICHARDSON <sup>7</sup>, BRET D. LEHMER <sup>8</sup>, MIHOKO YUKITA <sup>9</sup>, EDMUND HODGES-KLUCK <sup>1</sup>,  
ANN HORNSCHEMEIER <sup>1</sup>, ANDREW PTAK <sup>1</sup> AND NEVEN VULIC <sup>10</sup>

<sup>1</sup>NASA Goddard Space Flight Center, Code 662, Greenbelt, MD 20771, USA

<sup>2</sup>Center for Space Science and Technology, University of Maryland, Baltimore County, Baltimore, MD 21250, USA

<sup>3</sup>Center for Research and Exploration in Space Science and Technology, NASA Goddard Space Flight Center, Greenbelt, MD 20771, USA

<sup>4</sup>Center for Astrophysics | Harvard & Smithsonian, 60 Garden Street, Cambridge, MA 02138, USA

<sup>5</sup>American Physical Society, Hauppauge, New York, NY 11788, USA

<sup>6</sup>Department of Astronomy, Williams College, Williamstown, MA 01267, USA

<sup>7</sup>Elon University, Elon, NC 27278, USA

<sup>8</sup>Department of Physics, University of Arkansas, Fayetteville, AR 72701, USA

<sup>9</sup>William H. Miller III Department of Physics and Astronomy, Johns Hopkins University, Baltimore, MD 21218, USA

<sup>10</sup>Eureka Scientific, Inc., Oakland, CA 94602-3017, USA

## ABSTRACT

We present a methodology for modeling the joint ionizing impact due to a “simple X-ray population” (SXP) and its corresponding simple stellar population (SSP), where “simple” refers to a single age and metallicity population. We construct composite spectral energy distributions (SEDs) including contributions from ultra-luminous X-ray sources (ULXs) and stars, with physically meaningful and consistent consideration of the relative contributions of each component as a function of instantaneous burst age and stellar metallicity. These composite SEDs are used as input for photoionization modeling with CLOUDY, from which we produce a grid for the time- and metallicity-dependent nebular emission from these composite populations. We make the results from the photoionization simulations publicly available. We find that the addition of the SXP prolongs the high-energy ionizing output from the population, and correspondingly increases the intensity of nebular lines such as He II  $\lambda 1640, 4686$ , [Ne V]  $\lambda 3426, 14.3\mu\text{m}$ , and [O IV]  $25.9\mu\text{m}$  by factors of at least two relative to models without an SXP spectral component. This effect is most pronounced for instantaneous bursts of star formation on timescales  $> 10$  Myr and at low metallicities ( $\sim 0.1 Z_{\odot}$ ), due to the imposed time- and metallicity-dependent behavior of the SXP relative to the SSP. We propose nebular emission line diagnostics accessible with *JWST* suitable for inferring the presence of a composite SXP + SSP, and discuss how the ionization signatures compare to models for sources such as intermediate mass black holes.

## 1. INTRODUCTION

Over the past decade, spectroscopic observations of high redshift ( $z > 6$ ) galaxies and their nearby analogs have revealed the presence of strong high-ionization nebular emission lines (e.g., He II, [Ar IV], [Ne V]) and lines with high equivalent widths, indicating the presence of relatively hard ionizing spectra, recent ( $\lesssim 30$  Myr) star formation, and relatively low metallicities ( $\sim 0.1 Z_{\odot}$ ) (e.g., Jaskot & Oey 2013; Stark 2016; Berg et al. 2018, 2019; Senchyna et al. 2017, 2019; Olivier et al.

2022). Attempts to model the observed nebular features of such “extreme emission line galaxies” (EELGs) have revealed that the spectral energy distributions (SEDs) from young, low-metallicity stellar populations have difficulty reproducing the observed strengths of a number of high-ionization emission line species, a problem that has been referred to as the “high-energy ionizing photon production problem” (Berg et al. 2021).

Addressing this problem is key to understanding how the heating and reionization of the Universe proceeds at  $z > 6$ , a regime now becoming more accessible spectroscopically thanks to *JWST*. In the coming decade, second generation interferometers such as the Hydrogen Epoch of Reionization Array (HERA) will probe even

earlier cosmic epochs ( $6 < z < 50$ ) through the cosmic 21-cm signal. This high-redshift 21-cm signal is sensitive to the UV to soft X-ray ( $< 2$  keV) radiation field produced by the first galaxies’ dominant ionizing populations. Initial results from HERA already suggest that the emergent 0.5–2.0 keV X-ray luminosity per galaxy star formation rate ( $L_X$  (0.5–2 keV)/SFR) from galaxies at  $z > 6$  is at least an order of magnitude higher than measured for local galaxies (HERA Collaboration et al. 2023). These results point to increased production efficiency of photons with energies  $\gtrsim 500$  eV from galaxies at high redshift, possibly due to increased formation efficiency of accreting compact objects at the lower metallicities and/or younger stellar populations ages characteristic of early galaxies (e.g., Fragos et al. 2013a). Developing a comprehensive accounting of the major sources of high-energy ionizing photons in EELGs, both near and far, therefore requires a framework for modeling how *additional* ionizing sources—such as fast shocks, superbubbles, and X-ray binaries (XRBs)—evolve as a function of redshift-dependent properties such as metallicity and stellar population age (e.g., Allen et al. 2008; Oskinova & Schaerer 2022; Simmonds et al. 2021).

One potential alternative source of high-energy ionizing photons is radiative shocks, which may be produced as a consequence of massive star evolution through winds and supernovae explosions (e.g., Izotov et al. 2012, 2021). For fast shocks, there are publicly available grids of emission line ratios for a range of shock properties (Allen et al. 2008). Based on such models, shocks appear capable of sufficient high-energy ionizing photon production to reproduce select observed nebular line intensities for some shock velocities (e.g., Thuan & Izotov 2005); however, it is not yet clear whether fast shocks are capable of simultaneously reproducing suites of high-ionization nebular lines (i.e., from UV to optical), particularly if there is a metallicity-dependence to the observed line ratios (e.g., Senchyna et al. 2017).

Numerous works have also investigated the need for changes to prescriptions used in *stellar* spectral population synthesis and photoionization modeling, such as changes to assumed abundance patterns (e.g., Berg et al. 2021), the initial mass function (IMF) and associated products of binary evolution (e.g., Götzberg et al. 2019; Senchyna et al. 2021), and/or assumptions about stellar rotation and line-driven winds for massive stars at very low metallicities (e.g., Telford et al. 2021). There are publicly available and well-vetted libraries for stellar atmosphere models and isochrones that allow for testing how these different prescriptions affect the ionizing output from stellar populations (see e.g., Conroy 2013, for a review of models). With stellar spectral popu-

lation synthesis, these ingredients can be flexibly combined for a given IMF to produce the SEDs for simple stellar populations (SSPs)—populations at a single burst age and metallicity—for use in photoionization modeling and spectrophotometric fitting (e.g., Conroy et al. 2009; Conroy & Gunn 2010; Byler et al. 2017; Johnson et al. 2021). These tools enable investigation of how tweaks to stellar population models can address the high-energy ionizing photon production problem (e.g., Berg et al. 2019; Senchyna et al. 2021). However, presently available stellar population models, including those that model some of the products of binary evolution, still have difficulty reproducing the observed intensities of select high-ionization nebular emission lines (e.g., He II; Stanway & Eldridge 2019). This highlights the need for more comprehensive accounting of the products of binary evolution that may contribute to the ionizing photon budget.

Accreting stellar mass compact objects (i.e., XRBs) are one such product of binary evolution, and have long been considered as a potential source of high-energy ionizing photons (e.g., Garnett et al. 1991; Schaerer et al. 2019; Kovelakas et al. 2022). Recent photoionization modeling that combines XRBs with stellar populations hints that XRBs may be sufficient to reproduce observed high-ionization emission line strengths *in some cases* (e.g., Senchyna et al. 2020; Simmonds et al. 2021). However, drawing a cohesive picture of the efficacy of XRBs to addressing the high-energy ionizing photon production problem remains challenging due to the following issues: (1) differing prescriptions for intrinsic XRB SEDs and; (2) minimal consideration towards how to scale XRB power output relative to the stellar population as a function of star formation history (SFH) and metallicity. Critically, for XRBs we currently lack many of the ingredients necessary for truly flexible spectral population synthesis, and therefore a means to understand the XRB contribution to high-energy ionizing photon production. In this work, we take steps to address this via the development of a flexible framework for including XRBs alongside SSPs for use in photoionization modeling.

XRBs, and specifically those sources at the extreme bright-end of the luminosity function known as ultra-luminous X-ray sources (ULXs), are a compelling option for producing high-energy ionizing photons in high redshift galaxies and their local analogs for a few key reasons. Specifically, such sources (1) form swiftly ( $\gtrsim 3$  Myr) in multiple generations following a burst of star formation, and are therefore capable of producing ionizing photons on longer timescales than single massive stars (e.g., Linden et al. 2010); (2) dominate the X-ray power output from normal star-forming galaxies (i.e.,

those without an actively accreting supermassive black hole) at high specific SFRs (e.g., [Lehmer et al. 2016](#)); and (3) have integrated luminosities directly proportional to SFR that increase with decreasing gas-phase metallicity, resulting in increased contribution to the photon budget in low-metallicity, highly star-forming galaxies (e.g., [Basu-Zych et al. 2013, 2016](#); [Brorby & Kaaret 2017](#)). For ULXs specifically, there is also increasing evidence for the presence of powerful outflows (e.g., [Pinto et al. 2016](#)), which may additionally produce shocks ([López et al. 2019](#); [Gúrpide et al. 2022](#)). ULXs may therefore be important sources of both radiative and mechanical feedback at the low metallicities and high specific SFRs characteristic of high redshift galaxies and their local analogs.

A key consideration for modeling the ionizing contribution from accreting stellar mass compact objects such as ULXs is that they should form as a consequence of the evolution of the stellar population. To address this, we present a methodology for constructing a simple X-ray population (SXP), analogous to an SSP (i.e., single age and metallicity), and an approach to a physically consistent coupling of the SXP to the corresponding SSP for use in photoionization modeling. This approach is aimed at providing a more comprehensive framework for investigating the XRB contribution to the high-energy ionizing photon production problem.

This paper is organized as follows: in Section 2 we present the main elements used in constructing the SXP and in Section 3 we outline how the SXP is scaled and added to the corresponding SSP to create the SED for a composite population. In Section 4 we describe our grid-based photoionization modeling set-up using the composite SXP + SSP SEDs. In Section 5 we present key results from the photoionization modeling for the nebular emission from the composite populations, and describe how to access our simulation results. In Section 6 we discuss the SXP model and photoionization simulation results in the context of X-ray detectability, recent literature results for the contribution of X-ray sources to the production of high-ionization emission lines, and alternative ionizing sources. Finally, in Section 7, we summarize our key findings.

## 2. CONSTRUCTING A SIMPLE X-RAY POPULATION

To construct the inputs for the photoionization modeling that follows, we apply the formalism of SSPs to accreting stellar mass compact objects. In what follows, we refer to models for single age and metallicity accreting compact object “populations” as “SXPs.” In constructing these SXPs we consider selection of the fol-

lowing three key ingredients: (1) power output for the population as a function of stellar population age and metallicity; (2) the dominant source type in the population; and (3) physically motivated *intrinsic* source spectra. In this section, we describe the SXP used in this work based on selections for these three ingredients.

### 2.1. Normalization as a Function of Metallicity and Instantaneous Burst Age

Constructing a true SXP requires a prescription for the normalization of X-ray emitting population as a function of burst age and metallicity. To describe this behavior, we use the theoretical predictions for the X-ray power output per stellar mass from XRBs as a function of age and stellar metallicity from the binary population synthesis models presented in [Fragos et al. \(2013b\)](#). We opt to use these theoretical predictions, as opposed to empirical measurements, for two key reasons. First, the evolution of XRB power output—particularly on finely resolved timescales  $\lesssim 100$  Myr that are important for luminous XRB formation—is not yet well-constrained observationally (e.g., [Lehmer et al. 2017](#)). In addition, empirical constraints on XRB radiative power as a function of time or metallicity are typically reported in terms of  $L_X/\text{SFR}$ , where the SFR is a quantity averaged over some extended timescale (i.e., 10 or 100 Myr). In this way, available empirical measurements are a time-averaged  $L_X$  for the *observed* XRB population. Such measurements are therefore not well-suited to simulating the ionizing output from the *intrinsic* XRB population formed from an instantaneous burst of star formation, as we aim to do here.

A critical component of the selected theoretical population synthesis models from [Fragos et al. \(2013b\)](#) is therefore that the predictions are provided in terms of radiative power ( $L_X$ ) from the intrinsic XRB population per stellar mass formed in a burst of star formation ( $M_0$ ). Nearly all other theoretical binary population synthesis models currently in the literature that focus on XRBs provide predictions in terms of *number counts* of sources per stellar mass as function of time and metallicity (e.g., [Linden et al. 2010](#); [Wiktorowicz et al. 2019](#)). For the purposes of the photoionization modeling that follows,  $L_X/M_0$  is the preferred quantity since transforming number counts to total radiative power is non-trivial, and requires additional assumptions about how the luminosities of different sources should be calculated from theoretical mass supply rates. The models from [Fragos et al. \(2013b\)](#) track the mass supply rate to the compact object population—both black holes (BHs) and neutron stars (NS)—as a function of time. Following prescriptions in [Fragos et al. \(2008, 2009\)](#), the bolomet-

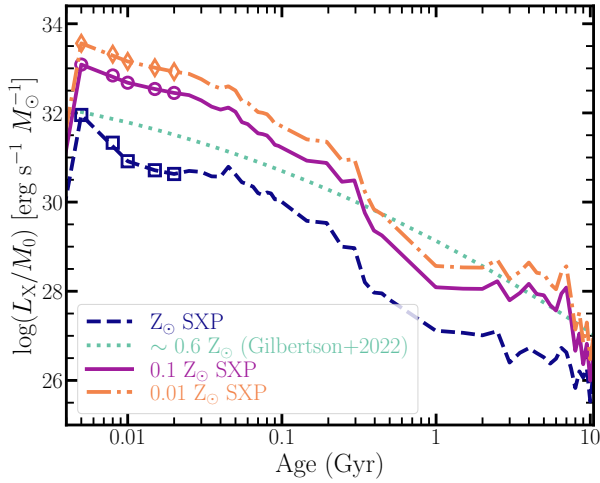


**Figure 1.** The adopted scaling of  $L_X/M_0$  for the SXP as a function of instantaneous burst age and metallicity ( $Z_\odot$ : dark blue dashed line,  $0.1 Z_\odot$ : purple solid line, and  $0.01 Z_\odot$ : orange dash-dot line) from theoretical binary population synthesis models (Fragos et al. 2013b). The instantaneous burst ages at which we model the SXP contribution in the photoionization simulations are marked with dark blue squares, purple circles, and orange diamonds for the  $Z_\odot$ ,  $0.1 Z_\odot$ , and  $0.01 Z_\odot$  cases, respectively. The SXP component in our models turns on for instantaneous bursts  $> 3$  Myr. Empirical results for  $L_X/M_0$  from star-forming galaxy stacks in the *Chandra* Deep Fields, for which the median metallicity ( $\sim 0.6 Z_\odot$ ) is intermediate to the theoretical scalings adopted here, are shown as a green dotted line for reference.

ric  $L_X$  is calculated directly for persistent XRBs from the mass supply rate along with the mass and radius of the accretor, assuming different conversion efficiencies for BHs and NS. For transient XRBs, a modified version of this formalism is applied, considering typical duty cycles and outburst luminosities.

The Fragos et al. (2013b) binary population synthesis models used here provide published values of  $L_X/M_0$  for XRBs at three different stellar metallicities<sup>1</sup>:  $Z = 0.002$  ( $0.1 Z_\odot$ ),  $Z = 0.02$  ( $Z_\odot$ ), and  $Z = 0.03$  ( $1.5 Z_\odot$ ), and burst ages from 0–10 Gyr. To calculate the normalization of the SXP as a function of age and metallicity, we select a set of seven discrete burst ages and three metallicities from the reference model in Fragos et al. 2013b (i.e., their Figure 2, data provided via private communication).

<sup>1</sup> Throughout, we assume  $Z = 0.02$  corresponds to  $Z_\odot$  for stellar metallicities. For abundances from Anders & Grevesse (1989), this corresponds to a gas-phase metallicity  $12 + \log(\text{O}/\text{H}) = 8.93$ .

The seven discrete time steps ( $t_{\text{burst}} \sim \{1, 3, 5, 8, 10, 15, 20\}$  Myr) are selected to maximize  $L_X/M_0$  (i.e., capture the bounding case for XRB ionization), and to cover relevant timescales for important stages of massive star evolution. On these short burst timescales, the XRB population power output is dominated by sources descended from the most massive stars, and such sources are therefore considered high-mass XRBs (HMXBs). As such, we calculate the normalization of the SXP to reproduce the theoretical  $L_X$  (0.5–8 keV)/ $M_0$  from the HMXB component of the reference model in Fragos et al. (2013b). We additionally elect to turn on the SXP with a delay time that accounts for the minimum time for the first BHs to form and begin accreting (e.g., Belczynski & Taam 2008; Linden et al. 2010). The first time step in the simulations with SXP contribution is 4 Myr.

Two of the three metallicities selected for our models include those available from the published theoretical population synthesis results, namely  $Z = 0.002$  ( $0.1 Z_\odot$ ) and  $Z = 0.02$  ( $Z_\odot$ ), where the  $0.1 Z_\odot$  scaling for  $L_X/M_0$  is relevant for nearby EELGs and sources at  $z \gtrsim 3$  (e.g., Shirazi & Brinchmann 2012; Madau & Dickinson 2014). We additionally add a third metallicity set at  $\sim 0.01 Z_\odot$ , though this metallicity is not originally included in the theoretical population synthesis models. To create normalizations for the SXP for this extremely metal-poor case, we assume the same dependence of  $L_X/M_0$  on post-starburst timescale as the  $0.1 Z_\odot$  model, but allow the absolute normalization of  $L_X/M_0$  to be a factor of  $3\times$  higher than for the  $0.1 Z_\odot$  at each time step. This scaling corresponds roughly to the observed  $\langle L_X/\text{SFR} \rangle$  from galaxies with  $12 + \log(\text{O}/\text{H}) \sim 7.0$ , the lowest metallicity for which the observed  $L_X$ –SFR– $Z$  scaling relation has been calibrated (Lehmer et al. 2021). Though speculative, we include this case for reference, noting that it will likely need to be revised either theoretically or observationally going forward.

In Figure 1, we show the adopted theoretical  $L_X/M_0$  as a function of instantaneous burst age for the three metallicities employed in the photoionization simulations that follow, with the burst ages for which the SXP contribution is modeled denoted with symbols. For reference, we also plot in this figure empirical results from Gilbertson et al. (2022) for  $L_X/M_0$  for a sample of star-forming galaxy stacks from *Chandra* Deep Fields. The galaxy stacks from the *Chandra* Deep Fields have median metallicity  $\sim 0.6 Z_\odot$ , intermediate to our selected metallicity range, illustrating that the empirical results are in qualitative agreement with the behavior of the adopted theoretical relations on the timescales of interest for these simulations.



The adopted theoretical values for  $L_X/M_0$  from Figure 1 can be considered as good approximations for the *average* radiative output from a population. For the purposes of our simulations, this is appropriate as we seek to simulate a well-sampled population; however, for observed samples the X-ray luminosity function (XLF) may not be as well-populated. Stochastic sampling of the XLF is particularly important to consider at very low SFRs ( $\lesssim 0.1 M_\odot \text{ yr}^{-1}$ ), where observed values for  $L_X/M_\star$  or  $L_X/\text{SFR}$  can be subject to scatter of order  $\sim 1$  dex, especially for sources at the bright end of the XLF (Lehmer et al. 2021). We return to this point in Section 6.1 in discussing how results from these simulations should be compared against observations.

## 2.2. Source Type: Ultra-luminous X-ray Sources

With the adopted scaling for  $L_X/M_0$ , we next consider the source type that dominates the power output from the population. In star-forming galaxies without a central accreting supermassive black hole, XRBs dominate the galaxy-integrated X-ray point source emission. For predominantly young stellar populations ( $\lesssim 100$  Myr) HMXBs are the dominant accretor population, while in galaxies with older stellar populations low-mass XRBs (i.e., sources with low-mass donor stars) dominate the radiative output (e.g., Garofali et al. 2018; Lehmer et al. 2019, 2021).

Regardless of stellar population age, the total radiative power output from a population will be dominated by the sources that populate the bright end of the XLF. Such sources are ULXs, off-nuclear point sources with  $L_X > 10^{39} \text{ erg s}^{-1}$ . These luminosities, under the assumption of isotropic emission, exceed the Eddington limit for a  $10 M_\odot$  BH or  $1.4 M_\odot$  NS:

$$L_{\text{Edd}} = \frac{4\pi G M c}{\kappa_T} = 1.5 \times 10^{38} m \frac{1.7}{1+X} \text{ ergs}^{-1} \quad (1)$$

where  $M$  is the mass of the compact object (such that  $m \equiv M/M_\odot$ ),  $X$  is the hydrogen mass fraction (assumed to be  $X = 0.73$ , corresponding to solar composition),  $G$  is the gravitational constant,  $c$  is the speed of light, and  $\kappa_T = 0.2(1+X)$  is the Thomson scattering opacity.

Models to explain the extreme apparent luminosities from ULXs fall broadly into two categories: (1) isotropic emission from sub-Eddington accretion onto intermediate mass black holes (IMBHs; e.g., Colbert & Mushotzky 1999) or (2) super-Eddington mass transfer via modified accretion disks onto either stellar mass BHs or strongly magnetized NS (e.g., King et al. 2001; Begelman et al. 2006; Poutanen et al. 2007; King 2009). Recent results from X-ray timing studies favor the second scenario, as the detection of pulsations in an increasing number of

ULXs indicates the presence of a NS for at least some fraction of the ULX population (e.g., Bachetti et al. 2014; Israel et al. 2017; Brightman et al. 2018). Broadband and high-resolution X-ray spectroscopy of ULXs also support the picture of stellar mass accretors with high mass transfer rates. In particular, the observed spectral turnover for ULXs at energies  $\gtrsim 3\text{--}8$  keV is incompatible with models for intermediate mass or supermassive BHs accreting at sub-Eddington rates (Gladstone et al. 2009a), and the detection of absorption lines for some ULXs provide evidence for the presence of fast outflows (Section 2.3.2; Pinto et al. 2016; Kosec et al. 2018a,b, 2021), and potentially strongly magnetized NS accretors (Walton et al. 2018; Brightman et al. 2022).

These findings suggest ULXs ( $L_X \sim 10^{39} - 10^{42} \text{ erg s}^{-1}$ , i.e., below the hyper-luminous regime) are a distinct class of stellar mass accretors with super-Eddington mass supply rates<sup>2</sup>. This in turn implies that ULXs are indeed the high luminosity extension of the XRB luminosity function. In this work, we treat ULXs as the bright extension of the HMXB luminosity function specifically, as we consider timescales relevant to formation and evolution of the most massive stars ( $\leq 20$  Myr, Section 2.1).

Given that they occupy the bright end of the XLF, ULXs in star-forming galaxies can surpass by at least an order of magnitude the combined output of various HMXB sub-populations filling out the lower luminosity—and more highly populated—portion of the luminosity function (e.g., Lehmer et al. 2021). *In this work, we therefore choose to model the SXP as a population of ULXs.* Assuming a well-sampled XLF (i.e., high SFR) as we model here, a ULX-based SXP is a reasonable approximation for the total XRB population. Indeed, many highly star-forming galaxies (SFRs  $\geq 3 M_\odot \text{ yr}^{-1}$ ) show ULX-like spectra globally (Garofali et al. 2020). Because various HMXB sub-populations likely have different accretion state distributions and scaling relations with metallicity and stellar population age, approximating the SXP using ULXs considerably simplifies the modeling that follows. Hereafter, we refer to the SXP as “SXP<sub>ULX</sub>”, to indicate the source type modeled.

<sup>2</sup> As discussed in King et al. (2023), the phrase “super-Eddington accretion” can lead to ambiguity, as stellar mass BHs and NS in ULXs do not actually accrete matter at highly super-Eddington rates; instead, these authors suggest that for ULXs it would be more appropriate to refer to the mass supply or transfer rate as the super-Eddington quantity in question. We adhere to this convention throughout.

This selection captures a bounding case for HMXB<sup>3</sup> contribution to production of high-energy ionizing photons in terms absolute normalization as emphasized above, as well as hardness of spectral shape (Section 2.3).

### 2.3. Model for Ultra-luminous X-ray Source SED

The efficacy of the SXP<sub>ULX</sub> in the production of high-energy ionizing photons is highly dependent on the shape of the *intrinsic* SED and normalization relative to the corresponding SSP (e.g., [Simmonds et al. 2021](#)). Unfortunately, this intrinsic shape for ULXs is difficult to measure observationally and therefore remains highly uncertain. At the typical extragalactic distances ( $\gtrsim 3$  Mpc) to ULXs, fluxes are  $< 10^{-12}$  erg s<sup>-1</sup> cm<sup>-2</sup>, such that high-resolution X-ray spectroscopy is currently feasible for a limited number ( $\sim 10$ ) of the brightest sources ([Kosec et al. 2018a](#)). At CCD-resolution, many more sources are available for spectral fitting, but these fits are often performed using phenomenological models with no obvious physical basis, which cannot be reliably extrapolated into wavelength regimes outside the observed bandpass. The lack of comprehensive multiwavelength catalogs for ULXs (from IR-to-X-ray) is a further limitation to measuring their intrinsic SEDs, resulting in large uncertainties especially in the extreme ultraviolet (EUV) to very soft X-ray regime ( $\sim 54$ –200 eV). Critically, this is the wavelength regime responsible for setting the intensity of high-ionization nebular emission lines.

We therefore opt to model our SED (hereafter SED<sub>ULX</sub>) using analytic prescriptions from theoretical models for stellar mass compact objects with super-Eddington mass supply rates. In the sections that follow, we outline the key components of the SED<sub>ULX</sub>, and motivate our selections. The SED<sub>ULX</sub> employed throughout this work is qualitatively similar to empirical models derived from analyses of ULXs detected within their own optical nebulae, where high-ionization emission lines are also detected ([Berghea et al. 2010](#); [Berghea & Dudik 2012](#); [Kaaret & Corbel 2009](#); [Lebouteiller et al. 2017](#); [Simmonds et al. 2021](#)). In such analyses, both the broad-band X-ray data and the observed emission line strengths provide constraints on the form of the ULX

SED, where the line emission is particularly useful for constraining the shape of the unseen EUV portion. We note that such a multi-wavelength approach has promise for constraining the shape of the intrinsic SED; however, as pointed out in [Simmonds et al. \(2021\)](#), there is as yet no comprehensive approach in this respect for ULXs given the lack of collated multiwavelength data sets.

#### 2.3.1. Accretor Type

As a starting point to constructing the SED<sub>ULX</sub>, we must select the mass of the accretor as well as the type (BH or NS), as the SED shape will depend not only on accretor mass and mass supply rate, but also on whether the accretion flow encounters a hard surface and/or a strong magnetic field (see Section 6.3.1). Because the selected  $L_X/M_0$  normalizations from Section 2.1 span burst ages  $\leq 20$  Myr, we choose a stellar mass BH ( $< 100 M_\odot$ ) as the accretor for the SED<sub>ULX</sub>. Theoretical binary population synthesis models show that the fraction of NS accretors contributing to the observed ULX population is still low on timescales  $< 20$  Myr post-starburst, and that accreting BHs may have ages  $\sim 4$ –40 Myr during their ULX phase ([Middleton & King 2017](#); [Wiktorowicz et al. 2017, 2019](#)).

Given that we likewise elect to model the population at three discrete stellar metallicities ( $Z_\odot$ ,  $0.1Z_\odot$ , and  $\sim 0.01Z_\odot$ ), we construct the SED<sub>ULX</sub> model as a function of approximate BH masses at each of these metallicities:  $10 M_\odot$ ,  $20 M_\odot$ , and  $40 M_\odot$  from solar to sub-solar metallicities, respectively (e.g., [Belczynski et al. 2010](#); [Fryer et al. 2012](#); [Eldridge & Stanway 2016](#)). The selected masses are likely on the high-end of the mass function for BHs in ULXs, again in order to capture the bounding case for SXP<sub>ULX</sub> ionization. At present it is not clear theoretically or observationally what the typical BH mass is in a ULX, particularly as a function of burst age and metallicity. Thus, we consider using approximate BH masses as a function of metallicity only to be a reasonable simplifying choice given presently available results from binary population synthesis models for ULXs. It is important to note that while these selected BH masses factor into the parametrization of the SED<sub>ULX</sub> shape (Section 2.3.3), they do not strongly affect the *normalization* of the SED<sub>ULX</sub>, which is key to setting the simulated nebular line intensities. Instead, the primary factor affecting SED<sub>ULX</sub> normalization, and therefore nebular line intensities, is the adopted scaling relation for  $L_X/M_0$  as a function of age and metallicity, as presented in Section 2.1.

<sup>3</sup> There is no explicit ULX population included in the theoretical models from [Fragos et al. \(2013b\)](#), and we therefore use the HMXB component, corresponding to the bright end of the XLF, for normalizing the SXP; however, the theoretical models do allow for XRBs undergoing outbursts to exceed Eddington. We also note that empirical values for  $L_X/M_0$  from galaxy-integrated studies, where the populations can be assumed to be dominated by sources at the brightest end of the XLF, i.e., ULXs, appear relatively consistent with the theoretical scaling relations ostensibly for HMXBs employed here, as shown in Figure 1.

### 2.3.2. Accretion Flow Geometry & Components

Under the selection of a stellar mass accretor with super-Eddington mass supply rate for the SED<sub>ULX</sub>, theory and observation alike suggest the presence of a strong outflow, which is a key component in defining the SED shape. In the supercritical regime the accretion flow consists of distinct zones delineated by the wind/outflow component (e.g., Shakura & Sunyaev 1973; Lipunova 1999; Poutanen et al. 2007; Abolmasov et al. 2009). We illustrate these zones in Figure 2, as follows:

- The hot inner region of the accretion flow before the wind launching zone ( $R < R_{\text{ph, in}}$ ).
- The region between the wind launching zone and so-called the spherization radius ( $R_{\text{ph, in}} < R < R_{\text{sph}}$ ), where the wind is optically thick. The spherization radius ( $R_{\text{sph}}$ ) can be thought of as the region where the disk is unstable and super-Eddington (i.e., the actual accretion rate is Eddington within this radius, and limited through the expulsion of matter from the disk as a wind).
- The region beyond the spherization radius where the wind becomes optically thin ( $R > R_{\text{sph}}$ ). The outer extent of the wind is given by the effective photospheric radius of the outflow,  $R_{\text{ph, out}}$ .

Under such a model, the launching of the disk wind leads to an evacuated “wind funnel,” wherein the hard inner disk emission is geometrically collimated and scattered by the wind. At much larger disk radii ( $R > R_{\text{sph}}$ ), the wind becomes optically thin and can be approximated as a pseudo-photosphere (i.e., a quasi-spherical component with a blackbody spectrum). This picture of the accretion flow is broadly consistent with CCD-resolution spectra of ULXs, which typically require multi-component models to fit their observed spectra (e.g., Gladstone et al. 2009b; Sutton et al. 2013; Middleton et al. 2015).

In defining our SED<sub>ULX</sub> model, we therefore include a component representing the hot inner disk and wind funnel, as well as a component for the outflow. In addition, we consider the effects of Compton scattering and irradiation on the resultant SED shape. Irradiation—where one component of the accretion flow absorbs and re-emits radiation from another component—may be critically important in the context of SXP<sub>ULX</sub> contribution to high-energy ionizing photon production. This is because reprocessed emission due to irradiation can produce a spectrum with a more substantial EUV component, where photon energies exceed ionization potentials for lines such as He II  $\lambda 4686$  and [Ne V]  $\lambda 3426$ .

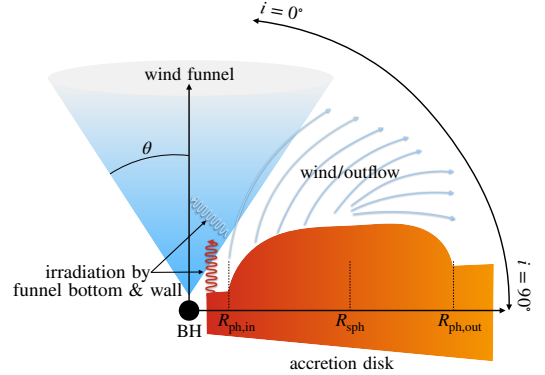


**Figure 2.** Cartoon depiction of the accretion flow geometry for the SED<sub>ULX</sub> model. Key components and parameters are labeled, including the accretor (BH) and accretion disk, evacuated wind funnel and associated funnel opening angle ( $\theta$ ), the inner and outer photospheric radii ( $R_{\text{ph, in}}$ ,  $R_{\text{ph, out}}$ , respectively), the spherization radius ( $R_{\text{sph}}$ ), and the inclination angle ( $i$ ) with respect to an observer. The wind or outflow, which is launched from the accretion disk and assumed to be a quasi-spherical component, is shown by the blue arrows. Irradiating photons emanate from the hot inner accretion flow and funnel walls, as labeled.

Given the geometry of the supercritical accretion flow described above, it is unlikely that there is direct irradiation of the outer regions of the accretion disk by hot inner disk photons (e.g., Gierliński et al. 2009). In the case of a ULX with an outflow, the wind likely blocks and reprocesses the hot inner disk emission. Irradiation may therefore occur via the wind irradiating the outer disk (Vinokurov et al. 2013; Yao & Feng 2019), or via “self-irradiation” of inner disk and funnel wall emission within the wind funnel itself (Abolmasov et al. 2009).

For the SED<sub>ULX</sub> in this work, we choose to model the irradiated component as being due to self-irradiation within the wind funnel. This is because there are uncertainties in how effectively soft photons from the wind thermalize in the outer disk (Kaaret & Corbel 2009; Grisé et al. 2012a), and additional complexities in handling the geometry and radiative transfer for wind irradiation. To represent the supercritical accretion flow with self-irradiation, we opt to use the `sirf`, or “self-irradiated funnel”, template as implemented in XSPEC (Abolmasov et al. 2009). This particular template provides a physical model coupling all components of the supercritical accretion flow, including the hot inner disk, outflow, and the effects of irradiation consistent with the previously described flow geometry. To additionally account for the effects of Compton scattering, we include the `simpl`(SIMple Power Law) convolution component, which Comptonizes flux output from the `sirf` model. Thus, our SED<sub>ULX</sub> is implemented as `simpl(sirf)` in



**Table 1.** Summary of calculated and selected parameters for the SED<sub>ULX</sub> model, as implemented via the `simpl(sirf)` templates in XSPEC. Parameter names follow nomenclature used in XSPEC, as described in the text.

Component	Name	Value	Units
(1)	(2)	(3)	(4)
<b>sirf</b>	$T_{\text{funnel, in}}$	Eq. 8	keV
	$r_{\text{ph, in}}$	Eq. 7	$R_{\text{sph}}$
	$r_{\text{ph, out}}$	Eq. 9	$R_{\text{sph}}$
	$\theta$	45	deg
	$i$	0	deg
	$\alpha$	0	...
	$\gamma$	4/3	...
	$\dot{m}$	Eq 5–6	...
	irrad.	4	...
	norm.	Fragos et al. (2013b)	...
<b>simpl</b>	$\Gamma$	2.5	...
	Frac. Sctr	0.1	...
	Up Sctr. Only	0	...

XSPEC, with relevant parameters listed in Table 1. Under this accretion flow model, the mass supply rate relative to Eddington sets the physical parameters (i.e., characteristic radii and temperatures) that define the shape of the *intrinsic* spectrum, while the viewing angle ( $i$  in Figure 2) determines the shape of the *observed* spectrum. In this respect, the `sirf` template is ideal, as it allows for changing the inclination angle to simulate changes to the apparent emergent spectrum for an observer, a point we return to in more detail in Section 6.1.

### 2.3.3. Parametrization of SED Shape

We aim to construct the SED<sub>ULX</sub> model with as few *selected* parameter values as possible. Therefore, to the extent possible, we calculate parameter values for the `sirf` template analytically from a few key selected physical properties (see Shakura & Sunyaev 1973; Poutanen et al. 2007; Abolmasov et al. 2009, for prescriptions). The primary physical properties for which values are selected are the funnel opening angle ( $\theta$ ) and compact object mass ( $m$ ). For the SED<sub>ULX</sub> used in this work, we select  $\theta = 45^\circ$  and  $m = 10, 20$ , or  $40 M_\odot$  for  $Z_\odot$ ,  $0.1 Z_\odot$ , and  $\sim 0.01 Z_\odot$ , respectively. As shown by the black solid line in Figure 3, the choice of  $\theta = 45^\circ$  results in a relatively flat SED in the EUV regime even without invoking high mass supply rates (i.e., this selection assumes the SXP<sub>ULX</sub> is not universally strongly

beamed; Equations 5–6). This choice for  $\theta$  is therefore important for capturing a bounding case for production of high-energy ionizing photons by the SXP<sub>ULX</sub>, while still producing good qualitative agreement with other ULX SED models across the electromagnetic spectrum, as discussed in Section 6.2. Below we outline how the remaining parameters defining the shape of the SED<sub>ULX</sub> are determined analytically.

The mass transfer rate is a parameter critical to defining the spectral shape. By definition, a source in an ultra-luminous accretion state will have a mass supply rate exceeding the Eddington rate:

$$\dot{M}_{\text{Edd}} = \frac{48\pi GM}{c\kappa_T} \simeq 3 \times 10^{-8} m M_\odot \text{ yr}^{-1} \quad (2)$$

where  $m$  is the mass of the accretor in units of  $M_\odot$ . It is often convenient to define a dimensionless mass transfer rate  $\dot{m}$ , as follows:

$$\dot{m} = \dot{M}/\dot{M}_{\text{Edd}} \quad (3)$$

A source in the ultra-luminous state would therefore be expected to have  $\dot{m} \gg 1$ . The *intrinsic* luminosity of the disk then depends logarithmically on the dimensionless mass transfer rate (Poutanen et al. 2007):

$$L_{\text{bol}}^{\text{int}} = L_{\text{Edd}}(1 + 0.6\ln(\dot{m})) \quad (4)$$

Following King (2009), the *observed*, or apparent, luminosity may differ from the intrinsic luminosity due to geometrical beaming, such that  $L_{\text{obs}} = L_{\text{bol}}^{\text{int}}/b$ . Under this formalism, the beaming factor  $b$  is related to the funnel opening angle ( $\theta$ ) as  $b = \Omega/4\pi$ , where  $\Omega = 2 \times 2\pi(1 - \cos\theta)$  is the combined solid angle from both cones of the wind funnel. In this way, the beaming factor ( $b$ ) also sets the probability that the source is observed:

$$b = P_{\text{obs}}(\theta) = 1 - \cos\theta \quad (5)$$

For large funnel opening angles ( $\theta \sim 90^\circ$ ), the beaming factor approaches unity, and there is a high probability the source is observed. For very small opening angles, by contrast, the beaming factor is small and the observed luminosity of the central disk is boosted, but the probability that the source is observed at X-ray wavelengths is low.

King (2009) suggest that the beaming factor itself may depend on the mass transfer rate, and we adopt this view for our model to reduce the number of predetermined parameter values. Specifically, we parameterize  $b$  in terms of the mass transfer rate as follows:

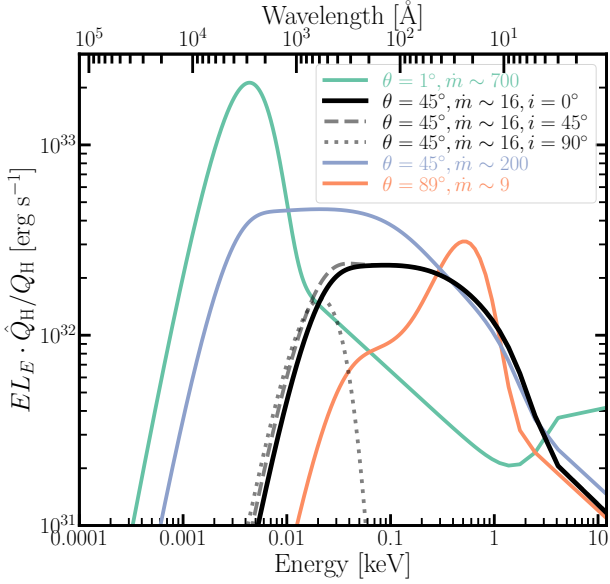


**Figure 3.** The broad-band SED for the SXP<sub>ULX</sub> (i.e., `simpl(sirf)` in `XSPEC`) under differing assumptions about the funnel opening angle ( $\theta$ ), the mass transfer rate onto the BH ( $\dot{m}$ ), and the viewing angle ( $i = 0^\circ$  for a face-on observer;  $i = 90^\circ$  for an edge-on observer). All SEDs correspond to a  $20 M_\odot$  BH, and are normalized to the same intrinsic bolometric luminosity. The SED<sub>ULX</sub> (intrinsic model for the photoionization simulations) is shown as the solid black line, while SEDs with different viewing angles for the same  $\theta$  and  $\dot{m}$  are shown as dashed and dotted gray lines. In the case of an edge-on observer ( $i = 90^\circ$ ) the source emits mostly in the EUV. The solid green and orange lines show the effect of changing the funnel opening angle ( $\theta$ ), which changes the corresponding mass transfer rate, while the solid blue SED demonstrates the effect of uncoupling  $\theta$  and  $\dot{m}$  and allowing for a very high mass transfer rate with a moderate funnel opening angle.

$$b = \begin{cases} 1 & \dot{m} \leq 8.5 \\ (8.5/\dot{m})^2 & \dot{m} > 8.5 \end{cases} \quad (6)$$

By this definition, high mass transfer rates ( $\dot{m} > 200$ ) lead to small funnel opening angles, correspondingly small beaming factors, and therefore low probabilities for observing hard emission from the source. The model for the SED<sub>ULX</sub> used in this work has  $\theta = 45^\circ$ , and therefore  $b = P_{\text{obs}}(\theta) \sim 0.3$  and  $\dot{m} \sim 16$ , using Equations 5–6. In Figure 3 we show the SED<sub>ULX</sub> in black for various viewing angles ( $i = 0^\circ$  for the intrinsic model) alongside SEDs under different assumptions for the funnel opening angle and mass transfer rate and the relation between these parameters; these are discussed in more detail in Section 6.1.

With  $\theta$ ,  $\dot{m}$ , and  $m$  specified as above, it is relatively straightforward to calculate a number of the remaining critical parameters setting the shape of the `sirf` component of the SED<sub>ULX</sub> model (see Table 1). The spherization radius where the outflow is launched is calculated as  $R_{\text{sph}} = \frac{18}{\cos\theta} R_S \dot{m}$ , where  $R_S = 2 \frac{GM}{c^2}$  is the Schwarzschild radius<sup>4</sup>. The minimum inner radius for the photosphere ( $r_{\text{ph,in}}$ ) in units of this spherization radius ( $R_{\text{sph}}$ ) can be calculated as the innermost stable circular orbit ( $R_{\text{isco}} = 6 \frac{GM}{c^2}$ ) divided by  $\theta$ :

$$r_{\text{ph,in}} = \frac{1}{6\dot{m}} \quad (7)$$

The corresponding temperature at the inner edge of the wind funnel ( $T_{\text{funnel, in}}$ ), and the outer radius of the photosphere ( $r_{\text{ph,out}}$ ), also in units of the spherization radius, can be calculated analytically following Abolmasov et al. (2009):

$$T_{\text{funnel, in}} = 0.038(\Omega' \tan^2\theta r_{\text{ph,in}})^{-1/4} \times (2.8 + 0.6 \ln \dot{m}_3)^{1/4} \dot{m}_3^{-1/2} M_{10}^{1/4} \text{ keV} \quad (8)$$

$$r_{\text{ph,out}} \simeq \left[ \frac{2\Omega' \sqrt{\dot{m}}}{(1+\alpha)\sqrt{\cos\theta}} \right]^{1/(1+\alpha)} \quad (9)$$

where  $\dot{m}_3 = \dot{M}$  in units of  $10^3 \dot{M}_{\text{Edd}}$ ,  $\Omega' = -8\pi \ln \sin\theta$ ,  $M_{10}$  is the mass of the BH in units of  $10 M_\odot$ , and  $\alpha$  is the exponent describing the velocity law for the wind. Our Equation 8 corresponds to Equation 35 from Abolmasov et al. (2009), where we have assumed  $T_{\text{funnel, in}}$  is equal to the temperature at the bottom of the funnel ( $T_{\text{bot}}$ ) for the `sirf` template.

The remainder of the parameters for the `sirf` component of the SED<sub>ULX</sub> model are selected, as summarized in Table 1, where notation corresponds to symbols used in `XSPEC`. In particular, the SED<sub>ULX</sub> model employed in the photoionization simulations has  $i = 0^\circ$  (such that the cloud in the photoionization modeling described in Section 4 sees all components of the inflow/outflow),  $\alpha = 0$  (no acceleration for the wind),  $\gamma = 4/3$  (default value, the adiabatic index for the inner parts of the accretion flow), and  $\text{irrad.} = 4$  (number of iterations for irradiation). The normalization for the SED<sub>ULX</sub> model is calculated following the theoretical scaling of  $L_X/M_0$  with starburst age from Fragos et al. (2013b) as described in Section 2.1.

Finally, we convolve the `sirf` component of the SED<sub>ULX</sub> model with a Comptonization component

<sup>4</sup> This is proportional to the dimensionless spherization radius from Poutanen et al. (2007), given as  $r_{\text{sph}} = 5/3 \times \dot{m}$ , but critically also depends on the geometry of the funnel.

(`simpl`) in order to reproduce the typical high-energy ( $> 2$  keV) shape of observed ULX spectra. All parameters values of the `simpl` component are selected, namely the photon power-law index  $\Gamma = 2.5$ , and the scattering fraction (10%). For observed ULXs fit with the `simpl` convolution component, the recovered Comptonization parameters are broadly consistent with those listed in Table 1; however, such parameters are typically not tightly constrained from observations (e.g. Walton et al. 2013, 2014). As such, we consider the  $\text{SED}_{\text{ULX}}$  shape at energies  $\gtrsim 2$  keV, which is set by the `simpl` component, critical for comparisons to apparent observed  $L_X$ , but not particularly physically informative in terms of shape.

We make this  $\text{SED}_{\text{ULX}}$  model available as part of this work (Section 5.4), noting that it represents *only* the accretion flow, and therefore does not account for any emission related to the putative donor star. We have implemented the  $\text{SED}_{\text{ULX}}$  without selecting a unique donor star in part because the distribution of such sources for ULXs, though the subject of intense study, is still not well-constrained theoretically or observationally (e.g., Liu et al. 2004; Copperwheat et al. 2005; Tao et al. 2011; Motch et al. 2011; Soria et al. 2012; Grisé et al. 2012b; Gladstone et al. 2013; Heida et al. 2014, 2016, 2019a,b; Lau et al. 2019; Wiktorowicz et al. 2017, 2021). Identifying unique optical, UV, or IR counterparts at the extragalactic distances to most ULXs remains challenging. Constraining donor stars SEDs through photometry or spectroscopy is likewise difficult given uncertainties such as the contribution of emission from the accretion flow itself, and effects of irradiation of the donor star. In the photoionization simulations that follow, the  $\text{SED}_{\text{ULX}}$  is always coupled to the SED for a stellar population, thereby making a range of potential donor stars available to the accretor. We consider this a sensible choice for modeling the spectra or nebular emission from simple *populations*; however, comparison of this model to broad-band observations for an *individual* ULX would warrant matching the  $\text{SED}_{\text{ULX}}$  with the spectrum for an appropriate donor star, and therefore further customization of the  $\text{SED}_{\text{ULX}}$  model presented here.

### 3. CONSTRUCTING A PHYSICALLY CONSISTENT COMPOSITE POPULATION

In constructing a composite population with contributions from both stars and ULXs, we start from the assumption that the  $\text{SXP}_{\text{ULX}}$  can be specified using the same parameters governing the evolution of the stellar population. Ideally, the  $\text{SXP}_{\text{ULX}}$  contribution would be determined directly from stellar population synthesis models themselves; however, there is currently no

publicly available set of models for which properties of both the stellar and accreting compact object population are easily recoverable. Absent such models, our method aims to stitch together the  $\text{SXP}_{\text{ULX}}$  model with publicly available models for SSPs in a physically consistent way.

To specify the stellar component (i.e., SSPs) of the composite population, we opt to use Flexible Stellar Population Synthesis (FSPS) and the associated `python-fsps` bindings (Conroy et al. 2009; Conroy & Gunn 2010; Johnson et al. 2022). For the SSPs, we use the Binary Population and Spectral Synthesis (BPASSv2.2; Eldridge et al. 2017) models available in FSPS, which set the prescriptions for the IMF, as well as metallicity- and time-dependent properties of the spectra for the stellar population. We use the spectra from BPASS v2.2 that include products of binary evolution, noting that this version does not explicitly include accreting compact objects as part of the population. As a consequence of using the default BPASS SSPs included in FSPS, the IMF has an upper mass cutoff of  $100 M_{\odot}$ , a low-mass ( $0.1\text{--}0.5 M_{\odot}$ ) IMF slope of  $-1.30$ , and a high-mass ( $0.5\text{--}100 M_{\odot}$ ) IMF slope of  $-2.35$  (matching the IMF used in the theoretical models from Fragos et al. 2013b). For the BPASS models  $Z = 0.02$  corresponds to  $Z_{\odot}$ . By convention in FSPS, each SSP is normalized by stellar mass.

We construct a grid of BPASS SSPs in age and metallicity corresponding to the selected burst ages and metallicities<sup>5</sup> at which we model the  $\text{SXP}_{\text{ULX}}$  ( $t_{\text{burst}} \sim \{1, 3, 5, 8, 10, 15, 20\}$  Myr, and  $Z = \{0.0001, 0.002, 0.02\}$ ). Because the  $\text{SXP}_{\text{ULX}}(t_{\text{burst}}, Z)$  models we produce are already in terms of  $1 M_{\odot}$  stellar mass, we simply add them to the corresponding SSP to produce the composite  $[\text{SXP}_{\text{ULX}} + \text{SSP}](t_{\text{burst}}, Z)$ . This ensures some measure of physical consistency between the SSP and SXP, for example, accounting for the delay between formation of high mass stars and the appearance of the first X-ray emitting accreting BHs. This procedure also incorporates metallicity dependent effects on the SSP and SXP evolution. For example, the increase in radiative output from the  $\text{SXP}_{\text{ULX}}$  with decreasing metallicity shown in Figure 1 is likely the consequence of weaker line-driven winds for massive stars at low metallicities, which result in less mass and angular momentum loss from the binary. This in turn results in XRBs with more massive compact objects and tighter orbits, which facilitate

<sup>5</sup> We consider the extremely metal poor case speculative in terms of  $\text{SXP}_{\text{ULX}}$  normalization, and therefore refer to this case as  $0.01 Z_{\odot}$  throughout for simplicity, noting the true stellar metallicity from BPASS for this set of models is slightly lower ( $0.005 Z_{\odot}$ ).

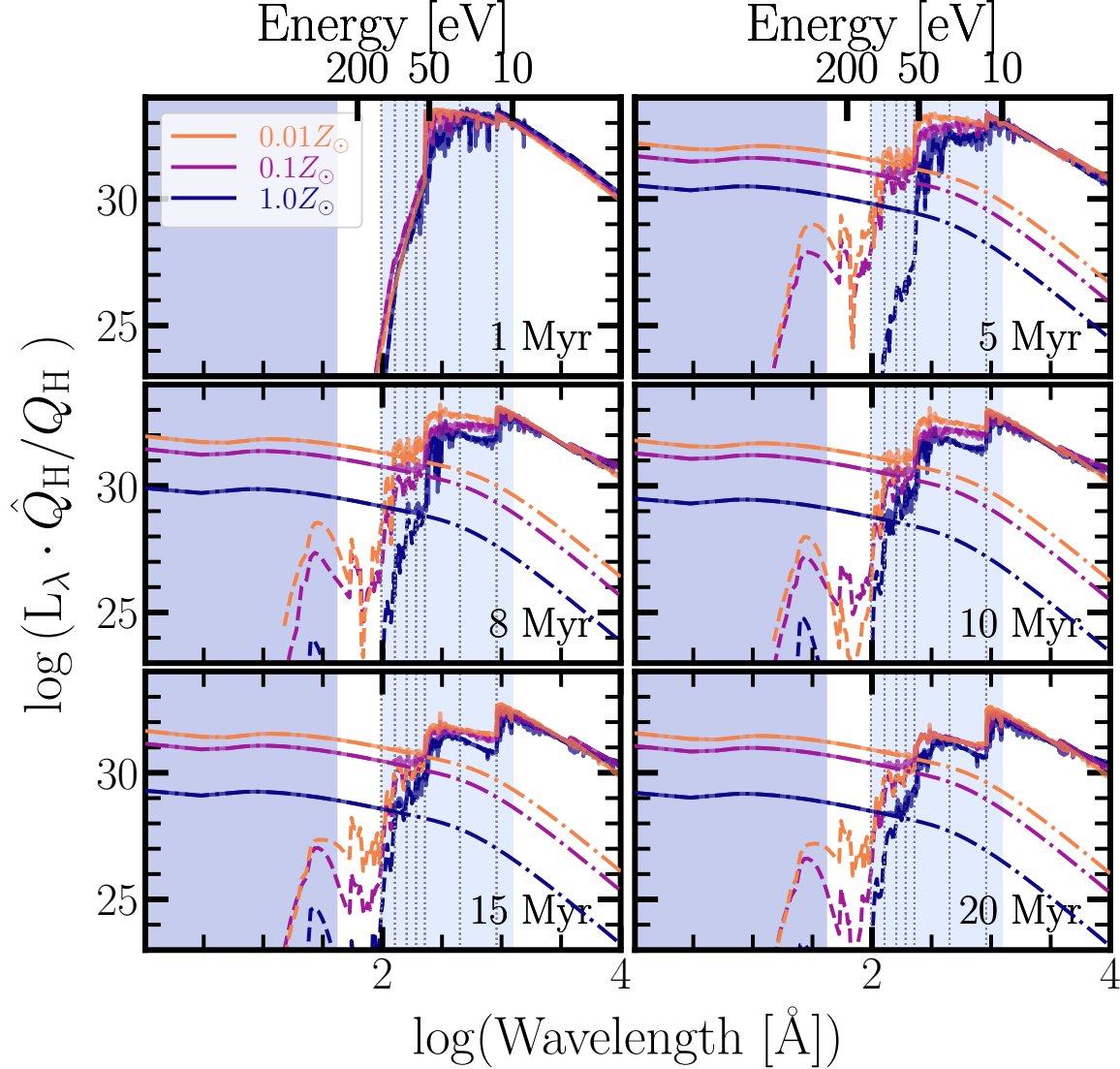


**Figure 4.** The composite  $\text{SXP}_{\text{ULX}} + \text{SSP}$  SEDs (solid lines) for the sampled metallicities (dark blue:  $Z_{\odot}$ , purple:  $0.1 Z_{\odot}$ , and orange:  $0.01 Z_{\odot}$ ) normalized to  $1 M_{\odot}$  stellar mass formed in an instantaneous burst, where the burst age is annotated in each panel. In each panel, the dash-dot line shows the  $\text{SXP}_{\text{ULX}}$  component of the composite, while the dashed line denotes the SSP contribution. The dark blue shaded region indicates the 0.5–12 keV range, while the light blue shaded region shows the EUV regime. Grey dotted vertical lines mark the ionization potentials for select lines, from high to low energies (left to right): [Ne V], [Ne IV], [O IV], C IV, He II, [Ar II], and H. The addition of the  $\text{SXP}_{\text{ULX}}$  to the corresponding SSP substantially adds to the intensity at energies  $\gtrsim 54$  eV ( $\log(\text{Wavelength } \text{\AA}) = 2.36$ ), particularly for the low-metallicity models with  $t_{\text{burst}} > 10$  Myr.

more efficient mass transfer, thereby producing more luminous sources (Linden et al. 2010; Mapelli et al. 2010). Pairing a low metallicity  $\text{SXP}_{\text{ULX}}$  (high  $L_{\text{X}}/M_0$ ) with a high metallicity SSP would therefore be inconsistent, i.e., would assume that massive stars with strong line-driven winds typically produce XRBs with tight orbits and massive accreting compact objects.

In Figure 4 we show the  $[\text{SXP}_{\text{ULX}} + \text{SSP}](t_{\text{burst}}, Z)$  models normalized to  $1 M_{\odot}$  (solid lines), where each panel corresponds to the annotated instantaneous burst age. The  $\text{SXP}_{\text{ULX}}$  and SSP components are shown as

dash-dot and dashed lines, respectively. We do not display the 3 Myr burst, as it is very similar to the 1 Myr panel, prior to  $\text{SXP}_{\text{ULX}}$  formation. In all panels, the 0.5–12 keV bandpass is highlighted via the dark blue shaded region, while the EUV range is shown in light blue. These  $[\text{SXP}_{\text{ULX}} + \text{SSP}](t_{\text{burst}}, Z)$  models, which span wavelengths  $1\text{--}10^8$  Å, are used as the spectral input for photoionization modeling with CLOUDY.

#### 4. PHOTOIONIZATION SIMULATIONS WITH CLOUDY



We perform photoionization simulations using the  $[\text{SXP}_{\text{ULX}} + \text{SSP}](t_{\text{burst}}, Z)$  models as input to CLOUDY v17.02 (Ferland et al. 2017). To construct the CLOUDY-specific input files for our photoionization simulation grid and organize the CLOUDY output, we employ a modified version of the `cloudyFSPS` code (Byler 2018). Below we describe the CLOUDY simulation set-up, relevant grid parameters, and saved output from the simulations.

For the cloud geometry in all simulations, we assume a closed spherical shell with a fixed inner radius  $R = 10^{19}$  cm and a constant density  $n_{\text{H}} = 100 \text{ cm}^{-3}$ . The cloud is ionized by a central source, which we set as the  $[\text{SXP}_{\text{ULX}} + \text{SSP}](t_{\text{burst}}, Z)$  SED, implying coincident mixing between the  $\text{SXP}_{\text{ULX}}$  and SSP components. This cloud set-up is most appropriate for radiation-bounded regions, while the assumed density is appropriate to HII regions. The chosen value for the inner radius ( $R$ ) corresponds to  $\sim 0.3\text{--}3 R_{\text{S}}$  over the entire simulation grid, where  $R_{\text{S}}$  is the Strömgren<sup>6</sup> radius.

We set  $i = 0$  for the  $\text{SED}_{\text{ULX}}$  component of the  $[\text{SXP}_{\text{ULX}} + \text{SSP}](t_{\text{burst}}, Z)$ , which is equivalent to assuming an isotropic distribution of photons from the composite spectrum is incident on the cloud. This is a simplifying assumption, but reasonable for the production of high-energy ionizing photons as considered here. The outflow component of the  $\text{SED}_{\text{ULX}}$  should be quasi-spherical, and it is this component in particular that emits strongly in the EUV (e.g., Figure 3). We consider more complex geometrical effects beyond the scope of the present work, but note that although the cloud in all simulations is subject to an isotropic distribution of photons (effective  $i = 0$ ), simulation results can be post-processed with  $i > 0$  to simulate different viewing angles for an observer.

In setting the chemical composition of the cloud, we follow the prescriptions outlined in Byler et al. (2017). In brief, we assume the gas-phase metallicity is tied to the stellar metallicity, with the gas-phase abundances set following Dopita et al. (2000). The metal abundances, except for nitrogen, are scaled to solar following the solar abundances in Anders & Grevesse (1989), while the nitrogen scaling follows that of Dopita et al. (2000). We include depletion onto dust grains again using prescriptions from Dopita et al. (2000), where depletion

factors do not depend on metallicity and are applied regardless of whether grains are included in the cloud. For these simulations, we do not include dust grains.

The  $[\text{SXP}_{\text{ULX}} + \text{SSP}](t_{\text{burst}}, Z)$  models specify the SED of the central ionizing source normalized by stellar mass. In order to set the intensity of the composite population for the CLOUDY simulations, we normalize each model by the dimensionless ionization parameter  $\mathcal{U}$ :

$$\mathcal{U} \equiv \frac{\mathcal{Q}_{\text{H}}}{4\pi R^2 n_{\text{H}} c} \quad (10)$$

where  $\mathcal{Q}_{\text{H}} \equiv \int_{\nu_0}^{\infty} \frac{f_{\nu}}{h\nu} d\nu$  is the rate of emitted photons capable of ionizing hydrogen (i.e.,  $h\nu_0 = 13.6$  eV),  $R$  is the inner cloud radius (hydrogen ionized region) in cm,  $n_{\text{H}}$  is the hydrogen number density in  $\text{cm}^{-3}$ , and  $c$  is the speed of light. By this definition, the dimensionless ionization parameter can be thought of as the density of photons relative to the density of atoms. For the simulations presented here we select seven values of  $\log \mathcal{U} = [-4.0, -3.5, -3.0, -2.5, -2.0, -1.5, -1.0]$ , a range that is typical for modeling HII regions or starbursts (e.g., Dopita et al. 2000; Kewley et al. 2013). Each model is therefore specified as  $[\text{SXP}_{\text{ULX}} + \text{SSP}](t_{\text{burst}}, Z, \log \mathcal{U})$  before being run through CLOUDY.

This intensity scaling is required to simulate a reasonable range of observed nebular continuum and emission line intensities, as the SED for a composite population per  $1 M_{\odot}$  burst mass would produce relatively few ionizing photons. Because  $R$  and  $n_{\text{H}}$  remain fixed<sup>7</sup> in our models, changing  $\log \mathcal{U}$  amounts to changing  $\mathcal{Q}_{\text{H}}$  and therefore the effective stellar mass, as more or fewer sources are needed for older and younger bursts, respectively, to produce sufficient ionizing photons to achieve the intensity specified by  $\log \mathcal{U}$ . Following the same convention as Byler et al. (2017), we define the rate of ionizing photons *per solar mass* as  $\hat{\mathcal{Q}}_{\text{H}} \equiv \mathcal{Q}_{\text{H}} / M_{\odot}$ , where  $\mathcal{Q}_{\text{H}}$  is the rate of ionizing photons corresponding to the  $\log \mathcal{U}$  that sets the intensity for a given model in the CLOUDY simulations. With this convention, output quantities can be recovered for a composite population corresponding to  $1 M_{\odot}$  stellar mass through multiplication by  $\hat{\mathcal{Q}}_{\text{H}}/\mathcal{Q}_{\text{H}}$ . This normalization of input or output intensities using  $\hat{\mathcal{Q}}_{\text{H}}/\mathcal{Q}_{\text{H}}$  is specified throughout, where appropriate.

With these parameters ( $t_{\text{burst}}$ ,  $Z$ , and  $\log \mathcal{U}$ ), the overall grid input to CLOUDY consists of 147 separate models, corresponding to different combinations of the

<sup>6</sup>  $R_{\text{S}} = (\frac{3\mathcal{Q}_{\text{H}}}{4\pi\alpha(T_{\text{e}})n_{\text{e}}n_{\text{H}}})^{1/3}$ , where  $\mathcal{Q}_{\text{H}}$  is the hydrogen ionizing photon rate,  $\alpha(T_{\text{e}})$  is the recombination rate,  $n_{\text{e}}$  is the electron density, and  $n_{\text{H}}$  is the hydrogen density. To obtain the range of  $R_{\text{S}}$  from our simulations, we calculate  $\mathcal{Q}_{\text{H}}$  directly from the input SEDs, use  $\alpha(T_{\text{e}}) = 2.6 \times 10^{-13} \text{ cm}^3 \text{ s}^{-1}$  (corresponding to  $T_{\text{e}} = 10^4$  K, as in Jaskot & Ravindranath 2016), and assume  $n_{\text{e}} = n_{\text{H}} = 100 \text{ cm}^{-3}$ .

<sup>7</sup> We note that fixing  $R$  and varying only ionizing flux means certain geometric effects are not accounted for in these models; such geometrical effects can substantially change both high-ionization and neutral line emission (e.g., Ramambason et al. 2022).

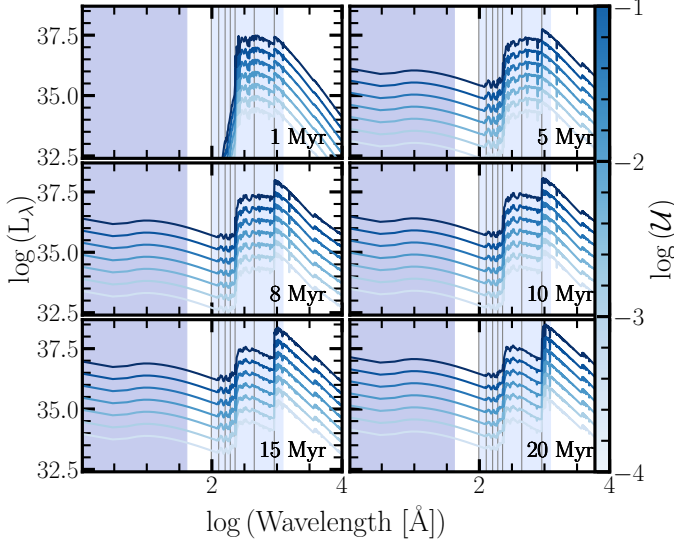


**Figure 5.** The composite SXP<sub>ULX</sub> + SSP SEDs at  $0.1 Z_{\odot}$  for a selection of instantaneous burst ages, normalized by a range of  $\log \mathcal{U}$  values, as noted in the colorbar. Models with high  $\log \mathcal{U}$  have the highest intensities, and correspond to the largest stellar mass formed in a burst. As in Figure 4, the darker blue shaded region shows the X-ray bandpass, the lighter blue shaded region encompasses the EUV regime, and the grey vertical lines denote a selection of relevant ionization potentials (13.6–126 eV, from right to left). Each composite SED is used as input for the CLOUDY photoionization simulations.

seven values for  $t_{\text{burst}}$ , three values for  $Z$ , and seven values for  $\log \mathcal{U}$ . In Figure 5, we show the [SXP<sub>ULX</sub> + SSP]( $t_{\text{burst}}$ ,  $Z$ ,  $\log \mathcal{U}$ ) models for select burst ages and the full range for  $\log \mathcal{U}$  for the  $0.1 Z_{\odot}$  case. The models with  $\log \mathcal{U} = -1$  have the highest intensities, or correspondingly, the largest stellar mass formed in a burst ( $Q_{\text{H}}/\dot{Q}_{\text{H}} \sim 10^4 - 10^6 M_{\odot}$  for  $\log \mathcal{U} = -1$  and  $t_{\text{burst}} = 1\text{--}20$  Myr).

We again employ a modified version of cloudyFSPS to create the relevant CLOUDY input files for each model in the grid, execute CLOUDY simulations, and organize the CLOUDY output files. For each grid point, we allow the CLOUDY simulations to iterate to convergence, up to a maximum number of five iterations, and set the stopping criteria for the calculations to when the cloud temperature falls below 100 K or the ionized fraction falls to 1%. Building on the nebular emission line lists presented in Byler et al. (2017) and Byler et al. (2018), we record intensities from 407 emission lines, spanning the far IR to the near UV. The full line list is included in the Appendix in Table A.1, including vacuum wavelength (Å), line name, and CLOUDY specific line ID.

## 5. RESULTS

We highlight select results illustrating the importance of the time- and metallicity-dependence of the SXP<sub>ULX</sub> implementation, and provide potential diagnostics for investigating a SXP<sub>ULX</sub> ionizing contribution. We further describe the availability of our models and simulation results.

### 5.1. Characteristics of Nebular Emission Due to SXP<sub>ULX</sub> and Potential SXP<sub>ULX</sub> Diagnostics

A key result from the photoionization simulations is that the inclusion of the SXP<sub>ULX</sub> component does not significantly alter the *broad-band* colors in the UV-to-FIR relative to the case of the BPASS SSPs alone. This can easily be seen by looking at the enhancement in total nebular (line and continuum) emission due to the addition of the SXP<sub>ULX</sub>. In Figure 6 we show the fractional contribution of the nebular emission to the total flux as a function of wavelength and burst age in the top panel, and the percentage *enhancement* in this nebular flux due to the addition of the SXP<sub>ULX</sub> in the bottom panel. The nebular contribution to the total flux is high ( $> 50\%$ ) at all wavelengths on short burst timescales ( $\leq 3$  Myr, before the SXP<sub>ULX</sub> has turned on), and in the MIR for all burst timescales simulated here. However, as the bottom panel illustrates, the enhancement in nebular emission due to the inclusion of the SXP<sub>ULX</sub> is typically very small ( $< 5\%$ ). In the broad-band sense, the major effect of the SXP<sub>ULX</sub> is therefore to slightly prolong the ionizing output relative to the SSP alone, a consequence of the imposed age-dependence of our models.

Due to the shape of the SED<sub>ULX</sub> as extended through the EUV, a key outcome from the addition of the SXP<sub>ULX</sub> is a change to the intensity of lines with excitation potentials  $\geq 54$  eV. The CLOUDY line list for our simulations (Table A.1) includes 63 lines redward of Ly $\alpha$  with ionization potential  $\geq 54$  eV (Kramida et al. 2022), of which 28 have ionization potentials in excess of 90 eV, including a number of so-called “coronal lines” (i.e., forbidden transitions with very high ionization potentials). In order to establish which of these high-excitation lines may be used as diagnostics for SXP<sub>ULX</sub> ionization, we consider lines redward of Ly $\alpha$  that satisfy the following criteria: (1) are relatively strong in the models with SXP<sub>ULX</sub> contribution, as measured in terms of median line flux relative to median flux in H $\beta$  or Pa $\beta$ <sup>8</sup> (i.e.,  $\log(\hat{f}_{\text{line}}/\hat{f}_{\text{H}\beta}) \geq -3$  or  $\log(\hat{f}_{\text{line}}/\hat{f}_{\text{Pa}\beta})$

<sup>8</sup> We use H $\beta$  as the reference line for the high-ionization lines, which are mostly in the UV and optical, and Pa $\beta$  for coronal lines in the IR.

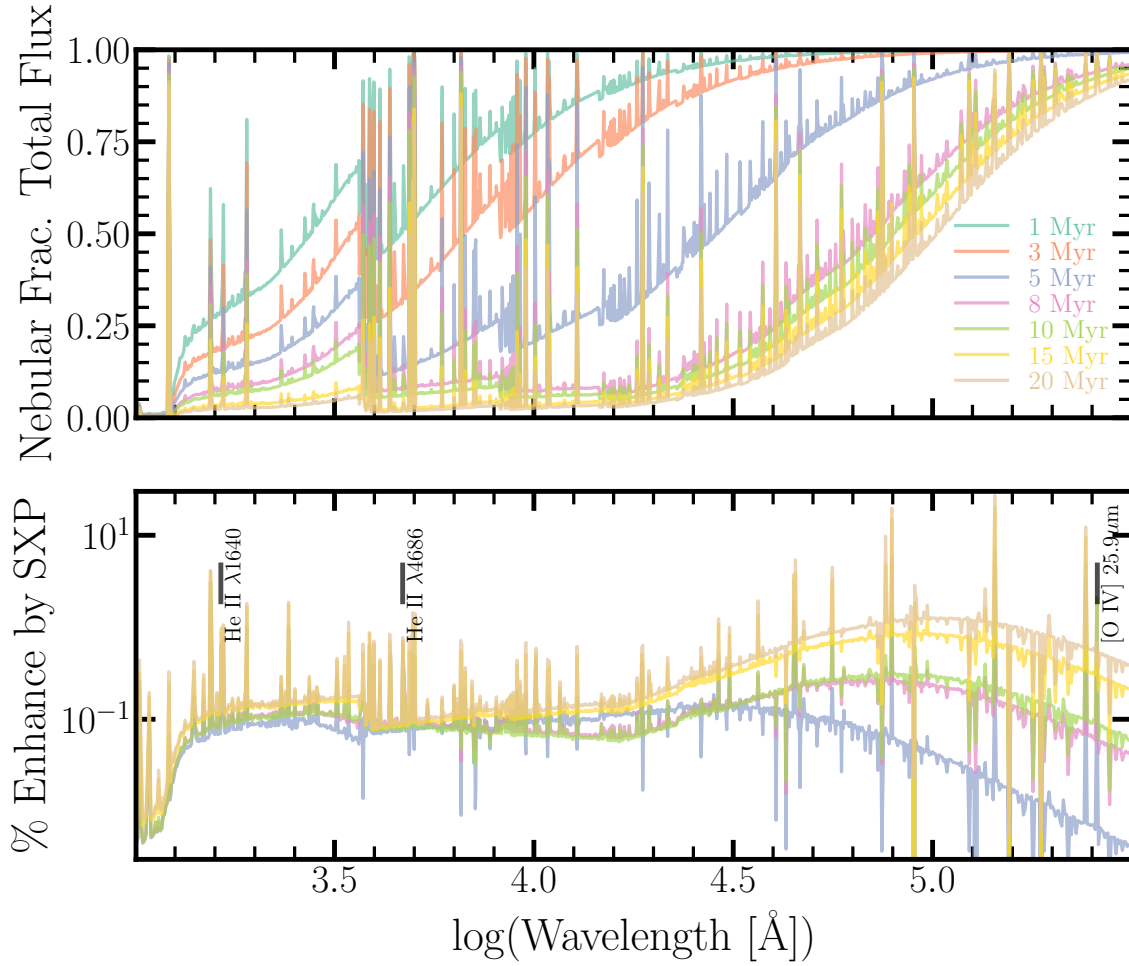


**Figure 6.** *Top:* The fractional contribution of the nebular line and continuum emission to the total flux (stellar and nebular) as a function of wavelength and instantaneous burst age for models with  $Z = 0.1 Z_{\odot}$  and  $\log \mathcal{U} = -1$ . *Bottom:* The percentage enhancement in nebular line and continuum flux due to the addition of the  $\text{SXP}_{\text{ULX}}$ . For all burst timescales simulated, the  $\text{SXP}_{\text{ULX}}$ -driven enhancement in the total nebular emission is typically small ( $< 5\%$ ). The black labels denote high-ionization species whose nebular *line* intensity is particularly enhanced due to the inclusion of the  $\text{SXP}_{\text{ULX}}$  component.

$\geq -3$ ); and (2) have a median enhancement in line flux by a factor of  $2\times$  relative to the SSP-only models ( $\log(\tilde{f}_{\text{line,SXP+SSP}}/\tilde{f}_{\text{line,SSP}}) \geq 0.3$ ). There are only a select few emission lines satisfying both of these criteria: He II  $\lambda 1640, 4686$ , and [O IV]  $25.8832\mu\text{m}$ . We annotate these lines in Figure 6, and note them in Table A.1 (\* flag).

In Figures 7–9 we show emission line diagnostic diagrams in the UV, optical, and IR, respectively, to highlight the potential for uncovering ionization due to an  $\text{SXP}_{\text{ULX}}$  using these lines passing both the criteria as outlined above. In general, diagnostic diagrams such as these are constructed using lines relatively close in wavelength to reduce the effects of reddening and make the lines used in the diagnostic accessible with

a single instrument, reducing uncertainties due to cross-calibration. In all line diagnostic diagrams that follow, the  $[\text{SXP}_{\text{ULX}} + \text{SSP}](t_{\text{burst}}, Z, \log \mathcal{U})$  models (i.e., models *with*  $\text{SXP}_{\text{ULX}}$  contribution) are shown as the solid lines, where orange to dark blue lines represent metallicities from  $Z = 0.01$ – $1 Z_{\odot}$  and light blue to dark blue lines represent ionization parameters from  $\log \mathcal{U} = -4$  to  $-1$ . For all grids in the diagnostic plots, the star denotes the model with lowest metallicity ( $0.01 Z_{\odot}$ ) and highest ionization parameter ( $\log \mathcal{U} = -1$ ). The BPASS SSP-only models are shown as slightly transparent, dashed lines in the background with the same color scheme. In cases where the models with  $\text{SXP}_{\text{ULX}}$  contribution are indistinguishable from SSP-only models (e.g., burst ages  $< 5$  Myr), only solid lines are shown.

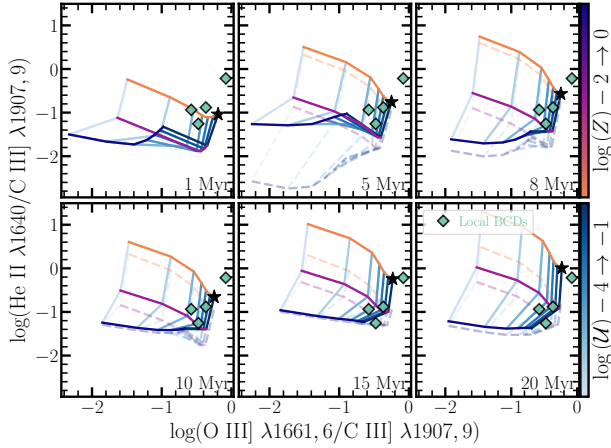


**Figure 7.** Potential UV diagnostic diagram for  $\text{SXP}_{\text{ULX}}$  ionization, as a function of instantaneous burst age. The  $[\text{SXP}_{\text{ULX}} + \text{SSP}](t_{\text{burst}}, Z, \log \mathcal{U})$  grid is shown as solid lines, where orange to dark blue lines represent metallicities  $0.01 Z_{\odot}$ – $Z_{\odot}$  and light blue to dark blue lines represent  $\log \mathcal{U} = -4$  to  $-1$ , as illustrated by the colorbars. In all panels, the star represents the  $0.01 Z_{\odot}$  and  $\log \mathcal{U} = -1$  grid point. The dashed transparent lines in the background show the corresponding grid with SSP ionizing contribution only. A sample of local BCDs for which these UV lines have been measured are shown as cyan diamonds, where the uncertainties in line ratios are smaller than the plotted points (Senchyna et al. 2017). The addition of the  $\text{SXP}_{\text{ULX}}$  hardens the ionizing spectrum at a given  $\log \mathcal{U}$ , thereby increasing the intensity of He II  $\lambda 1640$  relative to C III]  $\lambda 1907,9$ . This effect is more pronounced at solar metallicity for  $t_{\text{burst}} = 5$  Myr, following depletion of WR stars, and low metallicities with  $t_{\text{burst}} > 10$  Myr (bottom panels), following depletion of the most massive stars.

For the UV diagnostic in Figure 7, the  $(\text{O III}] \lambda 1661,6) / (\text{C III}] \lambda 1907,9)$  ratio is sensitive to the ionization parameter, C/O ratio (i.e., abundance pattern, see discussion in Section 5.3), and uses lines that are relatively strong in the UV (Byler et al. 2018). The He II  $\lambda 1640 / \text{C III}] \lambda 1907,9$  ratio in this same diagram is sensitive to the hardness of the ionizing spectrum. For burst timescales where the  $\text{SXP}_{\text{ULX}}$  contributes ( $\geq 5$  Myr), this diagnostic illustrates that the ionizing spectrum is harder at all metallicities relative to the SSP-only models due to the inclusion of the  $\text{SXP}_{\text{ULX}}$ , resulting in stronger intensity of He II  $\lambda 1640$  relative to C III]  $\lambda 1907,9$  at the same ionization parameter.

For this set of line diagnostics, we compare the  $[\text{SXP}_{\text{ULX}} + \text{SSP}](t_{\text{burst}}, Z, \log \mathcal{U})$  grid to a sample of local blue compact dwarf (BCD) galaxies from Senchyna et al. (2017) for which these same lines have been measured. While most of the data points from the BCDs (cyan diamonds) are consistent with both the SSP-only

and  $[\text{SXP}_{\text{ULX}} + \text{SSP}](t_{\text{burst}}, Z, \log \mathcal{U})$  grid for ionization parameters  $\log \mathcal{U} \geq -3.0$ , the inclusion of the  $\text{SXP}_{\text{ULX}}$  slightly broadens the range of metallicities consistent with the data points; whereas the BCD sample is consistent with the SSP-only grid for  $Z \leq 0.1 Z_{\odot}$ , the composite grid extends the consistency to  $0.1 Z_{\odot} \leq Z < Z_{\odot}$  for older burst ages. This BCD sample has a median gas-phase metallicity of  $\sim 0.15 Z_{\odot}$ , suggesting that if  $\text{SXP}_{\text{ULX}}$  ionization is important in these galaxies the population may be dominated by star formation bursts  $\geq 10$  Myr; however, given the relative sparsity of the metallicity sampling in our grids and in the absence of a more detailed age analysis—which we consider beyond the scope of this work—it is not clear from this qualitative comparison whether the SSP-only or  $\text{SXP}_{\text{ULX}}$  grid is preferred for such galaxies. Nonetheless, the comparison serves to illustrate how the addition of the  $\text{SXP}_{\text{ULX}}$  alters the parameter space spanned by the grid, therefore changing the range of physical properties consistent with the observed population. In the case of Figure 7, the addition of the  $\text{SXP}_{\text{ULX}}$  hardens the ionizing spectrum at a given  $\log \mathcal{U}$ , which in effect mimics an SSP with slightly lower metallicity.

For an optical emission line diagnostic we present Figure 8, where the  $[\text{N II}] \lambda 6584 / \text{H}\alpha$  ratio is sensitive to metallicity and  $\log \mathcal{U}$  (among other parameters, e.g., Kewley et al. 2013), and the He II  $\lambda 4686 / \text{H}\beta$  ratio again probes the hardness of the radiation field. Here we compare to a sample of star-forming galaxies with strong nebular He II emission from SDSS identified by Shirazi & Brinchmann (2012). A little under half of this sample lack Wolf-Rayet (WR) star features in their spectra (“Non-WR”; red triangles), while the remaining galaxies show evidence for broad emission line features due to the presence of WR stars (“WR”; blue circles). In general, SSP-only models have a difficult time reproducing the observed range of He II  $\lambda 4686 / \text{H}\beta$ , as the dashed grids in Figure 8 illustrate. The  $[\text{SXP}_{\text{ULX}} + \text{SSP}](t_{\text{burst}}, Z, \log \mathcal{U})$  grid is capable of reproducing the observed intensities for a subset of these data points, notably those without clear WR features in their spectra, but only for  $t_{\text{burst}} > 10$  Myr and lower metallicity ( $Z \sim 0.1 Z_{\odot}$ ). In this case, the ability of the  $[\text{SXP}_{\text{ULX}} + \text{SSP}](t_{\text{burst}}, Z, \log \mathcal{U})$  grid to explain a subset of the galaxies with strong He II/ $\text{H}\beta$  where SSP-only models cannot is again a consequence of a harder radiation field due to the addition of the  $\text{SXP}_{\text{ULX}}$ . However, the magnitude of the increase to the ionizing photon rate due to the  $\text{SXP}_{\text{ULX}}$  is strongly dependent on SFH, as we discuss in more detail in Sections 5.2 and 6.1.

Interestingly, the observed WR feature galaxies are difficult to reproduce using either the models with



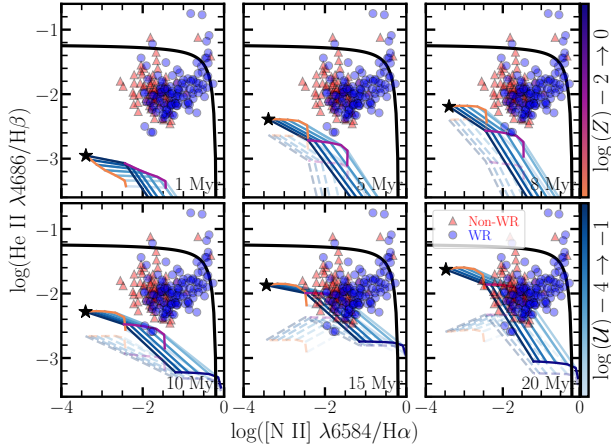


**Figure 8.** Same as Figure 7, but for a potential optical diagnostic diagram accounting for the inclusion of  $\text{SXP}_{\text{ULX}}$  ionization. The data points are a sample of star-forming galaxies from Shirazi & Brinchmann (2012) with strong nebular He II  $\lambda 4686$  emission (red triangles: galaxies without WR star features, blue circles: galaxies with WR star features). The black solid line is the empirically derived relation from Shirazi & Brinchmann (2012) to separate ionization due to star formation (below the line) versus ionization due to active galactic nuclei or composite populations (above the line). The models with  $\text{SXP}_{\text{ULX}}$  contribution overlap with the observed intensities for some of the Non-WR feature galaxies, particularly for  $t_{\text{burst}} > 10$  Myr and  $Z \leq 0.1 Z_{\odot}$ ; however, neither the  $[\text{SXP}_{\text{ULX}} + \text{SSP}](t_{\text{burst}}, Z, \log \mathcal{U})$  nor the SSP-only grids are capable of reproducing some of the more extreme galaxies, particularly those with detected WR features and higher N II/H $\alpha$  near the empirical maximum starburst line.

$\text{SXP}_{\text{ULX}}$  ionizing contribution or SSP-only photoionization. This is primarily because such galaxies have large ratios of both He II  $\lambda 4686/\text{H}\beta$ , implying hard ionizing spectra, and [N II]  $\lambda 6584/\text{H}\alpha$ , implying higher metallicities. We explore metallicity in the context of this diagnostic in Section 5.3 and alternative ionizing sources in Section 6.3.2, and here comment instead on the effect of stellar wind contamination of nebular emission. Lines such as He II can be produced either via stellar winds (broad emission line component) or photoionization (narrow emission line). Moderately good spectral resolution is therefore needed to distinguish the broad stellar from narrow nebular components for such lines (Brinchmann et al. 2008). If not fully resolvable, residual emission from the broader stellar wind component could enhance the line intensity assumed to be purely nebular. It is likely that stellar wind contamination, if present, operates preferentially to inflate line intensities at higher metallicities, where line driven winds from

massive stars are stronger (Vink et al. 2001). It is therefore important to consider the presence and magnitude of potential stellar wind contamination in observations of such nebular line species, particularly at higher metallicities, when comparing to the purely nebular line emission determined from photoionization simulations (e.g., Byler et al. 2018).

In the IR, we consider the diagnostic presented in Figure 9 for lines accessible with *JWST* (e.g., Weaver et al. 2010). Here the [O IV]  $25.9\mu\text{m}/[\text{Ne III}]$   $15.66\mu\text{m}$  ratio is sensitive to hardness of the ionizing spectrum, while [Ne III]  $15.66\mu\text{m}/[\text{Ne II}]$   $12.81\mu\text{m}$  is primarily sensitive to the ionization parameter. For this diagnostic, we include the classification regions from Richardson et al. (2022) for ionization due to pure star-formation (SF), SF/active galactic nuclei (AGN), and pure AGN, as well as the results from photoionization simulations for a  $10^3 M_{\odot}$  IMBH with fractional contribution 4–16% relative to a 20 Myr BPASS SSP (described in more detail in Section 6.3.2). The  $[\text{SXP}_{\text{ULX}} + \text{SSP}](t_{\text{burst}}, Z, \log \mathcal{U})$  grid is largely consistent with the pure SF region in this diagnostic, though offset from the SSP-only grid, again demonstrating how the addition of the  $\text{SXP}_{\text{ULX}}$  hardens the ionizing spectrum. The models including  $\text{SXP}_{\text{ULX}}$  contribution veer into the composite region for some of the solar metallicity  $t_{\text{burst}} = 5$  Myr models, and into the AGN ionization region only for lowest metallicities ( $\lesssim 0.1 Z_{\odot}$ ) and highest ionization parameters ( $\log \mathcal{U} > -3$ ) for bursts with  $t_{\text{burst}} > 10$  Myr. This indicates, not surprisingly, that the  $[\text{SXP}_{\text{ULX}} + \text{SSP}](t_{\text{burst}}, Z)$  photoionization signature looks less like pure SF when the fractional contribution of the  $\text{SXP}_{\text{ULX}}$  component relative to the SSP is most pronounced. As in Figure 7, this occurs when the strongest ionizing components of the stellar population are depleted, namely WR stars ( $\sim 5$  Myr at roughly solar metallicities) and the most massive stars that will explode as supernovae or collapse to a BH ( $> 10$  Myr). We note that the  $\text{SXP}_{\text{ULX}}$  grid does *not* significantly overlap with IMBH grids, suggesting some power in this emission line diagnostic for distinguishing between ionization due to BHs separated by orders of magnitude in mass; however, this too depends on how the accreting BH (at any mass) is scaled relative to the stellar population, a point that we return to in more detail in Section 6.3.2.

Finally, we comment on high-ionization lines that do not satisfy both criteria in terms of strength relative to H $\beta$  or Pa $\beta$  and enhancement relative to the SSP-only case. These lines fall broadly into three categories: (1) lines that are strong relative to H $\beta$  or Pa $\beta$ , but not significantly enhanced relative to the SSP-only models (flagged with † in Table A.1); (2) lines that are weak

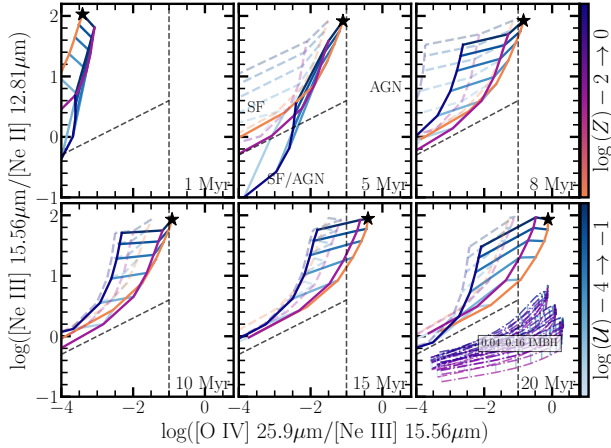


**Figure 9.** Same as Figure 7, but for a potential IR diagnostic diagram for  $\text{SXP}_{\text{ULX}}$  ionization. The dot-dash grids are photoionization simulations of a  $10^3 M_{\odot}$  IMBH at different fractional contributions relative to a 20 Myr SSP from Richardson et al. (2022), where the color scheme is the same as for the  $[\text{SXP}_{\text{ULX}} + \text{SSP}](t_{\text{burst}}, Z, \log \mathcal{U})$  grid for values  $\log \mathcal{U}$  and  $Z$  in common between the grids. The dashed lines show potential classification regions for pure star-formation ionization, composite star-formation and AGN ionization, and pure AGN ionization, also from Richardson et al. (2022), as annotated in the center top panel.

relative to  $\text{H}\beta$  or  $\text{Pa}\beta$ , but are significantly enhanced relative to the SSP-only models (flagged with ‡ in Table A.1); or (3) lines that have zero flux for three models (flagged with || in Table A.1). Lines flagged with † in Table A.1 have a median  $\log(\tilde{f}_{\text{line}}/\tilde{f}_{\text{H}\beta}) \sim -3$  and median enhancement of  $1.004\times$  in flux relative to the SSP-only models. By contrast, lines flagged with ‡ in Table A.1 have  $\log(\tilde{f}_{\text{line}}/\tilde{f}_{\text{Pa}\beta}) \sim -9$ , but median enhancement of  $47000\times$  in line flux relative to the SSP-only models. The latter case encompasses many coronal lines with ionization potentials  $> 90$  eV, i.e., the regime where the SSP provides relatively little flux, but the  $\text{SXP}_{\text{ULX}}$  component is substantial. As such, there is a higher diagnostic potential for discerning the  $\text{SXP}_{\text{ULX}}$  ionization contribution using coronal lines, many of which are in the IR, but only if the fractional contribution of the  $\text{SXP}_{\text{ULX}}$  relative to the SSP is high enough to boost the line strengths into an easily detectable range.

We illustrate these two cases—moderately strong lines only marginally enhanced by the  $\text{SXP}_{\text{ULX}}$  and weak lines heavily enhanced due to the addition of the  $\text{SXP}_{\text{ULX}}$ —via additional emission line diagnostics in Figures 10–12. In Figure 10, we show the  $[\text{SXP}_{\text{ULX}} + \text{SSP}](t_{\text{burst}}, Z, \log \mathcal{U})$  grid relative to the same sample of local BCD galaxies from as in Figure 7. Here, the grid with

$\text{SXP}_{\text{ULX}}$  contribution is only slightly offset to higher values of  $\text{C IV } \lambda 1548,51/\text{O III } \lambda 1661,6$  compared to the SSP-only grid. The lack of overlap between some of the galaxies and the grids in this diagnostic is likely a function of the adopted C/O ratio for the simulations in this work, which we discuss in more detail in Section 5.3.

In Figures 11–12, we show emission line diagnostics in the optical and IR that include the high-ionization line  $[\text{Ne V}]$ . For these emission line diagnostics, the addition of the  $\text{SXP}_{\text{ULX}}$  has a profound effect on the grid relative to the SSP-only case, given the ratio of  $[\text{Ne V}]/[\text{Ne III}]$  compares lines with ionization potentials of  $\sim 126$  eV and 64 eV, respectively. In Figure 11, the SSP-only models rarely reach  $\log([\text{Ne V } \lambda 3426]/[\text{Ne III } \lambda 3870]) > -5$ , while the grid with  $\text{SXP}_{\text{ULX}}$  contribution begins to populate the composite region for low metallicities and high-ionization parameters (classification regions from Cleri et al. 2023). In Figure 12, the  $[\text{SXP}_{\text{ULX}} + \text{SSP}](t_{\text{burst}}, Z, \log \mathcal{U})$  grid traces out a relatively narrow vertical track, distinct from the SSP-only and IMBH photoionization cases. However, for both of these diagnostics, the potential power for discerning  $\text{SXP}_{\text{ULX}}$  contribution to the ionizing photon budget comes at the expense of line strength. The ratio of  $[\text{Ne V } 14.3\mu\text{m}]/[\text{Ne III } 15.56\mu\text{m}]$  traced out by the grid with  $\text{SXP}_{\text{ULX}}$  contribution spans roughly 10 orders of magnitude. Such lines are therefore undetectable for pure star-formation ionization and only potentially detectable (e.g., with *JWST*) with an  $\text{SXP}_{\text{ULX}}$  ionizing contribution for a narrow range in  $\log \mathcal{U}$ ,  $t_{\text{burst}}$ , and  $Z$ . This implies that very high-ionization species such as  $[\text{Ne V}]$  or  $[\text{Ar V}]$  may be more reliable diagnostics of AGN or IMBH photoionization rather than  $\text{SXP}_{\text{ULX}}$  ionizing contribution; however, the potential selection biases inherent in using particular lines should be considered in assessing the reliability of any such classification diagnostic (e.g., Richardson et al. 2022).

## 5.2. Consequences of Time Dependence of the $\text{SXP}_{\text{ULX}}$ Relative to the SSP

The key parameters affecting the time-dependence of the nebular emission from the  $[\text{SXP}_{\text{ULX}} + \text{SSP}](t_{\text{burst}}, Z, \log \mathcal{U})$  grid are (1) the selection to impose a delay time for the  $\text{SXP}_{\text{ULX}}$  to turn on and; (2) the combination thereafter with SSPs of corresponding  $t_{\text{burst}}$ . Imposing a delay time creates a scenario in which the  $\text{SXP}_{\text{ULX}}$  prolongs the ionizing output of the population beyond that of the products of binary evolution already included in BPASS, as would be expected if the  $\text{SXP}_{\text{ULX}}$  component is indeed descended from the stellar component, allowing time for compact object formation and accretion to begin. In this way, the  $\text{SXP}_{\text{ULX}}$ , or ac-

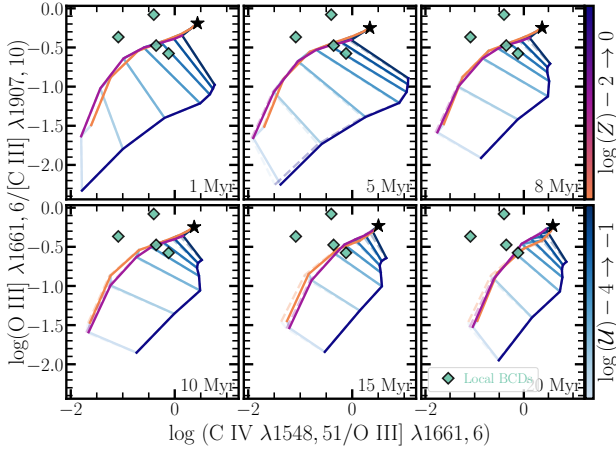


**Figure 10.** A UV emission line diagnostic where the  $\text{SXP}_{\text{ULX}}$  contribution does not change the high-ionization line species appreciably relative to the SSP-only grid. The cyan diamonds are again a sample of local BCDs for which these UV lines have been measured (Senchyna et al. 2017). The lack of overlap between some of the galaxies and either grid for this diagnostic is likely a function of adopted C/O ratio for the photoionization modeling in this work.

creting compact objects in general, are another way of rejuvenating the ionizing power from a population.

In spite of this, the magnitude of the *additional* contribution of the  $\text{SXP}_{\text{ULX}}$  to the emergent nebular emission has time-dependent limits by virtue of being coupled to the time evolution of the SSPs. Although the absolute  $L_X/M_0$  scaling for the  $\text{SXP}_{\text{ULX}}$  is largest for younger instantaneous bursts at all metallicities (Figure 1), the  $\text{SXP}_{\text{ULX}}$  generally hardens the incident ionizing spectrum more profoundly *relative to the BPASS SSPs* at older burst ages. That is, the fractional contribution of the  $\text{SXP}_{\text{ULX}}$  to the ionizing photon budget is typically highest for burst ages  $> 10$  Myr in the models considered here. This corresponds to the timescale on which the harder components of the stellar ionizing spectrum have been depleted (e.g., WR and other very massive stars), while the  $\text{SXP}_{\text{ULX}}$  component remains appreciable. Given the imposed delay time and coupling with BPASS SSPs, the  $\text{SXP}_{\text{ULX}}$  contribution to the total rate of ionizing photons is  $\lesssim 2\%$  for burst ages between 5–10 Myr, and increases only to 5–7% on timescales  $> 10$  Myr.

The consequences of this time dependence are especially evident in Figure 11, where the local EELGs are consistent with the models with  $\text{SXP}_{\text{ULX}}$  contribution for a narrow range of the grid corresponding to  $\sim 0.1 Z_\odot$ ,  $\log \mathcal{U} > -2$ , and  $t_{\text{burst}} > 10$  Myr. This suggests  $\text{SXP}_{\text{ULX}}$  photoionization could contribute to their observed line

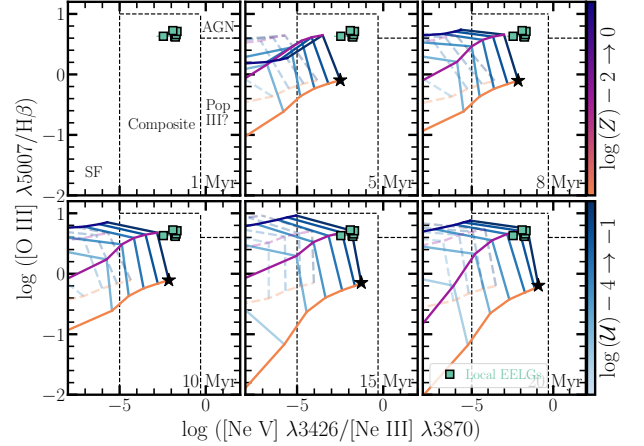


**Figure 11.** Same as Figure 7, but for a potential UV/optical diagnostic diagram for  $\text{SXP}_{\text{ULX}}$  contribution. For these high-ionization lines, the  $\text{SXP}_{\text{ULX}}$  contribution is substantial relative to the SSP-only case, but the high-ionization line intensities are generally weak except for select grid points (low metallicities and high  $\log \mathcal{U}$ ). The dashed lines illustrate classification regions for pure star-formation ionization, ionization from composite populations, ionization due to AGN, and potential ionization due to Pop III stars from Cleri et al. (2023). The cyan squares are the observed line ratios from a sample of local EELGs (Izotov et al. 2012; Berg et al. 2021; Olivier et al. 2022) that are consistent with select  $[\text{SXP}_{\text{ULX}} + \text{SSP}](t_{\text{burst}}, Z, \log \mathcal{U})$  models in a very narrow range of grid space.

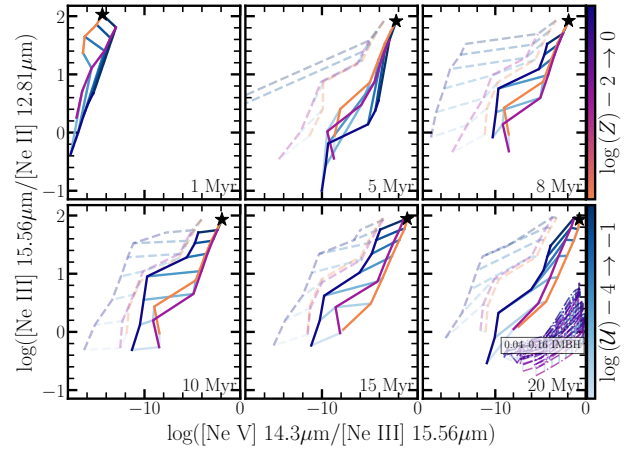


**Figure 12.** Same as Figure 11, but for a potential IR diagnostic, albeit using a weak coronal line that is highly sensitive to hardness of the ratio field. As in Figure 9, the IMBH models from Richardson et al. (2022) for a selection of IMBH fractional contributions are shown for reference.

intensities under this specific set of circumstances; how-

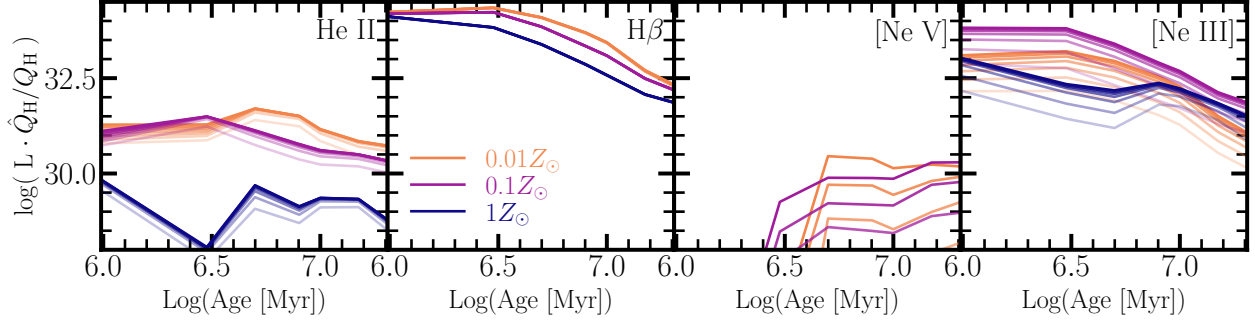


**Figure 13.** Nebular emission line luminosities normalized by stellar mass for He II  $\lambda 4686$ , H $\beta$ , [Ne V]  $\lambda 3426$ , and [Ne III]  $\lambda 3870$  as a function of burst age. As before, in each panel dark blue corresponds to  $Z_\odot$ , purple corresponds to  $0.1 Z_\odot$ , and orange corresponds to  $0.01 Z_\odot$  models. Increasing line opacity denotes increasing  $\log \mathcal{U}$ . The ratio of a high-ionization line (e.g., He II, [Ne V]) with significant SXP<sub>ULX</sub> contribution relative to a lower ionization line (e.g., H $\beta$ , [Ne III]) is largest at later times ( $> 10$  Myr), particularly for the lower metallicity models. This corresponds to the timescale on which the ionizing contribution from the stellar population has decreased significantly, while the SXP<sub>ULX</sub> ionizing contribution remains appreciable.

ever, such a range of physical properties (e.g., high  $\log \mathcal{U}$  coupled with older burst ages) may not be applicable in general to EELGs. For example, two of the galaxies in Figure 11 from have inferred ages  $\lesssim 10$  Myr, and may therefore require a source other than an SXP<sub>ULX</sub> or SSP to explain the observed line intensities, as discussed in Olivier et al. (2022).

In general, our models suggest select high-ionization emission lines can be produced by ionization due to an SXP<sub>ULX</sub> for  $t_{\text{burst}} > 10$  Myr and low metallicities. For SFHs that include a young ( $< 10$  Myr) burst component, the SXP<sub>ULX</sub> contribution to the ionizing photon budget is not significant enough to reproduce the observed line *ratios* that include high-ionization lines such as He II or [Ne V]. This is because, for the models considered here, the pure stellar ionizing continuum is substantial for  $t_{\text{burst}} < 10$  Myr, resulting in strong emission from lines such as H $\beta$ . This strong stellar ionizing flux effectively dilutes the SXP<sub>ULX</sub> contribution, which primarily affects the high-ionization line (e.g., He II) rather than hydrogen ionization. We illustrate this point in two ways. First, in Figure 13 we show nebular emission line luminosities normalized by stellar mass for He II  $\lambda 4686$ , H $\beta$ , [Ne V]  $\lambda 3426$ , and [Ne III]  $\lambda 3870$  as a function of burst age. In comparing the evolution of the intensities of He II and H $\beta$ , it is clear both lines reach their *absolute* maximum in intensity for  $t_{\text{burst}} \sim 3\text{--}5$  Myr; however, while the H $\beta$  intensity drops by almost two orders of magnitude thereafter, the evolution of the He II intensity is much flatter over the same time span, owing to the SXP<sub>ULX</sub> contribution, resulting in a higher ratio of He II  $\lambda$ /H $\beta$  at later times. The same is true for [Ne V]  $\lambda 3426$  relative to [Ne III]  $\lambda 3870$ . For this ratio, it is also particularly evident when the SXP<sub>ULX</sub> contribu-

tion turns for  $t_{\text{burst}} > 3$  Myr, as there is no appreciable [Ne V] emission prior to this.

To further illustrate the timescale dependent nature of the relative SXP<sub>ULX</sub> ionizing contribution, we reran the photoionization simulations without the strict delay-time dependence for the SXP<sub>ULX</sub> component. For these “no-delay time” simulations, we extrapolated  $L_X/M_0$  from Figure 1 to burst ages 1–3 Myr, allowing the SXP<sub>ULX</sub> to contribute to the ionizing budget at every time step. As Figure A.1 shows, the immediate formation of the SXP<sub>ULX</sub> alongside a 1 Myr or 3 Myr burst only weakly increases He II/H $\beta$ , given that the strength of the stellar ionizing continuum is still quite substantial on these timescales, as in Figure 13.

In this way, the addition of the SXP<sub>ULX</sub> may contribute significantly to high-energy ionizing photon production only in *some* environments, at least for the SED<sub>ULX</sub> considered in this work. Due to the time-dependent nature of the SXP<sub>ULX</sub> ionizing contribution from the models presented here, measured SFHs or other proxies for age (e.g., strong line equivalent widths) should be considered alongside emission line diagnostics when comparing with these models to discern SXP<sub>ULX</sub> ionizing contribution.

### 5.3. Consequences of Metallicity-Dependence of the SXP<sub>ULX</sub> and Adopted Abundance Patterns

The photoionization simulation results are based on the assumption that the metallicity of the SXP<sub>ULX</sub> corresponds to the stellar metallicity of the SSP, as would be expected if the SXP<sub>ULX</sub> and SSP form and evolve from the same parent stellar population. Consequently, a low-metallicity SSP, which already has a somewhat harder ionizing spectrum, will always be combined with an SXP<sub>ULX</sub> with higher formation efficiency ( $L_X/M_0$ )



than the  $\text{SXP}_{\text{ULX}}$  combined with a solar-metallicity SSP.

The imprint of the metallicity-dependent normalization of the  $\text{SXP}_{\text{ULX}}$  is particularly evident in emission line diagnostics that include metallicity-sensitive line ratios (e.g.,  $[\text{N II}]/\text{H}\alpha$ ). To illustrate the magnitude of this effect, we run simulations where we remove the correlation between the  $\text{SXP}_{\text{ULX}}$  normalization and stellar metallicity. In these “no stellar metallicity dependence” simulations, we allow an SSP at a given  $t_{\text{burst}}$  to be coupled with an  $\text{SXP}_{\text{ULX}}$  normalized using  $L_X/M_0$  from the orange curve (i.e., maximum) in Figure 1, regardless of the SSP metallicity. The results are shown in Figure A.2, where higher ratios of  $\text{He II } \lambda 4686/\text{H}\beta$  are produced at a given  $[\text{N II}]/\text{H}\alpha$ , particularly for the solar metallicity case. This results in much more overlap between the grid with the  $\text{SXP}_{\text{ULX}}$  contribution and the observed data points, for a broader range of burst ages; however, we note that such an elevated  $L_X/M_0$  for ULXs at solar metallicities is not supported by observations. Even allowing for variations due to stochastic sampling of the XLF, sources with  $L_X > 10^{39} \text{ erg s}^{-1}$  are more rare at higher metallicities, due to steepening of the bright end of the XLF with increasing metallicity (Lehmer et al. 2021). We therefore include this “no stellar metallicity dependence” example simply to illustrate the effects of our model choices.

While the  $\text{SXP}_{\text{ULX}}$  may not be an efficient additional source of ionizing photons at high metallicity given the relations in Figure 1, other sources of high-energy ionizing photons may operate preferentially in this regime. For example, as pointed out in Shirazi & Brinchmann (2012), the sub-sample of galaxies with WR features in Figure 8 generally has higher metallicity, which correlates with higher stellar mass and SFR, and therefore potentially stronger stellar feedback. For such galaxies, this stronger stellar feedback (i.e., winds and supernovae) may drive shocks, which could be an additional source of high-energy ionizing photons (e.g., Section 6.3.3).

The choice to couple stellar and gas-phase metallicities and the adopted abundance patterns for these simulations are also of critical importance for select emission line diagnostics. For example, though  $L_X/M_0$  increases with decreasing metallicity thereby increasing the number of high-energy ionizing photons, at very low metallicities the absolute abundance of some elements will be low enough that this becomes the dominant factor in setting the line intensity (e.g., discussion in Senchyna et al. 2020). This can easily be seen in the shape of the  $[\text{SXP}_{\text{ULX}} + \text{SSP}](t_{\text{burst}}, Z, \log \mathcal{U})$  grid in Figure 12, where the lowest metallicity models

including  $\text{SXP}_{\text{ULX}}$  contribution do not uniformly have the strongest  $[\text{Ne V}] 14.3\mu\text{m}/[\text{Ne III}] 15.56\mu\text{m}$  ratios, as would be expected if  $\text{SXP}_{\text{ULX}}$  production efficiency (i.e.,  $L_X/M_0$ ) were the dominant factor in determining line strength.

Likewise, the adopted C/O ratio in the simulations affects the extent of the grids as presented in Figures 7 and 10. Our abundance pattern corresponds to  $\log(\text{C/O}) = -0.45$ , which is a factor of approximately two higher than the average  $\log(\text{C/O})$  found for metal-poor, star-forming dwarf galaxies from Berg et al. (2019), though there is a large (0.17 dex) intrinsic dispersion in this value. For the emission line diagnostic in Figure 7, adopting a lower C/O ratio would shift the grids to the right (Jaskot & Ravindranath 2016), thereby encompassing all the observed BCDs. Likewise, a lower C/O ratio would shift the grids in Figure 10 up and to the left (Byler et al. 2018). We consider a more detailed treatment of the metallicity-dependence of the C/O and N/O ratios in the context of  $\text{SXP}_{\text{ULX}}$  ionization out of the scope of the present work, and refer the reader to Appendix B in Byler et al. (2018) for an excellent demonstration and discussion of the effect of differing abundance patterns on emission line diagnostics. We note that care should be taken in comparing observed line ratios to these simulations if using lines that are particularly sensitive to the assumed abundance pattern, such as C and N.

#### 5.4. Availability of Models

We make our models and simulation results available in two separate formats, as outlined below.

The models are available directly from `FSPS`<sup>9</sup>. From `FSPS`, one can build SEDs for a population with or without  $\text{SXP}_{\text{ULX}}$  contribution, including consideration of nebular line and continuum emission. In this way, users can simulate spectro-photometric data for populations including  $\text{SXP}_{\text{ULX}}$  contribution for use in SED fitting codes (e.g., Johnson et al. 2021; Doore et al. 2023).

We also provide the results through a standalone github repository<sup>10</sup>. In this repository we provide code examples in `python` for reading and plotting simulation results, allowing users to quickly plot the  $[\text{SXP}_{\text{ULX}} + \text{SSP}](t_{\text{burst}}, Z, \log \mathcal{U})$  grid for different emission line diagnostics. Users can therefore compare data or other model grids to these simulations including  $\text{SXP}_{\text{ULX}}$  contribution. In this repository, we likewise provide Table A.1 in a machine-readable format, such that lines

<sup>9</sup> <https://github.com/cconroy20/fps>; This version currently only supports adding  $\text{SXP}_{\text{ULX}}$  contribution alongside BPASS SSPs.

<sup>10</sup> <https://github.com/kgarofali/sxp-cloudy>

can be selected on the basis of relevant flags included in the table notes.

## 6. DISCUSSION

We have already presented potential UV, optical and IR emission line diagnostics for SXP<sub>ULX</sub> ionization in Section 5. Here we present best practices for diagnosing SXP<sub>ULX</sub> ionization when using X-ray observations, and summarize the results from this work relative to recent literature results for photoionization due to high-energy sources. We additionally present a brief discussion of alternative sources of hard ionizing photons and their connection to the SXP<sub>ULX</sub> model presented here.

### 6.1. Caveats For Applying SXP<sub>ULX</sub> Formalism to X-ray Observations

The emergent  $L_X$  (0.5–8 keV) from the SXP<sub>ULX</sub> models is very similar to the input  $L_X$  (i.e., Figure 1), as the hard photons are attenuated very little by the cloud. However, comparison of the simulation results with X-ray observations requires a more careful transformation of the intrinsic  $L_X$  from the simulations into a model for observed X-ray counts. We must consider of factors such as line of sight absorption (e.g., Wilms et al. 2000), viewing angle (e.g., Abolmasov et al. 2009; Kovelakas et al. 2022), source variability (e.g., Earnshaw et al. 2018), and instrumental effects. Such considerations likely require a full forward-modeling approach (e.g., Gilbertson et al. 2022), but could allow the use of relatively low count X-ray data in spectro-photometric fitting (e.g., Doore et al. 2023). Nevertheless, implementation will be non-trivial, and we defer full consideration to a future work. Here, we instead provide caveats relevant for interpreting the simulation results with respect to the observations, given factors affecting X-ray detectability.

A primary consideration in interpreting  $L_X$  values from the photoionization simulations is that the SED<sub>ULX</sub> model assumes a specific geometry appropriate to a supercritical accretion flow. In such a model, the wind or outflow component creates an effective funnel geometry, which collimates and scatters the harder inner disk emission for face-on viewers and may obscure this component for more edge-on viewing angles (e.g., Begelman et al. 2006; Poutanen et al. 2007; King et al. 2023). Under this geometry,  $L_X$  (obs) is likely dependent on inclination angle, and possibly also on the mass supply rate itself, which in the SED<sub>ULX</sub> model is set by the fixed funnel opening angle.

The effects of changing inclination angle and mass supply rate are illustrated in Figure 3. We show the adopted SED<sub>ULX</sub> in black with different linestyles, ranging from a face-on viewing angle ( $i = 0^\circ$ ) to the edge-on

case ( $i = 90^\circ$ ), wherein the SED<sub>ULX</sub> is primarily an EUV source. However, these are all for a fixed funnel opening angle ( $\theta$ ), tied to the mass transfer rate and BH mass. We therefore also show the effect of changing the funnel opening angle and corresponding mass supply rate in green for a small opening angle, and orange for a large funnel opening angle (both for  $i = 0^\circ$ , corresponding to a face-on viewing angle). These two extremes illustrate that the shape of the SED is also, not surprisingly, highly dependent on the assumed  $\theta$  (or, correspondingly,  $\dot{m}$ ): for a small funnel opening angle, where the mass transfer rate is very high, the peak of the SED shifts into the UV/optical owing to the dominance of the outflow component, while for a large funnel opening angle the peak shifts to the soft X-ray regime, and there is a loss of the very flat EUV component due to lack of relatively isotropic outflow component and associated self-irradiation within the wind funnel. Finally, we relax the assumption that the funnel opening angle is tied to the mass supply rate, allowing for a high mass transfer rate and modest funnel opening angle, shown by the blue line in Figure 3. This results in an intrinsic SED<sub>ULX</sub> with the strongest EUV component, as well as an appreciable optical/UV contribution, though it is unclear if such a case is physical.

The diversity of observed spectral shapes for ultra-luminous sources may therefore be explained by differences in both funnel opening angle and viewing angle. For example, ultra-luminous supersoft sources (e.g., Soria & Kong 2016; Urquhart & Soria 2016) may represent accreting compact objects with modest mass supply rates and large funnel opening angles viewed edge-on, while ultra-luminous UV sources may be compact objects with higher mass transfer rates likewise viewed edge-on (e.g., Kaaret et al. 2010).

Unfortunately, the dependence of mass transfer rate (or lack thereof) on funnel opening angle, and corresponding distribution of funnel opening angles is not well-known for either the intrinsic or the observed ULX population. Some binary population synthesis models suggest that the dominant accretor population (i.e., BH versus NS) and the timescale on which they appear will affect the fraction of the population that is strongly beamed (e.g., Wiktorowicz et al. 2019). In this respect, the form of the SED<sub>ULX</sub> used in this work is not exhaustive. As Figure 3 illustrates, it is possible an SXP could be an even more extreme EUV source under certain assumptions about the mass supply rate and distribution of funnel opening angles for the population. Different assumptions about typical values for ULX parameters such as  $\theta$  and  $\dot{m}$  will therefore propagate to the intensities of high-ionization nebular emission lines. In

practice, this could work to either increase or decrease the line intensities, or perhaps even alter the strict age-dependence for particular line ratios. A more detailed investigation of the effect of these parameters on the resultant nebular emission is therefore beyond the scope of the present work.

Despite these caveats, we demonstrate the applicability of our models to observations in terms of line intensities and  $\text{SXP}_{\text{ULX}} L_X$  via a comparison of simulated and observed  $\text{He II } \lambda 4686/\text{H}\beta$  as a function of  $L_X/\text{SFR}$  (a typical observable for HMXB and ULX populations; e.g., Mineo et al. 2012; Kovelakas et al. 2020). For the observational comparison set, we use a sample of star-forming dwarf galaxies for which there are spectra from SDSS, *HST*/COS, and MMT, and X-ray coverage from *Chandra* (Senchyna et al. 2020). Given the aforementioned caveats to X-ray detectability, comparison of our simulations with this observed sample rests on the assumption that the observed  $L_X$  corresponds roughly to the  $L_X$  from the intrinsic (simulated) population. Additionally, given the discussion in Section 5.2, we must consider whether the SFH assumed for the simulated results is appropriate to the observed sample (i.e., line intensities, SFRs, and  $L_X$  are time-averaged in a similar way). For the observed sample, line intensities are derived from the spectroscopic data, and the corresponding SFRs and values for  $L_X$  (or upper limits) are determined from the same spectroscopic aperture, or within  $1.4''$  of the aperture for the X-ray data. SFRs are measured using calibration constants derived from BPASS appropriate to the effective age and metallicity of the stellar population assuming continuous star formation.

To produce a simulated comparison set, we consider both burst and continuous SFH cases. The burst properties are easily recoverable from the simulations, as shown in figures throughout. To recover the continuous SFH case, we integrate the simulated line intensities and  $\text{SXP}_{\text{ULX}} L_X$  (both in terms of stellar mass) assuming a constant SFR of  $1 M_\odot \text{ yr}^{-1}$ . The results are shown in Figure 14, with the continuous SFH models as circles and the burst models as shaded regions, where the extent of the region encompasses the range of simulated  $\log \mathcal{U}$  and  $t_{\text{burst}}$ . The most extreme line ratios are achieved for high  $\log \mathcal{U}$  and older  $t_{\text{burst}}$ . The simulations can reproduce much of the observed range of  $\text{He II } \lambda/\text{H}\beta$  (green diamonds) for reasonable  $L_X/\text{SFR}$  (i.e., overlap with detections, or are below upper limits); however, this is true only for instantaneous bursts of star formation where  $t_{\text{burst}} > 10 \text{ Myr}$ . For the continuous SFH case, the models produce much more modest  $\text{He II } \lambda/\text{H}\beta$ , as discussed in Section 5.2, and there is much less overlap with the observed sample. This

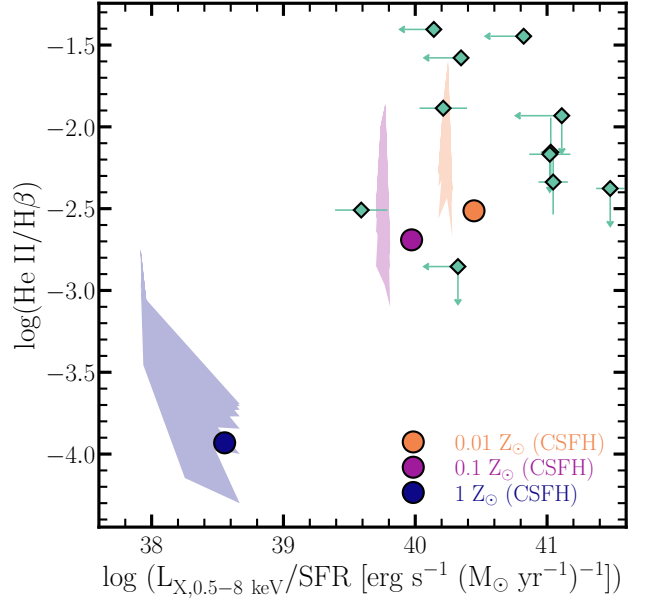


**Figure 14.** The emergent  $L_X$  (0.5–8 keV)/SFR relative to the strength of  $\text{He II } \lambda 4686/\text{H}\beta$  from photoionization simulations with  $\text{SXP}_{\text{ULX}}$  contribution for both continuous star formation (circles) and instantaneous bursts (shaded regions). As before, metallicities are color-coded and labeled. Observed values for a sample of star-forming dwarfs from Senchyna et al. (2020) are shown as green diamonds. The low metallicity simulations are consistent with all but the most extreme observed values and upper limits for the line ratios and  $L_X/\text{SFR}$ ; however, this requires instantaneous bursts where  $t_{\text{burst}} > 10 \text{ Myr}$ . Models with continuous SFHs produce  $L_X/\text{SFR}$  in the range of the observed galaxies and upper limits, but much lower ratios of  $\text{He II } \lambda 4686/\text{H}\beta$ .

demonstrates that the assumed SFH is of critical importance in such comparisons. SFHs recovered from SED fitting (e.g., Johnson et al. 2021), or other proxies for age such as  $\text{H}\alpha$  or  $\text{H}\beta$  equivalent width, are therefore integral to determining the importance of  $\text{SXP}_{\text{ULX}}$  high-energy ionizing contribution.

As some of the observed galaxies in Figure 14 have values of  $L_X/\text{SFR}$  in excess of the simulated results, we briefly comment on the effects of sampling in making such comparisons. In general, testing for agreement between the simulated results for  $L_X$  and an observed population is best achieved when the observed population has a well-sampled XLF. This typically holds in the high SFR regime ( $\gtrsim 3 M_\odot \text{ yr}^{-1}$ ), where the effects of stochastic sampling of the XLF are on the order of, or smaller than, the model uncertainties on  $L_X$ , and where the strict linear scaling of  $L_X$  with SFR holds (Grimm et al. 2003; Justham & Schawinski 2012; Lehmer et al. 2021). In the low SFR regime, on the other hand, integrated

$L_X$  (obs) can be subject to large ( $\sim 0.7$  dex) scatter due to stochastic sampling of an XLF that, for HMXBs and ULXs, flattens at the bright end (e.g., [Lehmer et al. 2021](#)). Similar but far less severe considerations about statistical sampling apply when determining and comparing SFRs. Empirical or model-derived calibration constants for different SFR indicators are based on the assumption of a fully populated IMF and SFR indicators which have equilibrated. In other words, typical calibration constants are appropriate for regions physically large enough for the IMF to be well-sampled *and* for which the SFH has been continuous long enough for a given SFR indicator to reach equilibrium (e.g., 5–100 Myr [Kennicutt 1998](#); [Kennicutt & Evans 2012](#)). The galaxies in Figure 14 that are X-ray detected with the highest  $L_X/\text{SFR}$  ( $\gtrsim 10^{41} \text{ erg s}^{-1}$ ) are some of the most distant galaxies ( $D > 200 \text{ Mpc}$ ) in the sample, such that the spectroscopic apertures encompass large areas on the sky, making it unlikely that statistical sampling affects the measured SFRs. These galaxies have measured SFRs in the range  $0.003\text{--}6 M_\odot \text{ yr}^{-1}$ , and therefore may be subject to significant sampling effects at the low SFR end; however, stochastic sampling is likely not enough to explain their high X-ray production efficiencies, even at the very low SFR end, making them  $\sim 2\sigma$  outliers relative to empirical scaling relations at low metallicities ([Lehmer et al. 2021](#)). These galaxies may therefore represent cases where alternative high-energy ionizing sources with  $L_X/\text{SFR}$  well in excess of average XRB scaling relations contribute to the observed line ratios (e.g., Section 6.3.2).

Taken together, the discussion presented here implies that in order to determine whether  $L_X$  from a given SXP<sub>ULX</sub> is consistent with observations requires modeling the effects of inclination, both on the *observable* spectral components and their *apparent* luminosities (e.g., [Kovlakas et al. 2022](#)), as well as consideration of the effects of sampling. The former is a critical consideration in the context of these simulations, as it implies an SXP<sub>ULX</sub> may be intrinsically very luminous, and therefore efficient at producing high-energy ionizing photons, while potentially being difficult to detect in X-rays. The latter is important because all line intensities (either for bursts or calculated for continuous SFH) are simulated assuming a population average  $L_X$ . For highly star-forming galaxies, the population average  $L_X$  may be a good approximation; however, if these conditions do not hold for an observed sample, comparison with simulation results may result in erroneous inferences about population age, metallicity, and/or source(s) of ionization.

## 6.2. Comparison with Recent Literature

There have been a number of works in the literature exploring the efficacy of X-ray sources in the production of high-energy ionizing photons, with a particular recent emphasis on the X-ray contribution to production of He II  $\lambda 4686$  in high-redshift galaxies and their analogs (e.g., [Garnett et al. 1991](#); [Schaerer et al. 2019](#); [Senchyna et al. 2020](#); [Simmonds et al. 2021](#); [Oskinova & Schaerer 2022](#); [Kovlakas et al. 2022](#); [Umeda et al. 2022](#); [Ramambason et al. 2022](#)). The most recent investigations fall broadly into two categories: (1) full photoionization simulations of the ionizing effect of an X-ray source coupled to a stellar population; and (2) analytic approximations for the X-ray source contribution to select line intensities, such as He II  $\lambda 4686$ . We focus on the former here for parity with our own implementation.

In Figure 15 we show the SED<sub>ULX</sub> for a 20 Myr instantaneous burst of star formation at  $0.1 Z_\odot$  in yellow. Here the SED<sub>ULX</sub> has been normalized to  $1 M_\odot$  stellar mass formed (Section 3), corresponding to  $L_X$  (0.5–8 keV)  $\sim 3 \times 10^{32} \text{ erg s}^{-1}$ . The corresponding SSP ( $t_{\text{burst}} = 20 \text{ Myr}$ ,  $0.1 Z_\odot$ ) is shown in green, while the composite of these two components is shown in black. The additional labeled SEDs (“MCD”, “DIS”, “BB”, and “I Zw18”) are selections from the literature that have previously been used in photoionization simulations. Below, we briefly summarize salient points from recent investigations using these SEDs, and compare to our findings based on the SXP<sub>ULX</sub> framework.

The photoionization simulations performed in [Senchyna et al. \(2020\)](#) explored the effect of HMXBs on production of He II  $\lambda 4686$  and [Ne V]  $\lambda 3426$ . The authors couple an HMXB model, represented via a multi-color disk SED (“MCD”, green dotted line in Figure 15) at different BH masses ( $\sim 10\text{--}100 M_\odot$ ) to BPASS stellar populations ( $Z = 0.001\text{--}0.020$ ) assuming continuous star formation. The HMXB component is scaled to the stellar population for a range of X-ray production efficiencies ( $L_X/\text{SFR} = 10^{40}\text{--}10^{44} \text{ erg s}^{-1} (M_\odot \text{ yr}^{-1})^{-1}$ ). Much like our approach, they used a modified version of `cloudyFSPS` to initialize the `CLOUDY` input grid, employing a similar range in  $\log \mathcal{U}$ . With these simulation inputs, the authors conclude that the observed range of He II  $\lambda 4686/\text{H}\beta$  can only be reproduced for extremely high X-ray production efficiencies ( $L_X$  (0.5–8 keV)/ $\text{SFR} > 10^{42} \text{ erg s}^{-1} (M_\odot \text{ yr}^{-1})^{-1}$ ). Such extreme X-ray production efficiencies are not observed, even in nearby extremely metal-poor galaxies, and are likely excluded by reionization-era constraints ([Lehmer et al. 2021](#); [HERA Collaboration et al. 2023](#)). In Figure 14 we compare our model line predictions with the observational sample from [Senchyna et al. \(2020\)](#) which they used, in part, to draw the conclusion that



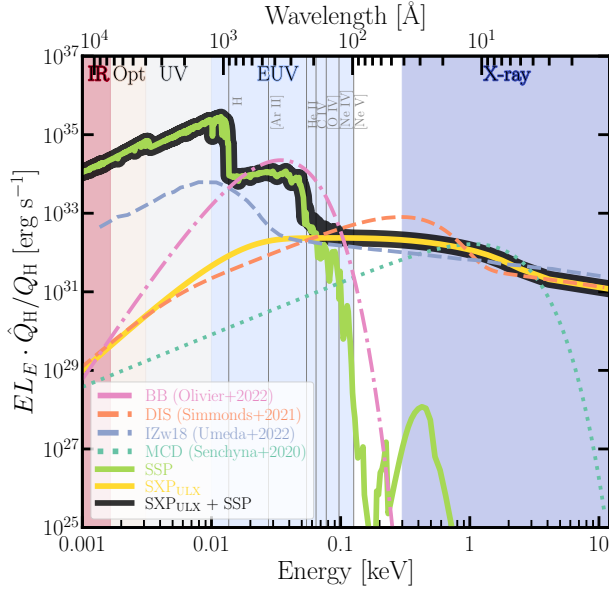


**Figure 15.** The intrinsic SED for the composite model (SXP<sub>ULX</sub> + SSP, solid black line) with  $t_{\text{burst}} = 20$  Myr and  $Z = 0.1 Z_{\odot}$ , normalized to  $1 M_{\odot}$  stellar mass formed. The stellar population and SED<sub>ULX</sub> components of the composite are shown in green and yellow, respectively. Various SEDs from the literature that have previously been used in photoionization simulations are shown in different colors and line styles for comparison, all normalized to the same  $L_X$  (0.5–8 keV) (or, in the case of the “BB”,  $L_{\text{EUV}}$ ) as the SED<sub>ULX</sub>. The grey vertical lines mark ionization potentials for select lines, as labeled.

HMXB ionization is insufficient to explain the observed range of He II  $\lambda 4686/H\beta$ . As already discussed in Section 6.1, our simulations are able to reproduce more of the observed range of He II  $\lambda 4686/H\beta$  within the observed range of  $L_X/\text{SFR}$ , but primarily for instantaneous bursts with  $t_{\text{burst}} > 10$  Myr at low metallicities. Under the assumption of a continuous SFH, as in Senchyna et al. (2020), our models are not able to reproduce the more extreme values of He II  $\lambda 4686/H\beta$  at the simulated range of  $L_X/\text{SFR}$ . This echoes the results presented in Senchyna et al. (2020), underscoring the importance of the assumed SFH in setting line ratios; however, even for similar assumptions about the SFH, our models produce stronger He II  $\lambda 4686/H\beta$  at a given  $L_X/\text{SFR}$  as compared with Senchyna et al. (2020), which we attribute to differences in the assumed SED for the X-ray photoionizing component. Our SED<sub>ULX</sub> is much flatter through the EUV than the multi-color disk model employed, and therefore produces more ionizing EUV photons per  $L_X$ .

The importance of the form of the SED to the production of high-energy ionizing photons was highlighted in the CLOUDY photoionization simulations from Simmonds

et al. (2021). These authors explored the photoionizing effect of ULXs using several empirical models for the ULX SED coupled to a BPASS SSP (1 Myr instantaneous burst with  $Z = 0.005$ <sup>11</sup>) again for a similar range in  $\log \mathcal{U}$  as employed here. In their simulations, the ULX contribution is scaled relative to the BPASS SSP for a range of  $L_X/\text{SFR}$ , motivated by empirical scalings and scatter therein. These authors find they can reproduce some of the observed range of He II  $\lambda 4686/H\beta$  for reasonable X-ray production efficiencies ( $L_X/\text{SFR} \simeq 10^{40} - 10^{41} \text{ erg s}^{-1} (M_{\odot} \text{ yr}^{-1})^{-1}$ ), roughly in agreement with our findings for instantaneous bursts and the SED<sub>ULX</sub> model.

In general, the simulations results presented in Simmonds et al. (2021) also achieve higher values of He II  $\lambda 4686/H\beta$  than our grids with SXP<sub>ULX</sub> contribution, at least for their most optimistic SED model (“DIS” from Berghea & Dudik 2012, as shown via the orange dashed line in Figure 15). We attribute differences in high-energy ionizing photon production efficiency between simulations, ostensibly both for ULX-type sources, in part to differences in adopted SED shape, and in part to treatment of how the ULX component is scaled relative to the stellar population as a function of metallicity and burst age. As is evident from Figure 15, the “DIS” model has a stronger soft X-ray excess than our SED<sub>ULX</sub>, leading to a different shape when extended into the EUV, particularly around 54 eV where He II  $\lambda 4686$  has its ionization potential. While our SXP<sub>ULX</sub> simulations are run coupled to a range of SSPs with  $L_X/M_0$  scaled as a function of burst age and metallicity, the simulations in Simmonds et al. (2021) are performed by scaling the ULX component to a single BPASS SSP (1 Myr,  $\sim 0.3 Z_{\odot}$ ) using a range of  $L_X/\text{SFR}$ . This amounts to relaxing the assumptions used here for scaling of the SXP<sub>ULX</sub> formation efficiency with SSP metallicity and age, and the requirement for a delay time for ULX formation. In this way, the approach in Simmonds et al. (2021) complements the average efficiencies employed in the SXP<sub>ULX</sub> simulations: using a broad range of  $L_X/\text{SFR}$  for a given  $Z$  and  $t_{\text{burst}}$  is akin to simulating a large degree of scatter in the X-ray production efficiency for that SSP.

While the simulations in Senchyna et al. (2020), Simmonds et al. (2021), and this work explore HMXBs and ULXs specifically, there are other recent approaches to the high-energy ionizing photon production question

<sup>11</sup> These authors list the metallicity of the BPASS SSP as  $12 + \log(\text{O}/\text{H}) = 8.1$ . For their adopted abundances from Grevesse et al. (2010), this corresponds to  $\sim 0.3 Z_{\odot}$ , which we assume corresponds to the BPASS  $Z = 0.005$  model.

that take a more agnostic approach to source type. In Umeda et al. (2022), the authors attempt to parametrically constrain the EUV shape of the intrinsic ionizing spectra for a sample of extremely metal-poor galaxies. To do so, they construct SEDs consisting of parametrized powerlaw and blackbody components which they run through CLOUDY. They then use MCMC to determine the parameters of these SED components that best describe a set of observed high-ionization emission lines from the sample of extremely metal-poor galaxies. Their best-performing models for each galaxy are then compared with more physical SEDs, in this case BPASS SSPs coupled to different ionizing sources such as ULX or AGN, to infer physical properties of the ionizing population. In Figure 15, we show the results of this approach for one of their galaxies, I Zw18 (blue dashed line), for which there exist excellent broad-band multi-wavelength coverage (i.e., X-ray, optical, and high-ionization nebular emission lines). We note that the results are remarkably consistent with our SED<sub>ULX</sub> component, despite very different approaches in (re)constructing the intrinsic ionizing spectrum.<sup>12</sup> In general, using their full galaxy sample, Umeda et al. (2022) show that the intensity of the observed high-ionization emission lines requires different combinations of BPASS SSPs (in terms of burst age) and ULX-like components with various scaling factors relative to the SSPs. Our [SXP<sub>ULX</sub> + SSP]( $t_{\text{burst}}$ ,  $Z$ ) grid is constructed with these various scaling factors determined from theoretical binary population synthesis models, while in Umeda et al. (2022) the characteristic burst ages and necessary scaling factors for the high-energy ionizing photon production are inferred from the best parametric fits after comparison with physical models. The two approaches are therefore quite complementary, and highlight that determining the sources that contribute to high-energy ionizing photon production may require consideration of not only different sources of ionizing photons, but also their relative contributions as a function of stellar population age and metallicity.

As a final point of comparison, we highlight the results from Olivier et al. (2022), where the authors fit the high-ionization emission lines in a set of nearby EELGs with very young ( $\lesssim 10$  Myr) and metal-poor ( $\sim 0.1 Z_{\odot}$ ) stellar populations. These authors find that BPASS SSPs alone cannot reproduce the observed strengths of some

of the highest ionization potential species, such as He II and [O IV]. To reproduce the strengths of such lines, they opt to add an 80,000 K blackbody to the BPASS SSPs scaled to a relatively large fractional contribution (45–55%) to the total luminosity. We show such a blackbody component in Figure 15 as the pink dash-dot line (“BB”). As already discussed in Section 6.1, the SED<sub>ULX</sub> includes a pseudo-blackbody component, albeit at slightly different temperature and normalization than the blackbody employed in Olivier et al. (2022). However, the temperature of the roughly blackbody component of the SED<sub>ULX</sub> and its relative contribution to the total composite SED depends on the specific assumptions about the accretion flow geometry, accretor type and mass, and mass supply rate, and our SED<sub>ULX</sub> model is certainly not exhaustive in these respects. Thus, an EUV blackbody source with no corresponding X-ray emission as employed in Olivier et al. (2022) is not necessarily incompatible with an SXP origin (e.g., Figure 3).

These results highlight a few crucial considerations for simulating photoionization due to an SXP-like source. Namely, the results depend heavily on the assumed SED shape for this additional ionizing component, and on how the component is scaled relative to the stellar population. Unfortunately, we still do not have tight empirical constraints on either of these ingredients for the case of ULXs specifically, or XRBs more broadly. However, as these photoionization simulation results suggest, select high-ionization emission lines may offer an additional lever arm for inferring the shape of unseen portions of the SED. The approaches presented in Umeda et al. (2022) and Olivier et al. (2022), for example, have the potential to be very powerful, but the recovered best-performing models depend critically on the suite of lines available for fitting as well as the set of parametric models considered. Whether using parametric or physically-motivated models as inputs to the photoionization simulations, larger grids are likely necessary going forward. We consider the recent approaches highlighted here important first steps in this process.

### 6.3. Alternative Ionizing Sources

For the SXP<sub>ULX</sub> model used in this work, we have assumed the accretor is a stellar mass BH ( $\sim 10$ – $100 M_{\odot}$ ) and have constructed the SED<sub>ULX</sub> accordingly. In this section, we discuss the effects of changing these assumptions about the accretor (both mass and type), and additional processes capable of producing high-energy ionizing photons.

#### 6.3.1. Neutron Star ULXs

While the simulations presented here consider only the case of stellar mass BH accretor for ULXs, there is now

<sup>12</sup> The ionizing spectra appear more discrepant in the UV-to-IR range, however, this regime was not the focus of the modeling in Umeda et al. (2022), and therefore had the smallest contribution (in terms of data sets used) to constraining the best-performing model.

direct and growing observational evidence for NS accretors in ULXs, via the detection of pulsations (e.g. [Bachetti et al. 2014](#); [Fürst et al. 2016](#); [Israel et al. 2017](#); [Carpano et al. 2018](#)). Swapping the BH for a NS accretor in the SXP<sub>ULX</sub> would result in a few fundamental differences, both in terms of longevity of the ionizing output relative to the stellar population and potentially the SED shape.

For the SSPs considered in this work ( $t_{\text{burst}} \leq 20$  Myr) BHs should dominate the accretor demographics, while NS likely become the main accretor population at later times (e.g., [Wiktorowicz et al. 2019](#)). The *addition* of NS ULXs to the SXP<sub>ULX</sub> would therefore further prolong the ionizing output of a population, beyond that of the most massive stars and binaries, and the BH SXP<sub>ULX</sub> presented here. Furthermore, because the stellar ionizing contribution begins to wane considerably on timescales  $> 20$  Myr after the massive star population is depleted, any additional source of high-energy photons present on these timescales will provide a larger fractional contribution to the overall ionizing photon budget. However, the contribution of different accretor demographics to the total  $L_X/M_0$  will be both SFH- and metallicity-dependent, and such a population breakdown for the scaling relations is not yet well-constrained theoretically or observationally.

In addition to timescale differences, the spectral shape and upper limit for the luminosity may well be different for NS accretors relative to stellar mass BHs in the supercritical regime. This is primarily due to the fact, in the case of a NS, the Eddington limit and accretion flow geometry may be modified by the presence of a strong magnetic field. In calculating the Eddington limit, the electron scattering cross section is typically given as the Thomson scattering cross section; however, in the presence of a strong magnetic field, this cross section may be reduced, effectively changing the radiation pressure term in Equation 1, and increasing the Eddington limit for a given mass ([Paczynski 1992](#)). Indeed, there is recent evidence for cyclotron resonance scattering features in the spectra of both a ULX and a hyper-luminous X-ray source ( $L_X > 10^{41}$  erg s<sup>-1</sup>), which implies the presence of an accreting NS with very strong magnetic field ([Brightman et al. 2018, 2022](#)). It is important to note, however, that an increase in Eddington limit due to a NS with a strong magnetic field is not mutually exclusive with a strongly super-Eddington mass supply rate (e.g., [Bachetti et al. 2022](#)), which may also lead to driving an outflow (e.g., [King & Lasota 2016](#); [King et al. 2017](#)).

A strong dipole field also funnels accreted material onto the poles of the NS (i.e., creates an accretion col-

umn) and possibly further modifies the picture of the supercritical accretion flow presented in Section 2.3.2, depending on how the extent of the Alfvén radius ( $R_M$ ) compares to the spherization radius ( $R_{\text{sph}}$ ). [King et al. \(2023\)](#) present a very detailed review and discussion of the current landscape of models for supercritically accreting NS, both pulsing and non-pulsing. Despite this attention to modeling, there exists no, to our knowledge, energetically self-consistent model in e.g., XSPEC for a NS ULX that allows for modeling the effects of a strong magnetic field as well as inclination-dependence on the resultant SED. We consider further investigation of the NS ULX contribution to the SXP<sub>ULX</sub> a promising avenue for future study, but outside the scope of the present work.

### 6.3.2. Intermediate Mass Black Holes

Moving up in the mass scale, IMBHs ( $100 M_\odot \leq m \leq 10^6 M_\odot$ ) have been proposed as an additional source of ionizing photons relative to stellar populations (e.g., [Hatano et al. 2023](#)). As relatively massive BHs with moderate to low mass transfer rates relative to Eddington, IMBHs may also have SEDs with a substantial EUV component. In Figure 16, we compare the SED<sub>ULX</sub> with IMBH SEDs for a  $10^3 M_\odot$  BH and  $10^5 M_\odot$  BH based on the *qsosed* model ([Kubota & Done 2018](#)), all normalized to the same  $L_X$  (0.5–8 keV) for plotting purposes. As Figure 16 shows, it can be difficult to distinguish between a ULX and IMBH for sources of similar bolometric luminosity that are sub-dominant with respect to the stellar population, particularly in the absence of broadband X-ray coverage. However, differences in the SED shapes in the EUV imply there is diagnostic power with high-ionization lines for discerning ionization by accreting BHs of different masses. We provide a preliminary exploration of this via a comparison with select results from the IMBH photoionization simulations presented in [Richardson et al. \(2022\)](#).

The full set of IMBH photoionization simulations from [Richardson et al. \(2022\)](#) is expansive, encompassing different BH masses, prescriptions for the IMBH SED, mixing methodologies between the IMBH and stellar population, and a relatively fine gridding in stellar metallicity and  $\log \mathcal{U}$ . We compare only with the subset of their results most closely matching our simulation inputs and set-up. Namely, we show only their simulations for a  $10^3 M_\odot$  IMBH (*qsosed* model) combined with a 20 Myr BPASS SSP assuming coincident mixing and a closed cloud geometry for grid points with  $-2 \leq \log(Z) \leq 0$  and  $-4 \leq \log \mathcal{U} \leq 1$ . In Figures 9 and 12 we plot their simulation results for IMBHs with fractional contribu-

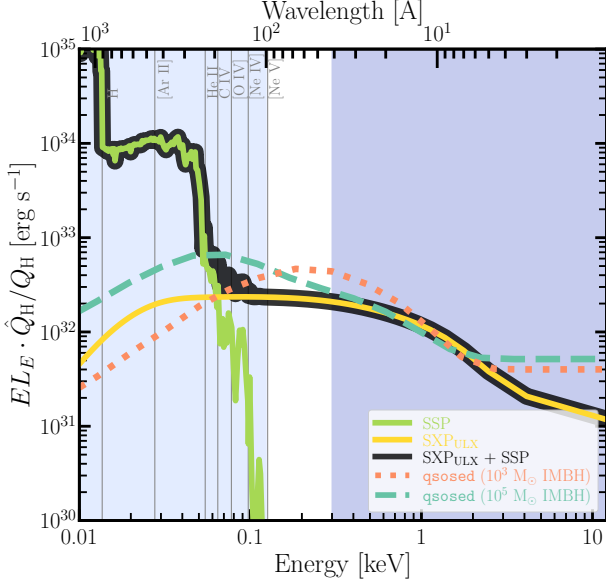


**Figure 16.** Similar to Figure 15, but for a comparison with  $10^3 M_\odot$  and  $10^5 M_\odot$  IMBH SEDs (orange dotted and green dashed lines, respectively), as employed in the photoionization simulations from Richardson et al. (2022). All SEDs are normalized to the same  $L_X$  (0.5–8 keV) for plotting purposes. In the absence of broad-band X-ray coverage, it can be difficult to distinguish between the SXP<sub>ULX</sub> and IMBH SEDs, particularly the sources are similar in bolometric luminosity and sub-dominant relative to the stellar population. However, differences in the intrinsic SEDs in the EUV-to-soft X-ray regime may result in some diagnostic power for distinguishing between these different ionizing sources using high-ionization nebular emission lines. Ionization potentials for a selection of lines are labeled and marked by grey vertical lines.

tions  $\leq 16\%$  relative to the 20 Myr SSP (bottom right panels).

The comparisons in Figures 9 and 12 illustrate that there is strong diagnostic potential with very high-ionization line species for distinguishing between the ionizing impact of BHs across orders of magnitude in mass (e.g., Cann et al. 2018; Richardson et al. 2022). Offsets between the IMBH grids and grid with SXP<sub>ULX</sub> contribution in these emission line diagnostics are driven primarily by SED shape, suggesting these particular line ratios are sensitive to BH mass. However, this implies the diagnostic power hinges on assumed SED shape for a given BH mass, as well as typical fractional contribution of the BH ionizing component relative to the stellar population.

To more clearly show the differences due to changing IMBH ionizing fraction, in Figure 17 we instead plot different fractional contributions of the IMBH (from 4–100%) relative to the SSP in each panel, as compared

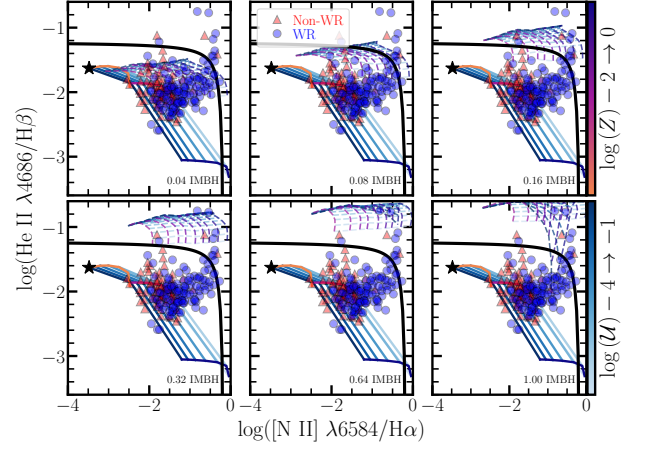


**Figure 17.** Similar to Figure 8, but with each panel showing only the 20 Myr [SXP<sub>ULX</sub> + SSP](\$t\_{burst}\$, Z, log  $\mathcal{U}$ ) grid (solid lines), relative to grids covering similar log  $\mathcal{U}$  and Z with different fractional IMBH contributions (dashed lines) from Richardson et al. (2022), where the IMBH contribution is annotated in the lower right of each panel. Emission line diagnostics including high-ionization species such as He II  $\lambda 4686$  can be useful for distinguishing between ionization due to SF versus accreting black holes across the mass scale (i.e., SXP<sub>ULX</sub>, IMBH, AGN); however, classification regions depend on the fractional contribution of the additional ionizing source (e.g., SXP<sub>ULX</sub> or IMBH) relative to the stellar population, and whether this contribution scales strongly as a function of metallicity and burst age.

only with the 20 Myr [SXP<sub>ULX</sub> + SSP](\$t\_{burst}\$, Z, log  $\mathcal{U}$) grid from this work. As before, the black solid line represents the empirically derived star formation/AGN demarcation, which the grid with SXP<sub>ULX</sub> contribution never exceeds, and the IMBH grids only exceed for ionizing contribution  $\geq 16\%$ . In addition to the fractional contribution relative to the stellar population, differences between the grids in this diagnostic space also depend critically on how the additional ionizing component is scaled with respect to the metallicity of the stellar population. For example, the IMBH simulations that we compare to do not include a metallicity-dependence for the scaling of the IMBH component relative to the SSP. In this way, the IMBH grids are produced in a fashion similar to our “no metallicity-dependence” model (e.g., Figure A.2), and can therefore achieve more extreme line ratios across a range in metallicities from solar to sub-solar. If instead the typical IMBH mass scales with stellar population metallicity, some regions of the IMBH grids as presented here would potentially be excluded. Harnessing the full power of such emission line diagnostics for investigating BH ionizing impact across the mass scale will therefore likely require careful consideration of$



typical host galaxy environments for ULXs and IMBHs, and how this affects their scaling and mixing with stellar populations (e.g., Polimera et al. 2022; Richardson et al. 2022).

### 6.3.3. Shock Ionization

While the grid with SXP<sub>ULX</sub> contribution presented here is capable of reproducing some of the range of observed line ratios for high-ionization emission lines, the models fail elsewhere. This implies the need either for tweaks to the SXP<sub>ULX</sub> implementation, or consideration of some alternative energetic process.

Here we explore the ionizing impact of fast radiative shocks, which have been considered by many others as a potential source of the requisite high-energy ionizing photons to explain the observed line intensities in select EELGs (e.g., Thuan & Izotov 2005; Izotov et al. 2012; Plat et al. 2019; Izotov et al. 2021). However, instead of suggesting fast shocks as an *alternative* source of ionizing photons relative to the SXP<sub>ULX</sub>, we consider them as an *additional* source related to the SXP<sub>ULX</sub> itself.

The accretion flow model prescribed for the SXP<sub>ULX</sub> in this work includes a quasi-spherical outflow component, which will likely interact with the surrounding medium. The interaction of ULX outflows with the interstellar medium is fairly well motivated by observations. A number of nearby ( $\lesssim 10$  Mpc) ULXs have been observed to sit inside large ( $> 100$  pc) bubbles. Such nebulae may be radiatively or mechanically inflated (e.g., Cseh et al. 2012; King et al. 2023). Several very bright ULXs show more direct evidence for the presence of fast outflows via the detection of blue-shifted absorption lines in high-resolution X-ray spectra (Poutanen et al. 2007; Pinto et al. 2016; Kosec et al. 2018a,b). Very recently, a detailed optical spectroscopic study of a ULX with direct evidence for fast outflows, as well as a bubble detection, confirmed the ULX wind or jet likely drives bubble expansion (Gúrpide et al. 2022). And indeed, investigation of the emission line diagnostics for such ULX bubbles reveal signatures of shock and photoionization (e.g., Abolmasov et al. 2007; López et al. 2019; Gúrpide et al. 2022). Therefore, in at least *some* cases, ULX feedback is sufficient to inflate a bubble and drive both shock and photoionization.

The SED<sub>ULX</sub> model employed here, by virtue of including the outflow component, is therefore capable of driving shock ionization as well as photoionization, though we model only the latter in this work. Detailed shock and precursor ionization model grids are available from MAPPINGS (Allen et al. 2008), which may in principle be matched to a corresponding SXP<sub>ULX</sub> to simulate the combined signature of shock and pho-

toionization. However, including the effects of shocks self-consistently alongside SXP<sub>ULX</sub> photoionization, assuming the shock is driven by the SXP<sub>ULX</sub> itself, will likely require more than the addition of separate grids. In all simulations presented here we assume the gas is uniformly distributed in the cloud, but the presence of shocks related to the SXP<sub>ULX</sub> (or indeed the stellar population) could preferentially displace gas from certain regions of the cloud. This may lead to shock ionization occurring in regions with different density than where the primary photoionization is occurring (e.g., Izotov et al. 2021). Such a non-uniform density may also alter the intensities of typical strong lines such as [O III], which is produced in the inner regions of the cloud. If gas is displaced from the central regions, this would amount to effectively lowering the ionization parameter for species such as [O III], relative to species produced elsewhere in the cloud (e.g., Kewley et al. 2013). It is clear a more careful treatment of joint consideration of SXP<sub>ULX</sub> shock and photoionization is warranted in terms of timescales, cloud properties, and mixing methodologies to understand the overall effects on typical line diagnostics. Given the modeling complexities, we defer consideration of joint SXP<sub>ULX</sub> shock and photoionization to a future related work.

As a final note, we remark that the presence of relatively ubiquitous ULX outflows implies the potential for feedback that can strongly shape the interstellar medium, akin to feedback from stellar winds and supernovae. For example, a  $10^7 M_{\odot}$  instantaneous burst of star formation yields  $\sim 10^{40}$  erg s $^{-1}$  mechanical luminosity over the course of 10 Myr as the most massive stars evolve and explode as supernovae (e.g., Leitherer et al. 1999; Prestwich et al. 2015). From Figure 1, a  $\lesssim 0.1 Z_{\odot}$  SXP<sub>ULX</sub> provides  $\sim 10^{39}$ – $10^{40}$  erg s $^{-1}$  mechanical luminosity for the same instantaneous burst, assuming ULX mechanical luminosity on par with radiative output. For at least some observed ULXs, it appears mechanical power from the outflow actually exceeds radiative power, suggesting the above estimate may even be a lower limit for SXP<sub>ULX</sub> feedback (e.g. Justham & Schawinski 2012; Pinto et al. 2016; Gúrpide et al. 2022). Feedback from an SXP<sub>ULX</sub> could therefore contribute to favorable conditions for ionizing photon escape (e.g., similar to the scenario for stellar populations from Jaskot & Oey 2013). Indeed, resolved studies of Lyman continuum leakers at X-ray wavelengths suggest ULXs could be an important source of mechanical feedback, facilitating the escape of ionizing photons by carving channels in the surrounding medium (Prestwich et al. 2015; Kaaret et al. 2017). An SXP<sub>ULX</sub> with strong outflow component could therefore be important for (1)

producing high-energy ionizing photons via both shock and photoionization; (2) facilitating ionizing photon escape; and (3) producing the soft ( $< 2$  keV) photons that can more efficiently heat the intergalactic medium prior to the epoch of reionization (e.g., Das et al. 2017; HERA Collaboration et al. 2023). As such, continued attention to modeling SXP<sub>ULX</sub>-like sources is extremely relevant to high redshift studies.

## 7. SUMMARY

In this work, we have presented a framework for combining a “simple X-ray population” alongside the corresponding simple stellar population in a physically consistent and meaningful manner in order to simulate and explore their combined ionizing impact as a function of (1) instantaneous burst age and (2) metallicity. Using our combined SED as input to the photoionization code CLOUDY, we have produced a nebular line and continuum emission grid, which we make publicly available. Our principal findings can be summarized as follows:

- The addition of the SXP<sub>ULX</sub> prolongs the ionizing output relative to single massive stars or the products of binary evolution already included in BPASS. This is a consequence of the physically robust combination of an SXP<sub>ULX</sub> to the corresponding BPASS SSP with relative scaling factors determined as a function of burst age and stellar metallicity. Namely, the SXP<sub>ULX</sub> is scaled with an increasing fractional contribution as a function of decreasing stellar metallicity, in line with empirical constraints, and combined only with an SSP of the corresponding age, following the expectation that the SXP<sub>ULX</sub> evolves from the parent stellar population.
- For the burst timescales modeled here ( $t_{\text{burst}} \leq 20$  Myr) the ionizing photons due to the SXP<sub>ULX</sub> contribute no more than  $\sim 5\%$  to the total nebular line and continuum emission. Broad-band FIR-to-UV colors are therefore not strongly affected by the addition of this component, relative to the case of a stellar-only ionizing component.
- Given that the SXP<sub>ULX</sub> has an SED which is very flat through the EUV, the addition of this component increases the intensity lines with ionization potentials  $\gtrsim 54$  eV such as He II  $\lambda 1640, 4686$  and [O IV]  $25.9\mu\text{m}$  by a factor of at least two relative to the BPASS SSPs alone. Emission line diagnostics including such lines can therefore be used to infer the presence of SXP<sub>ULX</sub> ionization.
- The intensity of very high-ionization lines (ionization potentials  $> 90$  eV) such as [Ne V]  $\lambda 3426$ ,

$14.3\mu\text{m}$  are strongly enhanced ( $> 10^5\times$ ) due to the addition of the SXP<sub>ULX</sub>; however, these lines are typically very weak in the simulations presented here (e.g.,  $\log(\hat{f}_{\text{line}}/\hat{f}_{\text{Pa}\beta}) \sim -9$  for coronal lines in the IR). This is due in large part to the fixed SXP<sub>ULX</sub> normalization relative to the SSP as a function of burst age and metallicity, where the maximum relative scaling is achieved for the lowest stellar metallicities. Because gas-phase and stellar metallicities are coupled in all simulations, the regime in which the SXP<sub>ULX</sub> reaches maximum ionizing contribution relative to the SSP is also the one where many elements have their lowest absolute abundances in the cloud, which can be the dominant factor in setting line intensity.

- SXP<sub>ULX</sub> photoionization is capable of reproducing the observed strengths of high-ionization emission line ratios (e.g., He II  $\lambda 4686/\text{H}\beta$ ), but primarily for instantaneous burst models with  $Z \lesssim 0.1 Z_{\odot}$  and  $t_{\text{burst}} > 10$  Myr. This is again a consequence of the coupling of the SXP<sub>ULX</sub> to the SSP as a fixed function of stellar metallicity and burst age. On timescales  $< 10$  Myr, the stellar ionizing continuum is still substantial, effectively diluting the SXP<sub>ULX</sub> ionizing output, particularly for high-ionization lines as measured relative to strong nebular lines for which there is little SXP<sub>ULX</sub> ionizing contribution. In this way, the assumed star formation history strongly affects the efficacy of the SXP<sub>ULX</sub> to high-energy ionizing photon production in terms of typical observed line ratios.
- Comparison of the simulation outputs to observations in terms of emission line ratios and/or typical X-ray observables (e.g.,  $L_X/\text{SFR}$ ) should be performed with careful consideration of the underlying assumptions, including SXP<sub>ULX</sub> SED shape, cloud abundance patterns, assumed star formation history, and SXP<sub>ULX</sub> detectability as a function of viewing angle and variability.
- Though the X-ray detectability of the SXP<sub>ULX</sub> depends on viewing angle and duty cycle, the SXP<sub>ULX</sub> production of high-ionization nebular emission lines is ubiquitous for the SED<sub>ULX</sub> modeled here. This is due to the fact that the EUV and soft X-ray photons from the SXP<sub>ULX</sub> emanate from the outflow component, which is assumed to be relatively isotropic. In this way, high-ionization emission lines can be indirect tracers of a transient or unfavorably oriented SXP<sub>ULX</sub>.

- The outflow component of the SXP<sub>ULX</sub> may additionally drive fast shocks and therefore shock ionization. We discuss complexities in joint modeling of shock and photoionization due to an SXP<sub>ULX</sub>, and consider it a promising avenue for future study. This is particularly true given that SXP<sub>ULX</sub> mechanical feedback due to a disk wind or outflow could be similar in magnitude, if not timescale, to feedback from stellar winds and supernovae. As such, the SXP<sub>ULX</sub> could contribute to conditions in the interstellar medium conducive to ionizing photon escape, and additionally provide a substantial number of soft (0.5–2 keV) photons that could directly contribute to heating the intergalactic medium prior to the epoch of reionization.

*Software:* CLOUDY (Ferland et al. 2017), cloudyFSPS (Byler 2018), FSPS (Conroy et al. 2009; Conroy & Gunn 2010), python-fsps (Johnson et al. 2022), XSPEC (Arnaud 1996), HEASoft (Nasa High Energy Astrophysics Science Archive Research Center (Heasarc) 2014), astropy (Astropy Collaboration et al. 2013, 2018, 2022), scipy (Virtanen et al. 2020), matplotlib (Hunter 2007), astroquery (Ginsburg et al. 2019), numpy (Harris et al. 2020)

1 K.G.’s research was supported by an appointment  
2 to the NASA Postdoctoral Program at NASA God-  
3 dard Space Flight Center, administered by Oak  
4 Ridge Associated Universities under contract with  
5 NASA. We gratefully acknowledge support under NASA  
6 award 80GSFC21M0002 (A.R.B., P.T.), NASA award  
7 80NSSC22K0407 (K.G., A.R.B., P.T., A.H.), and *Chan-*  
8 *dra* grant No. GO0-2JO76A (B.D.L., A.R.B.) C.R. ac-  
9 knowledges the support of the Elon University Japheth  
10 E. Rawls Professorship. K.G. would like to thank Jenna  
11 Cann and Anna Ogorzałek for helpful conversations dur-  
12 ing the preparation of this manuscript, and give a special  
13 thanks to Nell Byler for inspiration.

## REFERENCES

- Abolmasov, P., Karpov, S., & Kotani, T. 2009, PASJ, 61, 213, doi: [10.1093/pasj/61.2.213](https://doi.org/10.1093/pasj/61.2.213)
- Abolmasov, P. K., Swartz, D. A., Fabrika, S., et al. 2007, ApJ, 668, 124, doi: [10.1086/520828](https://doi.org/10.1086/520828)
- Allen, M. G., Groves, B. A., Dopita, M. A., Sutherland, R. S., & Kewley, L. J. 2008, ApJS, 178, 20, doi: [10.1086/589652](https://doi.org/10.1086/589652)
- Anders, E., & Grevesse, N. 1989, GeoCoA, 53, 197, doi: [10.1016/0016-7037\(89\)90286-X](https://doi.org/10.1016/0016-7037(89)90286-X)
- Arnaud, K. A. 1996, in Astronomical Society of the Pacific Conference Series, Vol. 101, Astronomical Data Analysis Software and Systems V, ed. G. H. Jacoby & J. Barnes, 17
- Astropy Collaboration, Robitaille, T. P., Tollerud, E. J., et al. 2013, A&A, 558, A33, doi: [10.1051/0004-6361/201322068](https://doi.org/10.1051/0004-6361/201322068)
- Astropy Collaboration, Price-Whelan, A. M., Sipőcz, B. M., et al. 2018, AJ, 156, 123, doi: [10.3847/1538-3881/aabc4f](https://doi.org/10.3847/1538-3881/aabc4f)
- Astropy Collaboration, Price-Whelan, A. M., Lim, P. L., et al. 2022, ApJ, 935, 167, doi: [10.3847/1538-4357/ac7c74](https://doi.org/10.3847/1538-4357/ac7c74)
- Bachetti, M., Harrison, F. A., Walton, D. J., et al. 2014, Nature, 514, 202, doi: [10.1038/nature13791](https://doi.org/10.1038/nature13791)
- Bachetti, M., Heida, M., Maccarone, T., et al. 2022, ApJ, 937, 125, doi: [10.3847/1538-4357/ac8d67](https://doi.org/10.3847/1538-4357/ac8d67)
- Basu-Zych, A. R., Lehmer, B., Fragos, T., et al. 2016, ApJ, 818, 140, doi: [10.3847/0004-637X/818/2/140](https://doi.org/10.3847/0004-637X/818/2/140)
- Basu-Zych, A. R., Lehmer, B. D., Hornschemeier, A. E., et al. 2013, ApJ, 774, 152, doi: [10.1088/0004-637X/774/2/152](https://doi.org/10.1088/0004-637X/774/2/152)
- Begelman, M. C., King, A. R., & Pringle, J. E. 2006, MNRAS, 370, 399, doi: [10.1111/j.1365-2966.2006.10469.x](https://doi.org/10.1111/j.1365-2966.2006.10469.x)
- Belczynski, K., Bulik, T., Fryer, C. L., et al. 2010, ApJ, 714, 1217, doi: [10.1088/0004-637X/714/2/1217](https://doi.org/10.1088/0004-637X/714/2/1217)
- Belczynski, K., & Taam, R. E. 2008, ApJ, 685, 400, doi: [10.1086/590551](https://doi.org/10.1086/590551)
- Berg, D. A., Chisholm, J., Erb, D. K., et al. 2019, ApJL, 878, L3, doi: [10.3847/2041-8213/ab21dc](https://doi.org/10.3847/2041-8213/ab21dc)

- . 2021, *ApJ*, 922, 170, doi: [10.3847/1538-4357/ac141b](https://doi.org/10.3847/1538-4357/ac141b)
- Berg, D. A., Erb, D. K., Auger, M. W., Pettini, M., & Brammer, G. B. 2018, *ApJ*, 859, 164, doi: [10.3847/1538-4357/aab7fa](https://doi.org/10.3847/1538-4357/aab7fa)
- Berghea, C. T., & Dudik, R. P. 2012, *ApJ*, 751, 104, doi: [10.1088/0004-637X/751/2/104](https://doi.org/10.1088/0004-637X/751/2/104)
- Berghea, C. T., Dudik, R. P., Weaver, K. A., & Kallman, T. R. 2010, *ApJ*, 708, 364, doi: [10.1088/0004-637X/708/1/364](https://doi.org/10.1088/0004-637X/708/1/364)
- Brightman, M., Kosec, P., Fürst, F., et al. 2022, *ApJ*, 929, 138, doi: [10.3847/1538-4357/ac5e37](https://doi.org/10.3847/1538-4357/ac5e37)
- Brightman, M., Harrison, F. A., Fürst, F., et al. 2018, *Nature Astronomy*, 2, 312, doi: [10.1038/s41550-018-0391-6](https://doi.org/10.1038/s41550-018-0391-6)
- Brinchmann, J., Kunth, D., & Durret, F. 2008, *A&A*, 485, 657, doi: [10.1051/0004-6361/200809783](https://doi.org/10.1051/0004-6361/200809783)
- Brorby, M., & Kaaret, P. 2017, *MNRAS*, 470, 606, doi: [10.1093/mnras/stx1286](https://doi.org/10.1093/mnras/stx1286)
- Byler, N. 2018, *cloudyFSPS*, 1.0.0, Zenodo, doi: [10.5281/zenodo.1156412](https://doi.org/10.5281/zenodo.1156412)
- Byler, N., Dalcanton, J. J., Conroy, C., & Johnson, B. D. 2017, *ApJ*, 840, 44, doi: [10.3847/1538-4357/aa6c66](https://doi.org/10.3847/1538-4357/aa6c66)
- Byler, N., Dalcanton, J. J., Conroy, C., et al. 2018, *ApJ*, 863, 14, doi: [10.3847/1538-4357/aacd50](https://doi.org/10.3847/1538-4357/aacd50)
- Cann, J. M., Satyapal, S., Abel, N. P., et al. 2018, *ApJ*, 861, 142, doi: [10.3847/1538-4357/aac64a](https://doi.org/10.3847/1538-4357/aac64a)
- Carpano, S., Haberl, F., Maitra, C., & Vasilopoulos, G. 2018, *MNRAS*, 476, L45, doi: [10.1093/mnrasl/sly030](https://doi.org/10.1093/mnrasl/sly030)
- Cleri, N. J., Olivier, G. M., Hutchison, T. A., et al. 2023, *arXiv e-prints*, arXiv:2301.07745, doi: [10.48550/arXiv.2301.07745](https://doi.org/10.48550/arXiv.2301.07745)
- Colbert, E. J. M., & Mushotzky, R. F. 1999, *ApJ*, 519, 89, doi: [10.1086/307356](https://doi.org/10.1086/307356)
- Conroy, C. 2013, *ARA&A*, 51, 393, doi: [10.1146/annurev-astro-082812-141017](https://doi.org/10.1146/annurev-astro-082812-141017)
- Conroy, C., & Gunn, J. E. 2010, *ApJ*, 712, 833, doi: [10.1088/0004-637X/712/2/833](https://doi.org/10.1088/0004-637X/712/2/833)
- Conroy, C., Gunn, J. E., & White, M. 2009, *ApJ*, 699, 486, doi: [10.1088/0004-637X/699/1/486](https://doi.org/10.1088/0004-637X/699/1/486)
- Copperwheat, C., Cropper, M., Soria, R., & Wu, K. 2005, *MNRAS*, 362, 79, doi: [10.1111/j.1365-2966.2005.09223.x](https://doi.org/10.1111/j.1365-2966.2005.09223.x)
- Cseh, D., Corbel, S., Kaaret, P., et al. 2012, *ApJ*, 749, 17, doi: [10.1088/0004-637X/749/1/17](https://doi.org/10.1088/0004-637X/749/1/17)
- Das, A., Mesinger, A., Pallottini, A., Ferrara, A., & Wise, J. H. 2017, *MNRAS*, 469, 1166, doi: [10.1093/mnras/stx943](https://doi.org/10.1093/mnras/stx943)
- Doore, K., Monson, E. B., Eufrasio, R. T., et al. 2023, *arXiv e-prints*, arXiv:2304.06753, doi: [10.48550/arXiv.2304.06753](https://doi.org/10.48550/arXiv.2304.06753)
- Dopita, M. A., Kewley, L. J., Heisler, C. A., & Sutherland, R. S. 2000, *ApJ*, 542, 224, doi: [10.1086/309538](https://doi.org/10.1086/309538)
- Earnshaw, H. P., Roberts, T. P., & Sathyaprakash, R. 2018, *MNRAS*, 476, 4272, doi: [10.1093/mnras/sty501](https://doi.org/10.1093/mnras/sty501)
- Eldridge, J. J., & Stanway, E. R. 2016, *MNRAS*, 462, 3302, doi: [10.1093/mnras/stw1772](https://doi.org/10.1093/mnras/stw1772)
- Eldridge, J. J., Stanway, E. R., Xiao, L., et al. 2017, *PASA*, 34, e058, doi: [10.1017/pasa.2017.51](https://doi.org/10.1017/pasa.2017.51)
- Ferland, G. J., Chatzikos, M., Guzmán, F., et al. 2017, *RMxAA*, 53, 385. <https://arxiv.org/abs/1705.10877>
- Fragos, T., Lehmer, B. D., Naoz, S., Zezas, A., & Basu-Zych, A. 2013a, *ApJL*, 776, L31, doi: [10.1088/2041-8205/776/2/L31](https://doi.org/10.1088/2041-8205/776/2/L31)
- Fragos, T., Kalogera, V., Belczynski, K., et al. 2008, *ApJ*, 683, 346, doi: [10.1086/588456](https://doi.org/10.1086/588456)
- Fragos, T., Kalogera, V., Willems, B., et al. 2009, *ApJL*, 702, L143, doi: [10.1088/0004-637X/702/2/L143](https://doi.org/10.1088/0004-637X/702/2/L143)
- Fragos, T., Lehmer, B., Tremmel, M., et al. 2013b, *ApJ*, 764, 41, doi: [10.1088/0004-637X/764/1/41](https://doi.org/10.1088/0004-637X/764/1/41)
- Fryer, C. L., Belczynski, K., Wiktorowicz, G., et al. 2012, *ApJ*, 749, 91, doi: [10.1088/0004-637X/749/1/91](https://doi.org/10.1088/0004-637X/749/1/91)
- Fürst, F., Walton, D. J., Harrison, F. A., et al. 2016, *ApJL*, 831, L14, doi: [10.3847/2041-8205/831/2/L14](https://doi.org/10.3847/2041-8205/831/2/L14)
- Garnett, D. R., Kennicutt, Robert C., J., Chu, Y.-H., & Skillman, E. D. 1991, *ApJ*, 373, 458, doi: [10.1086/170065](https://doi.org/10.1086/170065)
- Garofali, K., Williams, B. F., Hillis, T., et al. 2018, *MNRAS*, 479, 3526, doi: [10.1093/mnras/sty1612](https://doi.org/10.1093/mnras/sty1612)
- Garofali, K., Lehmer, B. D., Basu-Zych, A., et al. 2020, *ApJ*, 903, 79, doi: [10.3847/1538-4357/abba2d](https://doi.org/10.3847/1538-4357/abba2d)
- Gierliński, M., Done, C., & Page, K. 2009, *MNRAS*, 392, 1106, doi: [10.1111/j.1365-2966.2008.14166.x](https://doi.org/10.1111/j.1365-2966.2008.14166.x)
- Gilbertson, W., Lehmer, B. D., Doore, K., et al. 2022, *ApJ*, 926, 28, doi: [10.3847/1538-4357/ac4049](https://doi.org/10.3847/1538-4357/ac4049)
- Ginsburg, A., Sipőcz, B. M., Brasseur, C. E., et al. 2019, *AJ*, 157, 98, doi: [10.3847/1538-3881/aafc33](https://doi.org/10.3847/1538-3881/aafc33)
- Gladstone, J. C., Copperwheat, C., Heinke, C. O., et al. 2013, *ApJS*, 206, 14, doi: [10.1088/0067-0049/206/2/14](https://doi.org/10.1088/0067-0049/206/2/14)
- Gladstone, J. C., Roberts, T. P., & Done, C. 2009a, *MNRAS*, 397, 1836, doi: [10.1111/j.1365-2966.2009.15123.x](https://doi.org/10.1111/j.1365-2966.2009.15123.x)
- . 2009b, *MNRAS*, 397, 1836, doi: [10.1111/j.1365-2966.2009.15123.x](https://doi.org/10.1111/j.1365-2966.2009.15123.x)
- Götberg, Y., de Mink, S. E., Groh, J. H., Leitherer, C., & Norman, C. 2019, *A&A*, 629, A134, doi: [10.1051/0004-6361/201834525](https://doi.org/10.1051/0004-6361/201834525)
- Grevesse, N., Asplund, M., Sauval, A. J., & Scott, P. 2010, *Ap&SS*, 328, 179, doi: [10.1007/s10509-010-0288-z](https://doi.org/10.1007/s10509-010-0288-z)
- Grimm, H. J., Gilfanov, M., & Sunyaev, R. 2003, *MNRAS*, 339, 793, doi: [10.1046/j.1365-8711.2003.06224.x](https://doi.org/10.1046/j.1365-8711.2003.06224.x)



- Grisé, F., Kaaret, P., Corbel, S., et al. 2012a, *ApJ*, 745, 123, doi: [10.1088/0004-637X/745/2/123](https://doi.org/10.1088/0004-637X/745/2/123)
- . 2012b, *ApJ*, 745, 123, doi: [10.1088/0004-637X/745/2/123](https://doi.org/10.1088/0004-637X/745/2/123)
- Gúrpide, A., Parra, M., Godet, O., Contini, T., & Olive, J. F. 2022, *A&A*, 666, A100, doi: [10.1051/0004-6361/202142229](https://doi.org/10.1051/0004-6361/202142229)
- Harris, C. R., Millman, K. J., van der Walt, S. J., et al. 2020, *Nature*, 585, 357, doi: [10.1038/s41586-020-2649-2](https://doi.org/10.1038/s41586-020-2649-2)
- Hatano, S., Ouchi, M., Umeda, H., et al. 2023, arXiv e-prints, arXiv:2305.02189, doi: [10.48550/arXiv.2305.02189](https://doi.org/10.48550/arXiv.2305.02189)
- Heida, M., Harrison, F. A., Brightman, M., et al. 2019a, *ApJ*, 871, 231, doi: [10.3847/1538-4357/aafa77](https://doi.org/10.3847/1538-4357/aafa77)
- Heida, M., Jonker, P. G., Torres, M. A. P., et al. 2016, *MNRAS*, 459, 771, doi: [10.1093/mnras/stw695](https://doi.org/10.1093/mnras/stw695)
- . 2014, *MNRAS*, 442, 1054, doi: [10.1093/mnras/stu928](https://doi.org/10.1093/mnras/stu928)
- Heida, M., Lau, R. M., Davies, B., et al. 2019b, *ApJL*, 883, L34, doi: [10.3847/2041-8213/ab4139](https://doi.org/10.3847/2041-8213/ab4139)
- HERA Collaboration, Abdurashidova, Z., Adams, T., et al. 2023, *ApJ*, 945, 124, doi: [10.3847/1538-4357/acf50](https://doi.org/10.3847/1538-4357/acf50)
- Hunter, J. D. 2007, *Computing in Science & Engineering*, 9, 90, doi: [10.1109/MCSE.2007.55](https://doi.org/10.1109/MCSE.2007.55)
- Israel, G. L., Belfiore, A., Stella, L., et al. 2017, *Science*, 355, 817, doi: [10.1126/science.aai8635](https://doi.org/10.1126/science.aai8635)
- Izotov, Y. I., Thuan, T. X., & Guseva, N. G. 2021, *MNRAS*, 508, 2556, doi: [10.1093/mnras/stab2798](https://doi.org/10.1093/mnras/stab2798)
- Izotov, Y. I., Thuan, T. X., & Privon, G. 2012, *MNRAS*, 427, 1229, doi: [10.1111/j.1365-2966.2012.22051.x](https://doi.org/10.1111/j.1365-2966.2012.22051.x)
- Jaskot, A. E., & Oey, M. S. 2013, *ApJ*, 766, 91, doi: [10.1088/0004-637X/766/2/91](https://doi.org/10.1088/0004-637X/766/2/91)
- Jaskot, A. E., & Ravindranath, S. 2016, *ApJ*, 833, 136, doi: [10.3847/1538-4357/833/2/136](https://doi.org/10.3847/1538-4357/833/2/136)
- Johnson, B., Foreman-Mackey, D., Sick, J., et al. 2022, *dfm/python-fsps: python-fsps v0.4.2rc1, v0.4.2rc1*, Zenodo, doi: [10.5281/zenodo.7113363](https://doi.org/10.5281/zenodo.7113363)
- Johnson, B. D., Leja, J., Conroy, C., & Speagle, J. S. 2021, *ApJS*, 254, 22, doi: [10.3847/1538-4365/abef67](https://doi.org/10.3847/1538-4365/abef67)
- Justham, S., & Schawinski, K. 2012, *MNRAS*, 423, 1641, doi: [10.1111/j.1365-2966.2012.20985.x](https://doi.org/10.1111/j.1365-2966.2012.20985.x)
- Kaaret, P., Brorby, M., Casella, L., & Prestwich, A. H. 2017, *MNRAS*, 471, 4234, doi: [10.1093/mnras/stx1945](https://doi.org/10.1093/mnras/stx1945)
- Kaaret, P., & Corbel, S. 2009, *ApJ*, 697, 950, doi: [10.1088/0004-637X/697/1/950](https://doi.org/10.1088/0004-637X/697/1/950)
- Kaaret, P., Feng, H., Wong, D. S., & Tao, L. 2010, *ApJL*, 714, L167, doi: [10.1088/2041-8205/714/1/L167](https://doi.org/10.1088/2041-8205/714/1/L167)
- Kennicutt, Robert C., J. 1998, *ARA&A*, 36, 189, doi: [10.1146/annurev.astro.36.1.189](https://doi.org/10.1146/annurev.astro.36.1.189)
- Kennicutt, R. C., & Evans, N. J. 2012, *ARA&A*, 50, 531, doi: [10.1146/annurev-astro-081811-125610](https://doi.org/10.1146/annurev-astro-081811-125610)
- Kewley, L. J., Dopita, M. A., Leitherer, C., et al. 2013, *ApJ*, 774, 100, doi: [10.1088/0004-637X/774/2/100](https://doi.org/10.1088/0004-637X/774/2/100)
- King, A., & Lasota, J.-P. 2016, *MNRAS*, 458, L10, doi: [10.1093/mnras/slw011](https://doi.org/10.1093/mnras/slw011)
- King, A., Lasota, J.-P., & Kluźniak, W. 2017, *MNRAS*, 468, L59, doi: [10.1093/mnras/slx020](https://doi.org/10.1093/mnras/slx020)
- King, A., Lasota, J.-P., & Middleton, M. 2023, *NewAR*, 96, 101672, doi: [10.1016/j.newar.2022.101672](https://doi.org/10.1016/j.newar.2022.101672)
- King, A. R. 2009, *MNRAS*, 393, L41, doi: [10.1111/j.1745-3933.2008.00594.x](https://doi.org/10.1111/j.1745-3933.2008.00594.x)
- King, A. R., Davies, M. B., Ward, M. J., Fabbiano, G., & Elvis, M. 2001, *ApJL*, 552, L109, doi: [10.1086/320343](https://doi.org/10.1086/320343)
- Kosec, P., Pinto, C., Fabian, A. C., & Walton, D. J. 2018a, *MNRAS*, 473, 5680, doi: [10.1093/mnras/stx2695](https://doi.org/10.1093/mnras/stx2695)
- Kosec, P., Pinto, C., Walton, D. J., et al. 2018b, *MNRAS*, 479, 3978, doi: [10.1093/mnras/sty1626](https://doi.org/10.1093/mnras/sty1626)
- Kosec, P., Pinto, C., Reynolds, C. S., et al. 2021, *MNRAS*, 508, 3569, doi: [10.1093/mnras/stab2856](https://doi.org/10.1093/mnras/stab2856)
- Kovlakas, K., Fragos, T., Schaerer, D., & Mesinger, A. 2022, arXiv e-prints, arXiv:2207.09331, <https://arxiv.org/abs/2207.09331>
- Kovlakas, K., Zezas, A., Andrews, J. J., et al. 2020, *MNRAS*, 498, 4790, doi: [10.1093/mnras/staa2481](https://doi.org/10.1093/mnras/staa2481)
- Kramida, A., Yu. Ralchenko, Reader, J., & and NIST ASD Team. 2022, NIST Atomic Spectra Database (ver. 5.10), [Online]. Available: <https://physics.nist.gov/asd> [2023, April 21]. National Institute of Standards and Technology, Gaithersburg, MD.
- Kubota, A., & Done, C. 2018, *MNRAS*, 480, 1247, doi: [10.1093/mnras/sty1890](https://doi.org/10.1093/mnras/sty1890)
- Lau, R. M., Heida, M., Walton, D. J., et al. 2019, *ApJ*, 878, 71, doi: [10.3847/1538-4357/ab1b1c](https://doi.org/10.3847/1538-4357/ab1b1c)
- Lebouteiller, V., Péquignot, D., Cormier, D., et al. 2017, *A&A*, 602, A45, doi: [10.1051/0004-6361/201629675](https://doi.org/10.1051/0004-6361/201629675)
- Lehmer, B. D., Basu-Zych, A. R., Mineo, S., et al. 2016, *ApJ*, 825, 7, doi: [10.3847/0004-637X/825/1/7](https://doi.org/10.3847/0004-637X/825/1/7)
- Lehmer, B. D., Eufrasio, R. T., Markwardt, L., et al. 2017, *ApJ*, 851, 11, doi: [10.3847/1538-4357/aa9578](https://doi.org/10.3847/1538-4357/aa9578)
- Lehmer, B. D., Eufrasio, R. T., Tzanavaris, P., et al. 2019, arXiv e-prints, <https://arxiv.org/abs/1905.05197>
- Lehmer, B. D., Eufrasio, R. T., Basu-Zych, A., et al. 2021, *ApJ*, 907, 17, doi: [10.3847/1538-4357/abcec1](https://doi.org/10.3847/1538-4357/abcec1)
- Leitherer, C., Schaerer, D., Goldader, J. D., et al. 1999, *ApJS*, 123, 3, doi: [10.1086/313233](https://doi.org/10.1086/313233)
- Linden, T., Kalogera, V., Sepinsky, J. F., et al. 2010, *ApJ*, 725, 1984, doi: [10.1088/0004-637X/725/2/1984](https://doi.org/10.1088/0004-637X/725/2/1984)
- Lipunova, G. V. 1999, *Astronomy Letters*, 25, 508, <https://arxiv.org/abs/astro-ph/9906324>
- Liu, J.-F., Bregman, J. N., & Seitzer, P. 2004, *ApJ*, 602, 249, doi: [10.1086/380994](https://doi.org/10.1086/380994)

- López, K. M., Jonker, P. G., Heida, M., et al. 2019, MNRAS, 489, 1249, doi: [10.1093/mnras/stz2127](https://doi.org/10.1093/mnras/stz2127)
- Madau, P., & Dickinson, M. 2014, ARA&A, 52, 415, doi: [10.1146/annurev-astro-081811-125615](https://doi.org/10.1146/annurev-astro-081811-125615)
- Mapelli, M., Ripamonti, E., Zampieri, L., Colpi, M., & Bressan, A. 2010, MNRAS, 408, 234, doi: [10.1111/j.1365-2966.2010.17048.x](https://doi.org/10.1111/j.1365-2966.2010.17048.x)
- Middleton, M. J., Heil, L., Pintore, F., Walton, D. J., & Roberts, T. P. 2015, MNRAS, 447, 3243, doi: [10.1093/mnras/stu2644](https://doi.org/10.1093/mnras/stu2644)
- Middleton, M. J., & King, A. 2017, MNRAS, 470, L69, doi: [10.1093/mnrasl/slx079](https://doi.org/10.1093/mnrasl/slx079)
- Mineo, S., Gilfanov, M., & Sunyaev, R. 2012, MNRAS, 419, 2095, doi: [10.1111/j.1365-2966.2011.19862.x](https://doi.org/10.1111/j.1365-2966.2011.19862.x)
- Motch, C., Pakull, M. W., Grisé, F., & Soria, R. 2011, Astronomische Nachrichten, 332, 367, doi: [10.1002/asna.201011501](https://doi.org/10.1002/asna.201011501)
- Nasa High Energy Astrophysics Science Archive Research Center (Heasarc). 2014, HEASoft: Unified Release of FTOOLS and XANADU, Astrophysics Source Code Library, record ascl:1408.004. <http://ascl.net/1408.004>
- Olivier, G. M., Berg, D. A., Chisholm, J., et al. 2022, ApJ, 938, 16, doi: [10.3847/1538-4357/ac8f2c](https://doi.org/10.3847/1538-4357/ac8f2c)
- Oskinova, L. M., & Schaerer, D. 2022, A&A, 661, A67, doi: [10.1051/0004-6361/202142520](https://doi.org/10.1051/0004-6361/202142520)
- Paczynski, B. 1992, A&A, 42, 145
- Pinto, C., Middleton, M. J., & Fabian, A. C. 2016, Nature, 533, 64, doi: [10.1038/nature17417](https://doi.org/10.1038/nature17417)
- Plat, A., Charlot, S., Bruzual, G., et al. 2019, MNRAS, 490, 978, doi: [10.1093/mnras/stz2616](https://doi.org/10.1093/mnras/stz2616)
- Polimera, M. S., Kannappan, S. J., Richardson, C. T., et al. 2022, ApJ, 931, 44, doi: [10.3847/1538-4357/ac6595](https://doi.org/10.3847/1538-4357/ac6595)
- Poutanen, J., Lipunova, G., Fabrika, S., Butkevich, A. G., & Abolmasov, P. 2007, MNRAS, 377, 1187, doi: [10.1111/j.1365-2966.2007.11668.x](https://doi.org/10.1111/j.1365-2966.2007.11668.x)
- Prestwich, A. H., Jackson, F., Kaaret, P., et al. 2015, ApJ, 812, 166, doi: [10.1088/0004-637X/812/2/166](https://doi.org/10.1088/0004-637X/812/2/166)
- Ramambason, L., Leboutteiller, V., Bik, A., et al. 2022, A&A, 667, A35, doi: [10.1051/0004-6361/202243866](https://doi.org/10.1051/0004-6361/202243866)
- Richardson, C. T., Simpson, C., Polimera, M. S., et al. 2022, ApJ, 927, 165, doi: [10.3847/1538-4357/ac510c](https://doi.org/10.3847/1538-4357/ac510c)
- Schaerer, D., Fragos, T., & Izotov, Y. I. 2019, A&A, 622, L10, doi: [10.1051/0004-6361/201935005](https://doi.org/10.1051/0004-6361/201935005)
- Senchyna, P., Stark, D. P., Charlot, S., et al. 2021, MNRAS, 503, 6112, doi: [10.1093/mnras/stab884](https://doi.org/10.1093/mnras/stab884)
- Senchyna, P., Stark, D. P., Chevallard, J., et al. 2019, MNRAS, 488, 3492, doi: [10.1093/mnras/stz1907](https://doi.org/10.1093/mnras/stz1907)
- Senchyna, P., Stark, D. P., Mirocha, J., et al. 2020, MNRAS, 494, 941, doi: [10.1093/mnras/staa586](https://doi.org/10.1093/mnras/staa586)
- Senchyna, P., Stark, D. P., Vidal-García, A., et al. 2017, MNRAS, 472, 2608, doi: [10.1093/mnras/stx2059](https://doi.org/10.1093/mnras/stx2059)
- Shakura, N. I., & Sunyaev, R. A. 1973, A&A, 24, 337
- Shirazi, M., & Brinchmann, J. 2012, MNRAS, 421, 1043, doi: [10.1111/j.1365-2966.2012.20439.x](https://doi.org/10.1111/j.1365-2966.2012.20439.x)
- Simmonds, C., Schaerer, D., & Verhamme, A. 2021, A&A, 656, A127, doi: [10.1051/0004-6361/202141856](https://doi.org/10.1051/0004-6361/202141856)
- Soria, R., & Kong, A. 2016, MNRAS, 456, 1837, doi: [10.1093/mnras/stv2671](https://doi.org/10.1093/mnras/stv2671)
- Soria, R., Kuntz, K. D., Winkler, P. F., et al. 2012, ApJ, 750, 152, doi: [10.1088/0004-637X/750/2/152](https://doi.org/10.1088/0004-637X/750/2/152)
- Stanway, E. R., & Eldridge, J. J. 2019, A&A, 621, A105, doi: [10.1051/0004-6361/201834359](https://doi.org/10.1051/0004-6361/201834359)
- Stark, D. P. 2016, ARA&A, 54, 761, doi: [10.1146/annurev-astro-081915-023417](https://doi.org/10.1146/annurev-astro-081915-023417)
- Sutton, A. D., Roberts, T. P., & Middleton, M. J. 2013, MNRAS, 435, 1758, doi: [10.1093/mnras/stt1419](https://doi.org/10.1093/mnras/stt1419)
- Tao, L., Feng, H., Grisé, F., & Kaaret, P. 2011, ApJ, 737, 81, doi: [10.1088/0004-637X/737/2/81](https://doi.org/10.1088/0004-637X/737/2/81)
- Telford, O. G., Chisholm, J., McQuinn, K. B. W., & Berg, D. A. 2021, ApJ, 922, 191, doi: [10.3847/1538-4357/ac1ce2](https://doi.org/10.3847/1538-4357/ac1ce2)
- Thuan, T. X., & Izotov, Y. I. 2005, ApJS, 161, 240, doi: [10.1086/491657](https://doi.org/10.1086/491657)
- Umeda, H., Ouchi, M., Nakajima, K., et al. 2022, ApJ, 930, 37, doi: [10.3847/1538-4357/ac602d](https://doi.org/10.3847/1538-4357/ac602d)
- Urquhart, R., & Soria, R. 2016, MNRAS, 456, 1859, doi: [10.1093/mnras/stv2293](https://doi.org/10.1093/mnras/stv2293)
- Vink, J. S., de Koter, A., & Lamers, H. J. G. L. M. 2001, A&A, 369, 574, doi: [10.1051/0004-6361:20010127](https://doi.org/10.1051/0004-6361:20010127)
- Vinokurov, A., Fabrika, S., & Atapin, K. 2013, Astrophysical Bulletin, 68, 139, doi: [10.1134/S1990341313020028](https://doi.org/10.1134/S1990341313020028)
- Virtanen, P., Gommers, R., Oliphant, T. E., et al. 2020, Nature Methods, 17, 261, doi: [10.1038/s41592-019-0686-2](https://doi.org/10.1038/s41592-019-0686-2)
- Walton, D. J., Fuerst, F., Harrison, F., et al. 2013, ApJ, 779, 148, doi: [10.1088/0004-637X/779/2/148](https://doi.org/10.1088/0004-637X/779/2/148)
- Walton, D. J., Harrison, F. A., Grefenstette, B. W., et al. 2014, ApJ, 793, 21, doi: [10.1088/0004-637X/793/1/21](https://doi.org/10.1088/0004-637X/793/1/21)
- Walton, D. J., Bachetti, M., Fürst, F., et al. 2018, ApJL, 857, L3, doi: [10.3847/2041-8213/aabadc](https://doi.org/10.3847/2041-8213/aabadc)
- Weaver, K. A., Meléndez, M., Mushotzky, R. F., et al. 2010, ApJ, 716, 1151, doi: [10.1088/0004-637X/716/2/1151](https://doi.org/10.1088/0004-637X/716/2/1151)
- Wiktorowicz, G., Lasota, J.-P., Belczynski, K., et al. 2021, ApJ, 918, 60, doi: [10.3847/1538-4357/ac0cf7](https://doi.org/10.3847/1538-4357/ac0cf7)
- Wiktorowicz, G., Lasota, J.-P., Middleton, M., & Belczynski, K. 2019, ApJ, 875, 53, doi: [10.3847/1538-4357/ab0f27](https://doi.org/10.3847/1538-4357/ab0f27)
- Wiktorowicz, G., Sobolewska, M., Lasota, J.-P., & Belczynski, K. 2017, ApJ, 846, 17, doi: [10.3847/1538-4357/aa821d](https://doi.org/10.3847/1538-4357/aa821d)

Wilms, J., Allen, A., & McCray, R. 2000, ApJ, 542, 914,  
doi: [10.1086/317016](https://doi.org/10.1086/317016)

Yao, Y., & Feng, H. 2019, ApJL, 884, L3,  
doi: [10.3847/2041-8213/ab44c7](https://doi.org/10.3847/2041-8213/ab44c7)

## APPENDIX

**Table A.1.** Line list used in photoionization simulations, including vacuum wavelength, line identifier, and CLOUDY specific identifier.

Vacuum Wavelength ( $\text{\AA}$ )	Line ID	Cloudy ID
(1)	(2)	(3)
917.473	O I 917.473	O 1 917.473A
917.726	O I 917.726	O 1 917.726A
917.970	O I 917.97	O 1 917.970A
918.147	P III 918.147	P 3 918.147A
918.493	Ar I 918.493	Ar 1 918.493A
918.704	O I 918.704	O 1 918.704A
919.912	O I 919.912	O 1 919.912A
920.243	O I 920.243	O 1 920.243A
920.963	H I 920.963	H 1 920.963A
922.509	Ar I 922.509	Ar 1 922.509A
922.969	O I 922.969	O 1 922.969A
923.150	H I (Ly-8) 923.15	H 1 923.150A
923.438	O I 923.438	O 1 923.438A
924.009	Cr III 924.009	Cr 3 924.009A
926.226	H I (Ly-7) 926.226	H 1 926.226A
927.472	O I 927.472	O 1 927.472A
928.186	O I 928.186	O 1 928.186A
929.014	Al II 929.014	Al 2 929.014A
930.748	H I (Ly-6) 930.748	H 1 930.748A
934.501	O I 934.501	O 1 934.501A
935.672	O I 935.672	O 1 935.672A
937.804	H I (Ly-5) 937.804	H 1 937.804A
942.258	N I 942.258	N 1 942.258A
943.939	C I 943.939	C 1 943.939A
946.100	C II 946.1	C 2 946.100A
946.387	O I 946.387	O 1 946.387A
948.506	O I 948.506	O 1 948.506A
949.743	H I (Ly- $\delta$ ) 949.743	H 1 949.743A
950.661	P IV 950.661	P 4 950.661A
952.118	N I 952.118	N 1 952.118A
953.970	N I 953.97	N 1 953.970A
954.104	N I 954.104	N 1 954.104A
959.306	Mg II 959.306	Mg 2 959.306A

**Table A.1** *continued*



**Table A.1** (*continued*)

Vacuum Wavelength (Å)	Line ID	Cloudy ID
(1)	(2)	(3)
963.828	P II 963.828	P 2 963.828A
967.202	P II 967.202	P 2 967.202A
969.049	O I 969.049	O 1 969.049A
972.537	H I (Ly- $\gamma$ ) 972.537	H 1 972.537A
973.577	O I 973.577	O 1 973.577A
976.791	O I 976.791	O 1 976.791A
977.000	C III 977	C 3 977.000A
980.700	N I 980.7	N 1 980.700A
981.258	Cl IV 981.258	Cl 4 981.258A
991.000	N III 991	N 3 991.000A
993.354	Si II 993.354	Si 2 993.354A
1001.73	P III 1001.73	P 3 1001.73A
1007.34	S III 1007.34	S 3 1007.34A
1011.29	Cl III 1011.29	Cl 3 1011.29A
1020.18	C II 1020.18	C 2 1020.18A
1024.03	Si II 1024.03	Si 2 1024.03A
1025.72	H I (Ly- $\beta$ ) 1025.72	H 1 1025.72A
1033.06	Cr III 1033.06	Cr 3 1033.06A
1035.74	Cr III 1035.74	Cr 3 1035.74A
1036.80	C II 1036.8	C 2 1036.80A
1040.08	Mg II 1040.08	Mg 2 1040.08A
1071.32	Cl II 1071.32	Cl 2 1071.32A
1084.94 <sup>†</sup>	He II 1084.94	He 2 1084.94A
1085.00	N II 1085.	Blnd 1085.00A
1086.27	S IV 1086.27	S 4 1086.27A
1092.50	C II 1092.5	C 2 1092.50A
1095.69	Ar I 1095.69	Ar 1 1095.69A
1121.30 <sup>  </sup>	P 5 1121.3	P 5 1121.30A
1131.12	N I 1131.12	N 1 1131.12A
1140.10	C I 1140.1	C 1 1140.10A
1154.42	P II 1154.42	P 2 1154.42A
1175.99	C III 1175.99	C 3 1175.99A
1179.59	Si II 1179.59	Si 2 1179.59A
1194.45	S III 1194.45	S 3 1194.45A
1198.85	Mn II 1198.85	Mn 2 1198.85A
1200.00	N I 1200	N 1 1200.00A
1206.50	Si III 1206.5	Si 3 1206.50A
1215.13 <sup>*</sup>	He II 1215.13	He 2 1215.13A
1215.67	H I (Ly- $\alpha$ ) 1215.67	H 1 1215.67A
1247.50	C I 1247.5	C 1 1247.50A

**Table A.1** *continued*

**Table A.1** (*continued*)

Vacuum Wavelength (Å)	Line ID	Cloudy ID
(1)	(2)	(3)
1256.00	S II 1256	Blnd 1256.00A
1257.64	Mg II 1257.64	Mg 2 1257.64A
1264.74	Si II 1264.74	Si 2 1264.74A
1309.28	Si II 1309.28	Si 2 1309.28A
1307.68	P II 1307.68	P 2 1307.68A
1314.77	C I 1314.77	C 1 1314.77A
1324.11	Ni II 1324.11	Ni 2 1324.11A
1335.00	C II 1335	C 2 1335.00A
1341.17	P III 1341.17	P 3 1341.17A
1357.00	O I 1357	O 1 1357.00A
1375.73	Ni II 1375.73	Ni 2 1375.73A
1393.75	Si IV 1393.75	Si 4 1393.75A
1400.37	Ni II 1400.37	Ni 2 1400.37A
1402.77	Si IV 1402.77	Si 4 1402.77A
1406.02	S IV 1406.02	S 4 1406.02A
1416.89	S IV 1416.89	S 4 1416.89A
1472.74	Ni II 1472.74	Ni 2 1472.74A
1484.97	Ni II 1484.97	Ni 2 1484.97A
1486.50 <sup>†</sup>	N IV] 1486.5	N 4 1486.50A
1533.43	Si II 1533.43	Si 2 1533.43A
1548.19 <sup>†</sup>	C IV 1548.19	C 4 1548.19A
1550.78 <sup>†</sup>	C IV 1550.78	C 4 1550.78A
1561.33	C I 1561.33	C 1 1561.33A
1577.10	C III 1577.1	C 3 1577.10A
1640.43 <sup>*</sup>	He II 1640.43	He 2 1640.43A
1656.27	C I 1656.27	C 1 1656.27A
1660.81 <sup>†</sup>	O III] 1660.81	O 3 1660.81A
1666.00 <sup>†</sup>	O III] 1666	Blnd 1666.00A
1670.79	Al II 1670.79	Al 2 1670.79A
1720.00	S III 1720	Blnd 1720.00A
1742.00	N II 1742	N 2 1742.00A
1744.24	Ni II 1744.24	Ni 2 1744.24A
1748.65	N III] 1748.65	N 3 1748.65A
1751.22	N III] 1751.22	N 3 1751.22A
1751.83	Ni II 1751.83	Ni 2 1751.83A
1752.16	N III] 1752.16	N 3 1752.16A
1754.00	N III] 1754	N 3 1754.00A
1814.56 <sup>†</sup>	[Ne III] 1814.56	Ne 3 1814.56A
1816.93	Si II 1816.93	Si 2 1816.93A
1828.00	C III 1828	C 3 1828.00A

**Table A.1** *continued*

**Table A.1** (*continued*)

Vacuum Wavelength (Å)	Line ID	Cloudy ID
(1)	(2)	(3)
1854.72	[Al III] 1854.72	Al 3 1854.72A
1862.79	[Al III] 1862.79	Al 3 1862.79A
1882.71	Si III] 1882.71	Si 3 1882.71A
1892.03	Si III] 1892.03	Si 3 1892.03A
1906.68	[C III] 1906.68	C 3 1906.68A
1908.73	C III] 1908.73	C 3 1908.73A
2060.47	Cr II 2060.47	Cr 2 2059.78A
2141.71	N II] 2141.71	Blnd 2141.00A
2297.64	C III] 2297.64	C 3 2296.90A
2321.70 <sup>†</sup>	[O III] 2321.7	O 3 2320.95A
2324.25	C II] 2324.25	C 2 2323.50A
2325.44	C II] 2325.44	C 2 2324.69A
2327.68	C II] 2327.68	C 2 2326.93A
2328.87	C II] 2328.87	C 2 2328.12A
2335.35	Si II] 2335.35	Si 2 2334.60A
2344.95	Si II] 2344.95	Si 2 2344.20A
2400.01	Fe II 2400.01	Fe 2 2399.24A
2424.77 <sup>‡</sup>	[Ne IV] 2424.77	Blnd 2424.00A
2471.79	[O II] 2471.79	Blnd 2471.00A
2589.79	Mn II 2589.79	Mn 2 2588.97A
2661.18	[Al II] 2661.18	Al 2 2660.35A
2669.99	[Al II] 2669.99	Al 2 2669.15A
2796.40	Mg II] 2796.4	Mg 2 2795.53A
2803.58	Mg II] 2803.58	Mg 2 2802.71A
2829.96	He I 2829.96	He 1 2829.08A
2853.01	Mg I 2853.01	Mg 1 2852.13A
2854.54 <sup>†</sup>	Ar IV 2854.54	Ar 4 2853.66A
2946.01	He I 2946.01	He 1 2945.10A
3110.13	[Ar III] 3110.13	Ar 3 3109.18A
3188.71	He I 3188.71	He 1 3187.74A
3343.19 <sup>‡</sup>	[Ne III] 3343.19	Ne 3 3342.18A
3427.07 <sup>‡</sup>	[Ne V] 3427.07	Ne 5 3426.03A
3448.63	He I 3448.63	He 1 3447.59A
3614.73	He I 3614.73	He 1 3613.64A
3722.75	[S III] 3722.75	S 3 3721.63A
3727.12	[O II] 3727.12	Blnd 3726.00A
3730.12	[O II] 3730.12	Blnd 3729.00A
3799.03	H I (Ba-8) 3799.03	H 1 3797.89A
3820.75	He I 3820.75	He 1 3819.61A
3836.53	H I (Ba-7) 3836.53	H 1 3835.38A

**Table A.1** *continued*

**Table A.1** (*continued*)

Vacuum Wavelength (Å)	Line ID	Cloudy ID
(1)	(2)	(3)
3868.16	[O II] 3868.16	O 2 3867.00A
3868.64	He I 3868.64	He 1 3867.48A
3869.92 <sup>†</sup>	[Ne III] 3869.92	Ne 3 3868.76A
3889.79	He I 3889.79	He 1 3888.63A
3890.21	H I (Ba-6) 3890.21	H 1 3889.05A
3965.91	He I 3965.91	He 1 3964.73A
3968.65 <sup>†</sup>	[Ne III] 3968.65	Ne 3 3967.47A
3971.26	H I (Ba-5) 3971.26	H 1 3970.07A
4027.40	He I 4027.4	He 1 4026.20A
4042.20	[N II] 4042.2	N 2 4041.00A
4052.21	[O II] 4052.21	O 2 4051.00A
4069.81	[S II] 4069.81	S 2 4068.60A
4070.21	[C III] 4070.21	C 3 4069.00A
4075.21	[S II] 4075.21	Blnd 4074.00A
4076.21	[O II] 4076.21	O 2 4075.00A
4077.56	[S II] 4077.56	S 2 4076.35A
4095.22	[O II] 4095.22	O 2 4094.00A
4102.95	H I (Ba-δ) 4102.95	H 1 4101.73A
4112.22	[O II] 4112.22	O 2 4111.00A
4122.05	He I 4122.05	He 1 4120.82A
4144.99	He I 4144.99	He 1 4143.76A
4153.24	[O II] 4153.24	O 2 4152.00A
4170.21	He I 4170.21	He 1 4168.97A
4189.25	[O II] 4189.25	O 2 4188.00A
4240.26	[N II] 4240.26	N 2 4239.00A
4268.27	C II 4268.27	C 2 4267.00A
4279.27	[O II] 4279.27	O 2 4278.00A
4295.27	[O II] 4295.27	O 2 4294.00A
4307.17	[Fe II] 4307.17	Fe 2 4305.89A
4341.75	H I (Ba-γ) 4341.75	H 1 4340.46A
4343.29	[O II] 4343.29	O 2 4342.00A
4364.29	[O III] 4364.29	Blnd 4363.00A
4380.30	[N III] 4380.3	N 3 4379.00A
4389.23	He I 4389.23	He 1 4387.93A
4438.86	He I 4438.86	He 1 4437.55A
4472.81	He I 4472.81	He 1 4471.49A
4608.36	[O II] 4608.36	O 2 4607.00A
4622.94	[C 4622.94	C 1 4621.57A
4650.37	[C III] 4650.37	C 3 4649.00A
4659.39	[Fe III] 4659.39	Fe 3 4658.01A

**Table A.1** *continued*



**Table A.1** (*continued*)

Vacuum Wavelength (Å)	Line ID	Cloudy ID
(1)	(2)	(3)
4670.63	[P II] 4670.63	P 2 4669.25A
4687.02 <sup>*</sup>	He II 4687.02	He 2 4685.64A
4703.01	[Fe III] 4703.01	Fe 3 4701.62A
4712.65 <sup>†</sup>	[Ar IV] 4712.65	Ar 4 4711.26A
4714.42	He I 4714.42	He 1 4713.03A
4741.52 <sup>†</sup>	[Ar IV] 4741.52	Ar 4 4740.12A
4721.39	[Ne IV] 4721.39	Blnd 4720.00A
4756.04	[Fe III] 4756.04	Fe 3 4754.64A
4862.76	H I (Ba- $\beta$ ) 4862.76	H 1 4861.33A
4914.45	[O II] 4914.45	O 2 4913.00A
4923.38	He I 4923.38	He 1 4921.93A
4932.68 <sup>†</sup>	[O III] 4932.68	O 3 4931.23A
4960.37 <sup>†</sup>	[O III] 4960.37	O 3 4958.91A
5006.47	[N II] 5006.47	N 2 5005.00A
5008.31 <sup>†</sup>	[O III] 5008.31	O 3 5006.84A
5017.16	He I 5017.16	He 1 5015.68A
5049.13	He I 5049.13	He 1 5047.64A
5193.35	[Ar III] 5193.35	Ar 3 5191.82A
5199.43	[N I] 5199.43	N 1 5197.90A
5201.79	[N I] 5201.79	N 1 5200.26A
5271.95	[Fe III] 5271.95	Fe 3 5270.40A
5324.84	[Cl IV] 5324.84	Cl 4 5323.28A
5519.33	[Cl III] 5519.33	Cl 3 5517.71A
5539.49	[Cl III] 5539.49	Cl 3 5537.87A
5578.97	[O I] 5578.97	O 1 5577.34A
5680.66	[N II] 5680.66	N 2 5679.00A
5756.29	[N II] 5756.29	N 2 5754.61A
5877.36	He I 5877.36	He 1 5875.64A
5891.67	Na I 5891.67	Na 1 5889.95A
6302.14	[O I] 6302.14	O 1 6300.30A
6313.90	[S III] 6313.9	S 3 6312.06A
6365.64	[O I] 6365.64	O 1 6363.78A
6549.96	[N II] 6549.96	N 2 6548.05A
6564.72	H I (Ba- $\alpha$ ) 6564.72	H 1 6562.81A
6585.37	[N II] 6585.37	N 2 6583.45A
6680.10	He I 6680.1	He 1 6678.15A
6718.40	[S II] 6718.4	S 2 6716.44A
6721.96	[S II] 6721.96	Blnd 6720.00A
6732.78	[S II] 6732.78	S 2 6730.82A
7067.28	He I 7067.28	He 1 7065.22A

**Table A.1** *continued*

**Table A.1** (*continued*)

Vacuum Wavelength (Å)	Line ID	Cloudy ID
(1)	(2)	(3)
7137.87	[Ar III] 7137.87	Ar 3 7135.79A
7172.79 <sup>‡</sup>	[Ar IV] 7172.79	Ar 4 7170.70A
7239.87 <sup>‡</sup>	[Ar IV] 7239.87	Ar 4 7237.77A
7265.44 <sup>‡</sup>	[Ar IV] 7265.44	Ar 4 7263.33A
7283.47	He I 7283.47	He 1 7281.35A
7308.12	[Ca II] 7308.12	Blnd 7306.00A
7325.13	[O II] 7325.13	Blnd 7323.00A
7334.13	[O II] 7334.13	Blnd 7332.00A
7334.28 <sup>‡</sup>	[Ar IV] 7334.28	Ar 4 7332.15A
7532.73	[Cl IV] 7532.73	Cl 4 7530.54A
7753.36	[Ar III] 7753.36	Ar 3 7751.11A
7775.26	O I 7775.26	O 1 7773.00A
7951.81	O I 7951.81	O 1 7949.50A
8047.95	[Cl IV] 8047.95	Cl 4 8045.62A
8364.15	He I 8364.15	He 1 8361.73A
8581.19	[Cl II] 8581.19	Cl 2 8578.70A
8619.45	[Fe II] 8619.45	Fe 2 8616.95A
8729.66	[C I] 8729.66	C 1 8727.13A
9017.48	H I (Pa-7) 9017.	H 1 9014.87A
9071.25	[S III] 9071.25	S 3 9068.62A
9126.24	[Cl II] 9126.24	Cl 2 9123.60A
9231.64	H I (Pa-6) 9231.64	H 1 9228.97A
9266.68	O I 9266.68	O 1 9264.00A
9466.31	He I 9466.31	He 1 9463.57A
9533.38	[S III] 9533.38	S 3 9530.62A
9548.69	H I (Pa-5) 9548.69	H 1 9545.93A
9606.22	He I 9606.22	He 1 9603.44A
9852.85	[C I] 9852.85	Blnd 9850.00A
9905.86	[C II] 9905.86	C 2 9903.00A
10052.2	H I (Pa-δ) 1.0052μm	H 1 1.00493m
10111.8 <sup>‡</sup>	Fe VI 1.0112μm	Fe 6 1.01089m
10126.2 <sup>‡</sup>	He II 1.0126μm	He 2 1.01233m
10289.7	[S II] 1.029μm	S 2 1.02867m
10314.3	He I 1.0314μm	He 1 1.03113m
10339.4	[S II] 1.0339μm	S 2 1.03364m
10323.5	[S II] 1.0324μm	S 2 1.03205m
10339.4	[S II] 1.0339μm	S 2 1.03364m
10373.5	[S II] 1.0373μm	S 2 1.03705m
10670.9	He I 1.0671μm	He 1 1.06678m
10749.3	[Fe XIII] 1.0749μ	Fe13 1.07462m

**Table A.1** *continued*

**Table A.1** (*continued*)

Vacuum Wavelength ( $\text{\AA}$ )	Line ID	Cloudy ID
(1)	(2)	(3)
10833.4	He I 1.0833 $\mu\text{m}$	He 1 1.08303m
10916.2	He I 1.0916 $\mu\text{m}$	He 1 1.09130m
10920.3	He I 1.0920 $\mu\text{m}$	He 1 1.09171m
10941.2	H I (Pa- $\gamma$ ) 1.0941 $\mu\text{m}$	H 1 1.09380m
10999.8	He I 1.1 $\mu\text{m}$	He 1 1.09966m
11016.3	He I 1.1016 $\mu\text{m}$	He 1 1.10131m
11048.2	He I 1.1048 $\mu\text{m}$	He 1 1.10450m
11471.5	P II 1.1471 $\mu\text{m}$	P 2 1.14682m
11886.2	P II 1.1886 $\mu\text{m}$	P 2 1.18828m
11972.7	He I 1.1973 $\mu\text{m}$	He 1 1.19692m
12531.0	He I 1.2531 $\mu\text{m}$	He 1 1.25274m
12570.4	Fe II 1.2570 $\mu\text{m}$	Fe 2 1.25668m
12788.6	He I 1.2789 $\mu\text{m}$	He 1 1.27849m
12794.2	He I 1.2794 $\mu\text{m}$	He 1 1.27905m
12821.7	H I (Pa- $\beta$ ) 1.2822 $\mu\text{m}$	H 1 1.28180m
12849.8	He I 1.285 $\mu\text{m}$	He 1 1.28461m
12972.1	He I 1.2972 $\mu\text{m}$	He 1 1.29684m
12988.6	He I 1.2989 $\mu\text{m}$	He 1 1.29849m
13209.3	Fe II 1.3209 $\mu\text{m}$	Fe 2 1.32055m
13415.6	He I 1.3416 $\mu\text{m}$	He 1 1.34117m
13722.2	Fe II 1.3722 $\mu\text{m}$	Fe 2 1.37182m
14304.9	[Si X] 1.4305 $\mu\text{m}$	Si10 1.43008m
15088.0	He I 1.5088 $\mu\text{m}$	He 1 1.50837m
16440.2	Fe II 1.6440 $\mu\text{m}$	Fe 2 1.64355m
17007.6	He I 1.7008 $\mu\text{m}$	He 1 1.70027m
17367.0	H I (Br-6) 1.7367 $\mu\text{m}$	H 1 1.73620m
18099.1	Fe II 1.8099 $\mu\text{m}$	Fe 2 1.80939m
18179.2	H I (Br-5) 1.8179 $\mu\text{m}$	H 1 1.81740m
18690.8	He I 1.8691 $\mu\text{m}$	He 1 1.86854m
18702.6	He I 1.8703 $\mu\text{m}$	He 1 1.86972m
18756.4	H I (Pa- $\alpha$ ) 1.8756 $\mu\text{m}$	H 1 1.87510m
19094.9	He I 1.9095 $\mu\text{m}$	He 1 1.90894m
19350.2	[Si XI] 1.9350 $\mu\text{m}$	Si11 1.93446m
19451.0	H I (Br- $\delta$ ) 1.9451 $\mu\text{m}$	H 1 1.94454m
19548.6	He I 1.9549 $\mu\text{m}$	He 1 1.95430m
19630.4 $^{\dagger}$	[Si VI] 1.9630 $\mu\text{m}$	Si 6 1.96247m
20450.3	[Al IX] 2.0450 $\mu\text{m}$	Al 9 2.04444m
20587.2	He I 2.0587 $\mu\text{m}$	He 1 2.05813m
21124.1	He I 2.1124 $\mu\text{m}$	He 1 2.11180m
21136.4	He I 2.1136 $\mu\text{m}$	He 1 2.11303m

**Table A.1** *continued*

**Table A.1** (*continued*)

Vacuum Wavelength (Å)	Line ID	Cloudy ID
(1)	(2)	(3)
21661.3	H I (Br- $\gamma$ ) 2.1661 $\mu$ m	H 1 2.16551m
23218.4	[Ca VIII] 2.3218 $\mu$ m	Ca 8 2.32117m
24734.5	He I 2.4735 $\mu$ m	He 1 2.47274m
24814.2	[Si VII] 2.4814 $\mu$ m	Si 7 2.48071m
26192.5	He I 2.6193 $\mu$ m	He 1 2.61850m
26206.0	He I 2.6206 $\mu$ m	He 1 2.61985m
26241.4	He I 2.6241 $\mu$ m	He 1 2.62338m
26258.9	H I (Br- $\beta$ ) 2.6259 $\mu$ m	H 1 2.62513m
29053.4 $^{\dagger}$	[Al V] 2.9053 $\mu$ m	Al 5 2.90450m
30392.2	H I (Pf-5) 3.0392 $\mu$ m	H 1 3.03835m
32070.2 $^{\dagger}$	[Ca IV] 3.2070 $\mu$ m	Ca 4 3.20610m
32970.2	H I (Pf- $\delta$ ) 3.2970 $\mu$ m	H 1 3.29607m
36603.7 $^{\dagger}$	[Al VI] 3.6604 $\mu$ m	Al 6 3.65932m
37036.7	He I 3.7037 $\mu$ m	He 1 3.70260m
37405.9	H I (Pf- $\gamma$ ) 3.7406 $\mu$ m	H 1 3.73951m
39293.3	[Si IX] 3.9293 $\mu$ m	Si 9 3.92820m
40378.0	He I 4.0378 $\mu$ m	He 1 4.03664m
40409.9	He I 4.041 $\mu$ m	He 1 4.03983m
40490.7	He I 4.0491 $\mu$ m	He 1 4.04791m
40490.9	He I 4.0491 $\mu$ m	He 1 4.04793m
40523.0	H I (Br- $\alpha$ ) 4.0523 $\mu$ m	H 1 4.05113m
42958.3	He I 4.2958 $\mu$ m	He 1 4.29459m
44884.1 $^{\dagger}$	[Mg IV] 4.4884 $\mu$ m	Mg 4 4.48712m
45293.0 $^{\dagger}$	[Ar VI] 4.5293 $\mu$ m	Ar 6 4.52800m
46181.6	K III 4.6182 $\mu$ m	K 3 4.61683m
46538.1	H I (Pf- $\beta$ ) 4.6538 $\mu$ m	H 1 4.65247m
51286.9	H I (Hu- $\delta$ ) 5.1287 $\mu$ m	H 1 5.12722m
53403.5	Fe II 5.3403 $\mu$ m	Fe 2 5.33881m
55033.5	[Mg VII] 5.5034 $\mu$ m	Mg 7 5.50177m
56086.1 $^{\dagger}$	[Mg V] 5.6086 $\mu$ m	Mg 5 5.60700m
59082.5	H I (Hu- $\gamma$ ) 5.9082 $\mu$ m	H 1 5.90655m
59820.2 $^{\dagger}$	K IV 5.9820 $\mu$ m	K 4 5.98030m
65147.5	[Si VII] 6.5148 $\mu$ m	Si 7 6.51288m
69853.8	Ar II 6.9854 $\mu$ m	Ar 2 6.98337m
73191.6 $^{\dagger}$	Na III 7.3192 $\mu$ m	Na 3 7.31706m
74538.8	He I 7.4539 $\mu$ m	He 1 7.45174m
74562.5	He I 7.4562 $\mu$ m	He 1 7.45411m
74562.6	He I 7.4563 $\mu$ m	He 1 7.45412m
74599.2	H I (Pf- $\alpha$ ) 7.4599 $\mu$ m	H 1 7.45777m
75025.4	H I (Hu- $\beta$ ) 7.5025 $\mu$ m	H 1 7.50038m

**Table A.1** *continued*

**Table A.1** (*continued*)

Vacuum Wavelength (Å)	Line ID	Cloudy ID
(1)	(2)	(3)
76453.8 <sup>†</sup>	[Ne VI] 7.6454 $\mu$ m	Ne 6 7.64318m
78126.2 <sup>†</sup>	[Fe VII] 7.8126 $\mu$ m	Fe 7 7.81037m
79019.8 <sup>†</sup>	[Ar V] 7.902 $\mu$ m	Ar 5 7.89971m
87601.2	H I 8.7601 $\mu$ m	H 1 8.75760m
89915.7	Ar III 8.9916 $\mu$ m	Ar 3 8.98898m
90091.4 <sup>  </sup>	[Mg VII] 9.0091 $\mu$ m	Mg 7 9.00655m
90335.8 <sup>†</sup>	[Na IV] 9.0336 $\mu$ m	Na 4 9.03098m
95103.6 <sup>†</sup>	[Fe VII] 9.5104 $\mu$ m	Fe 7 9.50763m
105106	[S IV] 10.5106 $\mu$ m	S 4 10.5076m
113088	H I 11.3088 $\mu$ m	H 1 11.3055m
117663	Cl IV 11.7663 $\mu$ m	Cl 4 11.7629m
123109 <sup>†</sup>	[Fe VI] 12.3109 $\mu$ m	Fe 6 12.3074m
123720	H I (Hu- $\alpha$ ) 12.372 $\mu$ m	H 1 12.3684m
128138	Ne II 12.8138 $\mu$ m	Ne 2 12.8101m
131023 <sup>†</sup>	[Ar V] 13.1023 $\mu$ m	Ar 5 13.0985m
143269 <sup>†</sup>	[Ne V] 14.3269 $\mu$ m	Ne 5 14.3228m
143680	Cl II 14.368 $\mu$ m	Cl 2 14.3639m
147712 <sup>†</sup>	[Fe VI] 14.7712 $\mu$ m	Fe 6 14.7670m
155554 <sup>†</sup>	Ne III 15.5554 $\mu$ m	Ne 3 15.5509m
162092	H I 16.2092 $\mu$ m	H 1 16.2045m
178848	P III 17.8848 $\mu$ m	P 3 17.8797m
179366	Fe II 17.9366 $\mu$ m	Fe 2 17.9314m
187132	S III 18.7132 $\mu$ m	S 3 18.7078m
190620	H I 19.062 $\mu$ m	H 1 19.0565m
195583 <sup>†</sup>	[Fe VI] 19.5583 $\mu$ m	Fe 6 19.5527m
203255	Cl IV 20.3255 $\mu$ m	Cl 4 20.3197m
218363	Ar III 21.8363 $\mu$ m	Ar 3 21.8300m
229256	[Fe III] 22.9256 $\mu$ m	Fe 3 22.9190m
242135 <sup>†</sup>	[Ne V] 24.2135 $\mu$ m	Ne 5 24.2065m
245191	Fe II 24.5191 $\mu$ m	Fe 2 24.5120m
258906 <sup>*</sup>	O IV 25.8906 $\mu$ m	O 4 25.8832m
259886	Fe II 25.9886 $\mu$ m	Fe 2 25.9811m
278035	H I 27.8035 $\mu$ m	H 1 27.7955m
328715	P II 32.8715 $\mu$ m	P 2 32.8620m
330365	[Fe III] 33.0365 $\mu$ m	Fe 3 33.0270m
332817	Cl II 33.2817 $\mu$ m	Cl 2 33.2721m
334800	S III 33.48 $\mu$ m	S 3 33.4704m
348146	Si II 34.8146 $\mu$ m	Si 2 34.8046m
353496	Fe II 35.3496 $\mu$ m	Fe 2 35.3394m
360140 <sup>†</sup>	Ne III 36.014 $\mu$ m	Ne 3 36.0036m

**Table A.1** *continued*



**Table A.1** (*continued*)

Vacuum Wavelength ( $\text{\AA}$ )	Line ID	Cloudy ID
(1)	(2)	(3)
388701	H I 38.8701 $\mu\text{m}$	H 1 38.8589m
513013	Fe II 51.3013 $\mu\text{m}$	Fe 2 51.2865m
516804	[Fe III] 51.6804 $\mu\text{m}$	Fe 3 51.6655m
518153 <sup>†</sup>	O III 51.8153 $\mu\text{m}$	O 3 51.8004m
573403	N III 57.3403 $\mu\text{m}$	N 3 57.3238m
606437	P II 60.6437 $\mu\text{m}$	P 2 60.6263m
631861	O I 63.1861 $\mu\text{m}$	O 1 63.1679m
883577 <sup>†</sup>	O III 88.3577 $\mu\text{m}$	O 3 88.3323m
121802	N II 121.802 $\mu\text{m}$	N 2 121.767m
145537	O I 145.537 $\mu\text{m}$	O 1 145.495m
157681	C II 157.681 $\mu\text{m}$	C 2 157.636m
205303	N II 205.303 $\mu\text{m}$	N 2 205.244m
370375	[C I] 370.375 $\mu\text{m}$	C 1 370.269m
609765	[C I] 609.765 $\mu\text{m}$	C 1 609.590m

\*Line that is strong relative to  $\text{H}\beta$  or  $\text{Pa}\beta$ , and strongly enhanced by the addition of the  $\text{SXP}_{\text{ULX}}$ , relative to SSP-only models.

<sup>†</sup>Line that is strong relative to  $\text{H}\beta$  or  $\text{Pa}\beta$ , but not strongly enhanced relative to SSP-only models.

<sup>‡</sup>Line that is weak relative to  $\text{H}\beta$  or  $\text{Pa}\beta$ , but strongly enhanced relative to SSP-only models.

<sup>||</sup>Line with zero flux.

NOTE—Criteria for strength relative to  $\text{H}\beta$  or  $\text{Pa}\beta$ , or enhancement relative to the SSP-only models are described in Section 5.1. Only lines with ionization potentials  $\geq 54$  eV are marked in the table according to the above criteria.

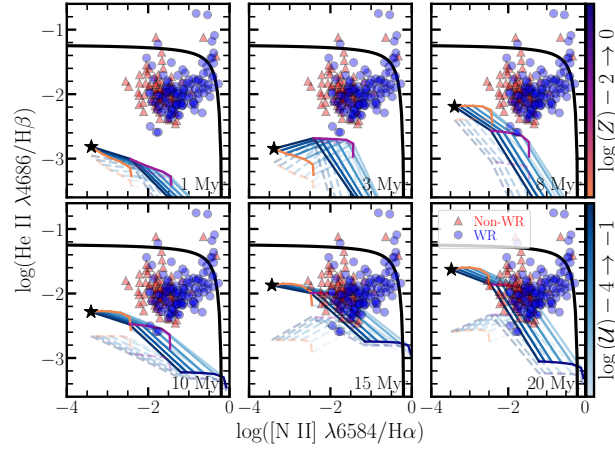


**Figure A.1.** Same as Figure 8, but with the strict delay-time dependence for the SXP<sub>ULX</sub> removed. Here we show  $t_{\text{burst}} = 1\text{--}3$  Myr in the top left and center panels to illustrate the effect of allowing the SXP<sub>ULX</sub> to form immediately with the corresponding SSP.

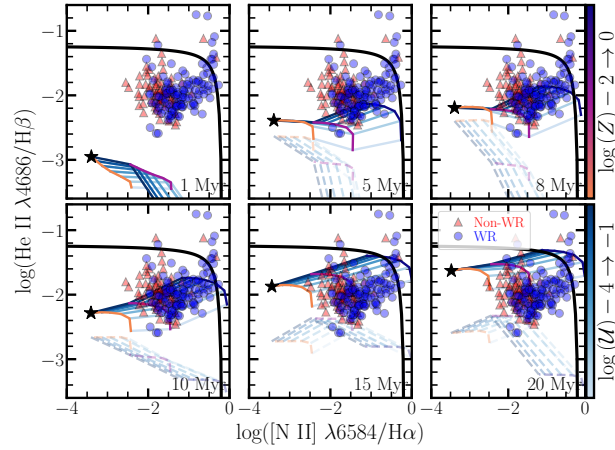


**Figure A.2.** Same as Figure 8, but with the strict correspondence of the metallicity dependence of the SXP<sub>ULX</sub> relative to the SSP removed. In this case, the grid with SXP<sub>ULX</sub> contribution overlaps with nearly the entire range of observed line ratios, even at very extreme He II  $\lambda 4686/\text{H}\beta$ , but requires extremely high, and therefore likely unphysical X-ray production efficiencies (i.e.,  $L_X/\text{SFR}$ ) for ULXs at high metallicity in order to do so.